Title
Interfacial heat and mass transfer of liquid films flowing down strings against counterflowing gas streams

Author
Zeng, Zezhi

Publication Date
2019

Peer reviewed|Thesis/dissertation

UNIVERSITY OF CALIFORNIA

Los Angeles

Interfacial heat and mass transfer of liquid films flowing down strings against counterflowing gas streams

A dissertation submitted in partial satisfaction

of the requirements for the degree

Doctor of Philosophy in Mechanical Engineering

by

Zezhi Zeng

2019

ABSTRACT OF THE DISSERTATION

Interfacial heat and mass transfer of liquid films flowing

down strings against counterflowing gas streams

by

Zezhi Zeng

Doctor of Philosophy in Mechanical Engineering

University of California, Los Angeles, 2019

Professor Yongho Ju, Chair

Direct-contact exchangers that involve energy exchange between gas and liquid streams have a variety of applications, including waste heat recovery, thermoelectric power plant cooling, and thermal desalination. Direct-contact methods are appealing as they may help mitigate potential corrosion, fouling, and scaling of solid surfaces and enhance transfer effectiveness. The widely used direct contact exchangers these days, such as packed bed and spray columns, suffer from the problems of low gas loading limit or inefficient transfer rate. Alternative exchanger technologies that can circumvent these limitations are urgently needed to enable wider adoption of direct contact methods. This dissertation presents the study on an innovative alternative to the direct contact heat and mass exchanger. The new economic light-weight direct-contact exchanger incorporates an array of strings of diameter of the order of 0.1~1 mm to sustain flows of thin liquid films. Thin

liquid films flow down the strings by gravity and exchange thermal energy with a counterflowing gas stream. To enable physics-based systematic design of the multi-string based direct contact exchanger, we need rigorous understanding of the fluid dynamics and interfacial heat and mass transfer of liquid films flowing down strings (i.e. a polymer or cotton string) against counterflowing air streams.

We began our study from numerically investigating the fluid dynamics and heat transfer of a liquid film flowing down a single string. We constructed finite element models using a moving mesh method to solve the time-dependent Navier-Stokes equation and the energy equation to obtain velocity and temperature distributions in the liquid film. The temporal variations in the temperature of travelling beads are analyzed to evaluate the effective heat transfer coefficients and to assess the accuracy of an approximate one-dimensional model.

We then conducted a combined experimental and modeling study of the flow and heat transfer characteristics of thin liquid films flowing down a single string in the presence of a counterflowing cooling gas. We focus on the Rayleigh-Plateau (RP) regime, where uniformly spaced drop-like liquid beads travel on a thin liquid substrate formed along the entire length of a vertical string. Using a high-speed camera and micro-thermocouples, we capture liquid film/bead profiles and temperatures at different air velocities and at different nozzle diameters. Finite element models are also constructed to help interpret and validate experimentally obtained heat transfer characteristics.

Moreover, we extended our experimental study from a single string to a direct-contact multi-string heat exchanger. We constructed a 1.6 m-tall prototype heat exchanger with an array of as many as 112 vertically aligned strings. We limited ourselves to non-evaporating liquids and non-condensing gases (air). We measure axial liquid temperature profiles and gas-stream pressure drop

to examine the impact on the thermohydraulic performance of the liquid and air flow rates, instability modes, and string pitch. The applicability of the Reynolds analogy is also examined.

Finally, we adapted our multi-string heat exchanger to a humidifier for thermal desalination. We investigate the evaporation rate as well as gas phase pressure drop. The evaporation process involves simultaneous heat and mass transfer. We report a combined experimental characterization and modeling study to validate our humidifier design for desalination purpose. The effects of the liquid flow rate, air velocity, and liquid salinity on the evaporation rates are experimentally characterized. The gas-stream pressure drop of the multi-string humidifier is measured and compared with existing humidifier designs.

The dissertation of Zezhi Zeng is approved.

Adrienne G. Lavine

Jeffrey D. Eldredge

Michael K. Stenstrom

Yongho Ju, Committee Chair

University of California, Los Angeles

2019

This dissertation is dedicated to my beloved family

TABLE OF CONTENTS

LIST OF FIGURES

ACKNOWLEDGEMENTS

I would like to first express my sincere appreciation and gratitude to my advisor, Professor Yongho Sungtaek Ju, for his enthusiastic guidance and encouragement throughout my PhD research, as well as his insightful suggestions and supports for my future career development. I would like to then thank my committee members, Professor Adrienne Lavine, Professor Jeff Eldredge, and Professor Michael Stenstrom, for their valuable suggestions and encouragement. Professor Andrea Bertozzi and Professor Gopinath Warrier are also gratefully acknowledged for their suggestions and support. I would also like to thank Professor Webb Marner for his suggestions and encouragement for my future development.

I would like to thank my former and current colleagues in UCLA Multiscale Thermosciences Laboratory: Jinda Zhuang, Cheng Peng, Aref Vandadi, Abolfazl Sadeghpour, Yide Wang, Chao Fan, Navid dehdari Ebrahimi, Zhengxian Qu, Dong Hyun Ko, and Erfan Sedighi for their help and support during my stay at UCLA. I would also like to thank staff members from UCLA mechanical engineering department: Mr. Benjamin Tan and Mr. Miguel Lozano for their assistance and support in device fabrication, experimental design and teaching assistant training.

Finally, I would like to give my deepest gratitude to my wife Bing-Ang Mei and my family for their endless love and support.

VITA

2010-2014	B.Eng., Mechanical Engineering The Hong Kong University of Science and Technology
2014-2019	Graduate Student Researcher/Teaching Assistant Mechanical and Aerospace Engineering Department University of California, Los Angeles

PUBLICATIONS

Journal Publications

Zeng, Z., Sadeghpour, A., Warrier, G. and Ju, Y.S., 2017. Experimental study of heat transfer between thin liquid films flowing down a vertical string in the Rayleigh-Plateau instability regime and a counterflowing gas stream. *International Journal of Heat and Mass Transfer*, 108, pp.830-840.

Zeng, Z., Sadeghpour, A. and Ju, Y.S., 2018. Thermohydraulic characteristics of a multi-string direct-contact heat exchanger. *International Journal of Heat and Mass Transfer*, 126, pp.536-544.

Zeng, Z., Sadeghpour, A., & Ju, Y. S., 2019. A highly effective multi-string humidifier with a low gas stream pressure drop for desalination. *Desalination*, 449, 92-100.

Sadeghpour, A., **Zeng, Z**. and Ju, Y.S., 2017. Effects of Nozzle Geometry on the Fluid Dynamics of Thin Liquid Films Flowing down Vertical Strings in the Rayleigh–Plateau Regime. *Langmuir*, 33(25), pp.6292-6299.

Conference Publication

Zeng, Z., Sadeghpour, A. and Ju, Y.S., 2018. Experimental study of heat transfer and pressure drop in a multistring based direct contact heat exchanger" *Proc. 16th Int. Heat Transfer Conf.*

Zeng, Z., Warrier, G. and Ju, Y.S., 2015. Flow and Heat Transfer in Liquid Films Flowing Over Highly Curved Surface. *ASME 2015 International Technical Conference and Exhibition on Packaging and Integration of Electronic and Photonic Microsystems collocated with the ASME 2015 13th International Conference on Nanochannels, Microchannels, and Minichannels*.

Zeng, Z., Warrier, G. and Ju, Y.S., 2015. Study of the Fluid Dynamics of Thin Liquid Films Flowing Down a Vertical String With Counterflow of Gas. *ASME 2015 International Mechanical Engineering Congress and Exposition*

CHAPTER 1

Introduction

1.1 Motivation

Direct-contact heat exchangers are good candidates in many applications, such as indirect dry cooling of thermoelectric power plants; waste heat capture; and heating or cooling of gaseous feed stocks or products in chemical processing. The indirect contact exchanger, such as the conventional shell and tube heat exchanger suffer from the problem of fouling and corrosion. The direct contact method involves no solid surface and is therefore capable of avoiding those problem. The heat and mass transfer processes are also enhanced due to direct contact between two streams of liquid. Packed beds are widely used in various direct-contact heat transfer applications [1–3] because their tortuous flow paths help achieve high heat transfer effectiveness. However, relatively high pressure drops experienced by the gas streams and low limits on gas loadings due to liquid flooding remain major challenges [4, 5]. Spray columns achieve heat transfer by dispensing small droplets into gas streams [6] but they can experience practical challenges: excess liquid pumping power required for spray generation; potential environmental issues associated with small droplets carried away with gas streams; and degraded heat transfer performance due to short residence time of large droplets [7]. New concepts and designs for direct-contact heat exchangers that can deliver high heat exchanger effectiveness while circumventing these challenges are desirable.

We propose a promising alternative: DIrect-contact Liquid-on-String Heat Exchanger (DILSHE), schematically illustrated in Figure 1.1. Each DILSHE unit consists of a dense array of aligned polymer strings with a diameter of the order of 1 mm. A heated coolant (after exiting a

surface condenser, for example) is fed into the top reservoir of the DILSHE unit. As thin films of the liquid coolant flow along the strings, they form traveling liquid beads due to flow instabilities. The coolant films/beads are cooled by counterflowing air. The straight flow paths for the air lead to lower air pressure drop and higher gas load limits when compared with packed beds. By inhibiting radial liquid transport, DILSHE also reduces liquid mal-distributions. Inexpensive polymer strings enable construction of economic and low-weight cooling modules that can be readily scaled.

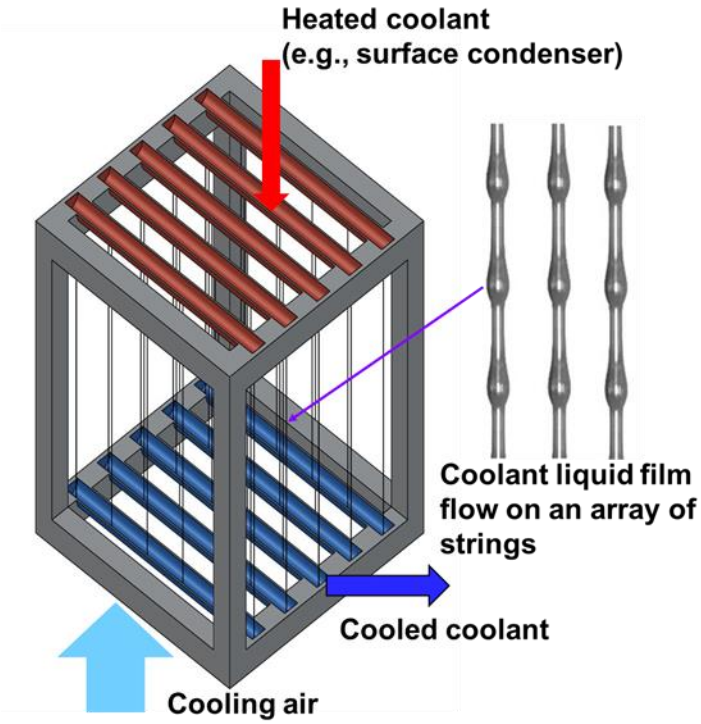

Figure 1.1: Schematic of a DILSHE module. Such modules may be stacked in arrays

1.2 Application of the multi-string exchanger

This multi-string exchanger has advantages of the high interfacial heat/mass transfer rate, low gas phase pressure drop, and light foot weight/cost. Implementing multi-string exchangers in the thermoelectric powerplant dry cooling or thermal desalination can greatly reduce the facilities size

and expense. These advantages make the multi-string exchanger superior to other direct contact methods and competitive among existing commercial exchangers.

1.2.1 Powerplant dry cooling

In recent years, there has been much interest in the research and development of dry cooling systems for power plants. Dwindling fresh water resources available for power plant cooling has resulted in the need to develop power plant cooling systems that minimize or completely eliminate water losses to the environment [8]. The use of air cooled condensers (ACC) for power plant cooling is gaining in popularity. However, since dry cooling systems have relatively poor heat transfer performance and higher cost compared with traditional wet cooling systems, innovative dry cooling solutions need to be developed to compete with existing wet cooling systems. The minimum steam condensation temperature in ACCs is dictated by the ambient dry bulb temperature and the air temperature rise across the ACC. In wet cooling systems, the wet bulb temperature can be much lower than the dry bulb temperature resulting in better turbine output and efficiency. The conventional air cooled condenser also consists of metal fins which require large amount of heavy civil work. The considerable expense of the metal components also retards the wider adoption of the air cooled condenser. An economic alternative to the air cooled condenser for thermoelectric powerplant dry cooling system is therefore desired to compete with the wet cooling method.

Figure 1.2 schematically illustrates the potential strategy to integrate our direct-contact multi-string heat exchangers into thermoelectric power plants. Each heat exchanger unit consists of a dense array of vertically aligned polymer strings of radii of the order of 0.1 mm. A heated non-volatile coolant (after exiting the surface condenser) is fed into each unit through top liquid

distributors. As it travels along the strings, the coolant is cooled by the counterflowing air stream. The straight and contiguous flow paths in-between the strings are expected to reduce pressure drops experienced by the gas streams than packed beds. At the same time, large gas/liquid interface-to-volume ratios and long residence times enable effective interfacial heat transfer process. The string arrays also limit radial liquid transport, facilitating more uniform liquid distributions. The use of polymer strings also reduces the cost and weight of the heat exchanger.

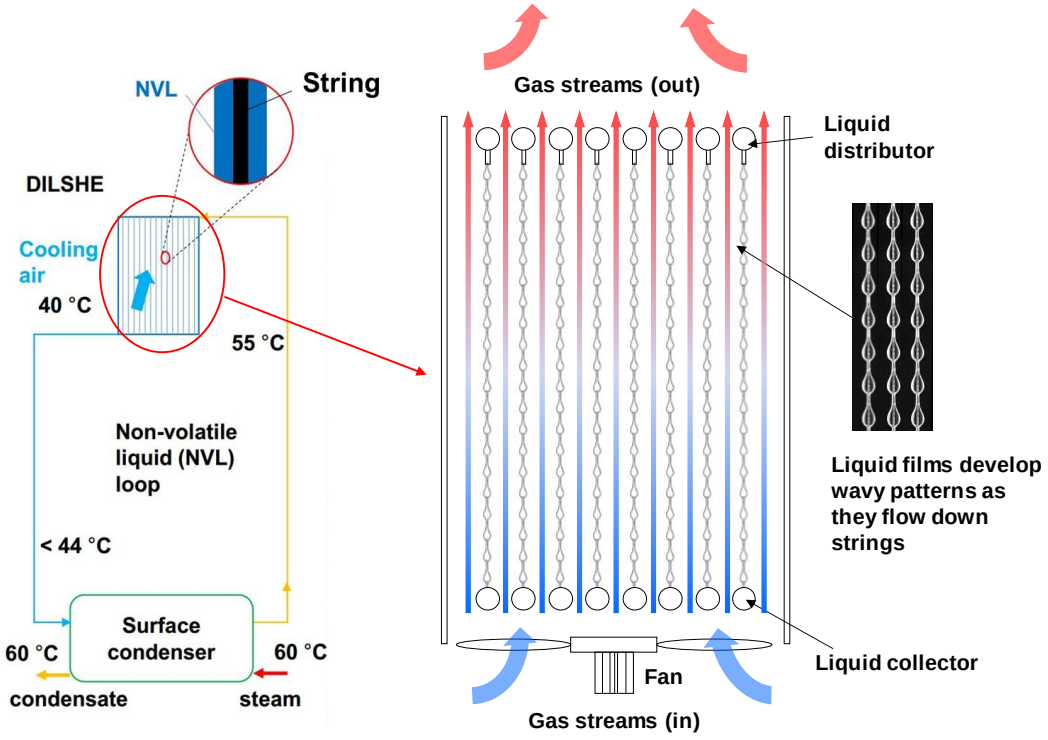

Figure 1.2: Schematic of a multi-string heat exchanger unit used to remove heat rejection from surface condensers in steam power plants

1.2.2 Thermal desalination

Water is a precious and limited resource. Agriculture, drinking, sanitation and thermoelectric power plant cooling all require significant amounts of fresh water. However, 97% of water on

earth is saline water and not suitable for many of these applications. This has motivated intense research efforts in developing various technologies for desalination and treatments/reuse of industrial and municipal waste water. The reverse osmosis (RO) [9, 10] has been widely used for desalination of sea water and treatment of certain waste water. Significant consumption of electricity, membrane fouling, and low limits on the acceptable salinity of feed water, however, have impeded their wider adoption [11]. Thermal desalination techniques, such as the multi-effect desalination (MED) and multi-stage flash desalination (MSF), can produce high quality distilled water [12]. However, relatively high total energy consumption and high capital/operating costs have presented barriers to their recent commercial deployments [13]. Humidification and dehumidification (HDH) is an intriguing thermal distillation technique for small-scale and mobile desalination and water treatment applications [14, 15] because it can operate under ambient pressure using low-grade and renewable heat sources and handle a wide variety of feed water streams. A HDH unit mimics natural water cycle by first humidifying a carrier gas and then condensing water vapor to produce distilled water.

Conventional shell and tube exchangers [16, 17] are widely used in a HDH system, but they are typically heavy and expensive and suffer from problems of corrosion and scaling. Direct-contact heat/mass exchangers help avoid the latter problems by suppressing phase change on solid surfaces and offer high specific interface areas for heat/mass transfer [18]. Recent studies reported the use of bubble columns as humidifiers or dehumidifiers [19–21]. A stream of air injected to a pool of water through small holes can create large liquid-gas interfacial areas for effective heat and mass transfer. A past study [22] experimentally investigated the effects of water temperature, hole diameter, and air flow rate on the performance of a bubble column humidifier. However,

bubble columns introduce significant gas-stream pressure drops and thereby require high electric energy consumption.

We propose a new design for humidifiers in the form of a multi-string heat/mass exchanger. The multi-string humidifier consists of a dense array of vertical aligned strings as illustrated in Figure 1.3. A heated liquid feed stream (i.e. seawater or industrial waste water) is flown down the strings while making direct contact with a counterflowing gas stream that carries the evaporated water. The unique configuration of our multi-string humidifier design affords high interface-to-volume ratios necessary for high heat/mass exchanger effectiveness in a compact and light-weight unit and at very low gas-stream pressure drops. To enable physics-based systematic design of the multi-string humidifier, we need rigorous understanding of the fluid dynamics and heat transfer characteristics of liquid films flowing down strings against counterflowing gas streams.

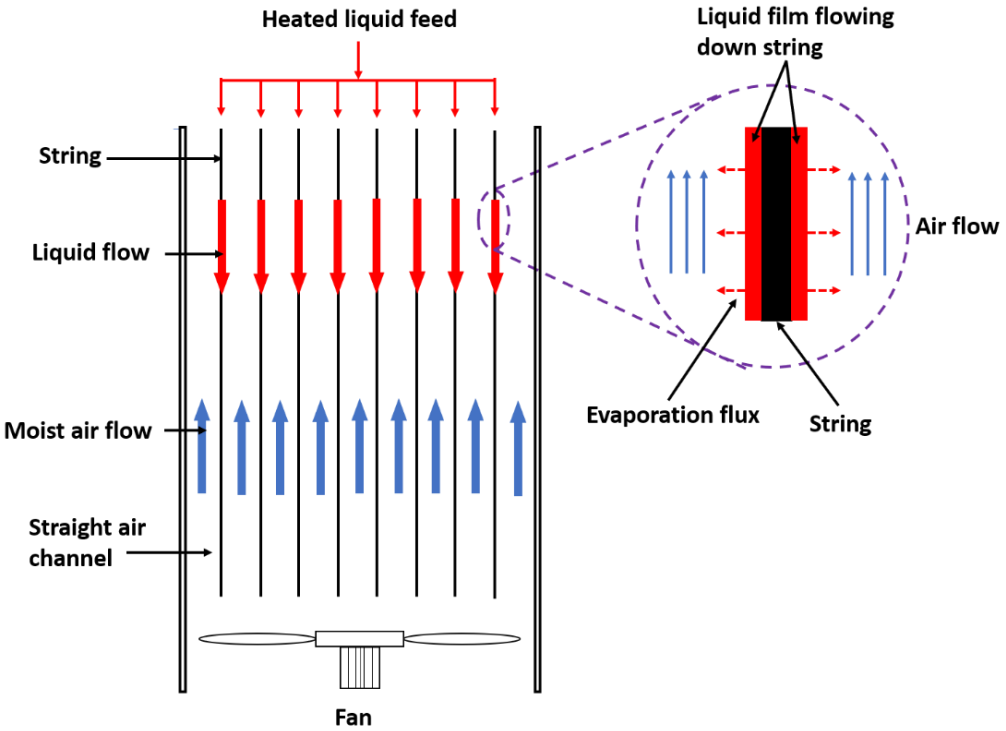

Figure 1.3: Schematic illustrating the operation of a multi-string humidifier.

1.3 Study of liquid films flowing down highly curved surfaces

1.3.1 Fluid dynamics of liquid films flowing down strings

Liquid films flowing over a highly curved surface [23] are unstable and form wavy profiles or traveling beads due to interplays among the surface tension, viscous and gravitational force. Two main types of instability experienced by such liquid films are the Rayleigh-Plateau (RP) instability [24], and the Kapitza instability [25] as shown in Figure 1.4. Kliakhandler et al. [26] experimentally studied highly viscous liquids flowing along vertical strings and proposed a creeping-flow model to predict flow patterns in the inertia-less limit. Ruyer-Quil et al. [27] added the effects of inertia and viscous diffusion to the evolution equation for the local film thickness and the local flow rate and predicted spatiotemporal variations of the liquid film profiles. A later study [28] improved the model using a weighted-residuals approach and considered the effects of inertia, azimuthal curvature, and viscous dispersion. This then led to the classification of four different flow regimes. Duprat et al. [29] examined the response of liquid films flowing down a vertical string to inlet forcing and studied the transition from the absolute to the convective instability both experimentally and theoretically [30]. A later numerical modeling study based on a multi-fluid method [31] showed results consistent with the previous experimental data in select flow conditions [32]. A recent study modeled the liquid film instability subject to an axial temperature gradient and investigated effect of thermocapillary force on the instability propagation [33]

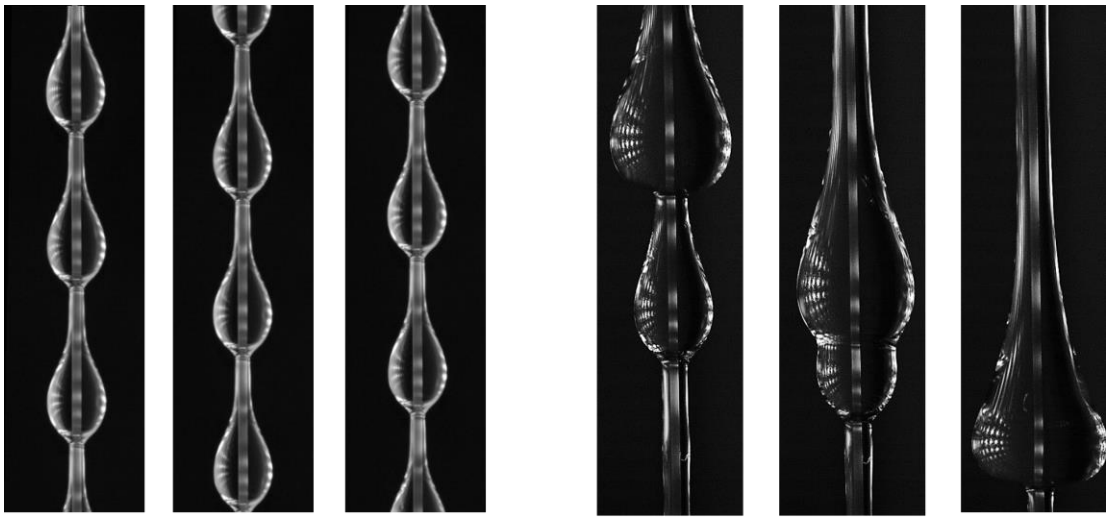

Figure 1.4: Two representative profiles of liquid film with (a) Rayleigh-Plateau instability (b) Kapitza instability

1.3.2 Interfacial heat/mass transfer between liquid films and gas streams

Past studies also explored the use of liquid films flowing down strings for direct contact heat and mass transfer applications. Hattori et al. [34] presented approximate analytical models for the temperature distribution of a liquid film subjected to cross-flows of a cooling gas. A later study performed CO_2 absorption experiments where they compared the performance of spray columns, packed beds and wetted string columns and demonstrated the superiority of wetted string columns [35]. Extending this work, Uchiyama et al. [5] reported an analytical model to predict the CO_2 absorption performance. Migita et al. [36] constructed a prototype containing an array of 109 strings to study CO_2 absorption effectiveness. They successfully demonstrated that, under the same inlet liquid and gas conditions, wetted string columns perform better in terms of absorption effectiveness and gas pressure drop over conventional packed columns and spray columns.

Pakdehi et al. [37] investigated the hydrazine absorption by a wetted string column with different number of strings and confirmed the advantage of wetted string columns in gas-phase pressure drop. Hosseini et al. [38] developed a CFD model and performed a parametric study to examine CO_2 absorption by a liquid film flowing along a single string. A recent study [39] also developed a numerical model for a CO_2 absorption process in a wetted string column and reported good agreement with the previous experimental results [36]. In addition to mass transfer studies, many experimental studies focus on investigating heat transfer performance of a turbulent liquid film around a uniformly heated tube [40–48]. Shmerler et al. [41, 42] measured the wall heat flux and temperature gradients across the liquid films to develop correlations for the normalized liquid-side heat transfer coefficients and the Reynolds number. These experiments focused on subcooled liquid films or saturated liquid films undergoing evaporation. However, very few studies were reported on heat transfer characteristics of liquid films flowing down thin strings with a counterflowing gas. A previous study [7] reported a rather limited experimental investigation of the cooling of thin films of a heated silicone oil flowing down single strings. By using strings with different diameters, they successfully achieved the string-of-bead flow and annular film flow at the same liquid flow rate, and demonstrated that the string-of-bead flow exhibited a higher overall heat transfer coefficient than the annular film flow.

However, the impact of the air velocity, liquid flow rate and nozzle radius on liquid film flow characteristics, and the relationship between the flow characteristics and heat transfer effectiveness still need further investigations. The gas-phase pressure drop of different air flow conditions also needs systematic studies to optimize the design of multi-string exchangers. It is also necessary to rigorously understand the simultaneous heat and mass transfer (i.e. water evaporation) of the liquid

film flowing down strings against counterflowing gas streams to evaluate the feasibility of adapting multi-string exchanger to the humidifier and dehumidifier for thermal desalination.

1.4 Objectives of the present study

The presents study aims to (i) conduct a combination of numerical and experimental study that helps improve our understanding of the fluid dynamics and heat transfer of a thin liquid film flowing down a single string against a counterflowing air stream, which helps build a foundation for the systematic design and optimization of a multi-string exchanger, (ii) experimentally investigate the heat transfer performance as well as the gas-phase pressure drop in a string-based direct-contact heat exchanger, (iii) construct a reliable numerical simulation to anticipate the heat transfer effectiveness and the gas phase pressure drop of the multi-string exchanger. (iv) experimentally study the simultaneous heat and mass transfer of water films flowing down cotton strings with the presence of a counterflowing gas stream and demonstrate the feasibility of adapting the multi-string exchanger for humidification-dehumidification technology and related applications. (v) compare the exchanger effectiveness and gas-phase pressure drop between a multi-string exchanger and other existing commercial direct-contact methods under the same working conditions.

1.5 Organization of the document

The present study investigates the interfacial heat and mass transfer of liquid films flowing down strings against counterflowing gas streams.

Chapter 2 presents the study of the fluid dynamics and heat transfer of a liquid film flowing down a single string. We constructed finite element models using a moving mesh method to solve

the time-dependent Navier-Stokes equation and the energy equation to obtain velocity and temperature distributions in the liquid and the counter-flowing cooling air. The temporal variations in the temperature of travelling beads are analyzed to evaluate the effective heat transfer coefficients and to assess the accuracy of an approximate one-dimensional model.

Chapter 3 discusses a combined experimental and modeling study of the flow and heat transfer characteristics of thin liquid films flowing down a single string in the presence of a counterflowing cooling gas. We focus on the Rayleigh-Plateau (RP) regime, where uniformly spaced drop-like liquid beads travel on a thin liquid substrate formed along the entire length of a vertical string. Using a high-speed camera and micro-thermocouples, we capture liquid film/bead profiles and temperatures at different air velocities and at different nozzle diameters. Finite element models are constructed to help interpret and validate experimentally obtained heat transfer characteristics.

Chapter 4 extends our experimental study to a direct-contact multi-string heat exchanger. We constructed a 1.6 m-tall prototype heat exchanger with an array of as many as 112 vertically aligned strings. We limited ourselves to non-evaporating liquids and non-condensing gases (air). We measure axial liquid temperature profiles and gas-stream pressure drop to examine the impact on the thermohydraulic performance of the liquid and air flow rates, instability modes, and string pitch. The applicability of the Reynolds analogy is also examined.

Chapter 5 explores the application of using the multi-string humidifier for thermal desalination purpose. We investigated simultaneous heat and mass transfer of liquid films flowing down strings against counterflowing gas streams. We report a combined experimental characterization and modeling study to validate our humidifier design, specifically with desalination applications in mind. The effects of the liquid flow rate, air velocity, and liquid salinity on the heat and mass transfer rates are experimentally characterized. The mass transfer conductance-interfacial area

products obtained are next used to quantify the performance of a multi-string humidifier. The gas-stream pressure drop of the multi-string humidifier is also measured and compared with existing humidifier designs.

CHAPTER 2

A moving mesh method to study flow and heat transfer in liquid films flowing over highly curved surfaces

This chapter aims to introduce a numerical method to predict the spatial temperature profile of the liquid film flowing along a single string against a counterflowing gas stream. We investigate the effective heat transfer coefficient of the travelling bead and liquid substrate. We first solved the Young-Laplace equation to obtain the liquid bead shape, which was then used to construct a finite element model. The time-dependent Navier-Stokes equation and the energy equation were then solved to obtain velocity and temperature distributions in the liquid and the surrounding counter-flowing air. The temporal and spatial variations in the temperature of travelling beads are analyzed to evaluate the effective heat transfer coefficients, which are key input parameters for an overall heat exchange model to quantify the heat transfer characteristic of DILSHE.

2.1 Background

Many early studies of liquid film flows on solid surfaces were conducted using plates or tubes of diameters much larger than the film thickness [49]. The Nusselt solution, for example, describes laminar liquid film flows on planar surfaces. Other studies examined thin liquid films flowing down highly curved surfaces. Such flows are always unstable, resulting in wavy patterns [50]. Several theoretical and experimental studies tried to elucidate these instabilities [30, 51], focusing on the interplay among the surface tension, inertia, viscous and gravitational forces. Depending on

the relative importance of these forces, various flow regimes result. The regimes include the drop-like regimes, solitary waves, secondary instabilities, and complex disordered patterns.

Hattori et al. [34] proposed the use of liquid films flowing down on strings for heat and mass transfer applications. By virtue of liquid beads that naturally form as a result of flow instability, the authors argued that one can retain the advantages of spray columns (low pressure drop in the gas stream and large gas-liquid interfacial area per unit volume) while at the same time reduce the bead velocity and thereby increase the gas-liquid contact time. Internal circulations within the beads further enhance heat and mass transfer.

We first experimentally studied the flow characteristics of a non-volatile liquid flowing down a string in the drop-like regime, where traveling beads are formed through the Rayleigh-Plateau (R-P) instability. Using the captured flow characteristics as inputs, we then constructed finite element models and solved the time-dependent Navier-Stokes equation and the energy equation to obtain velocity and temperature distributions in the liquid and the counter-flowing cooling air. The temporal variations in the temperature of travelling beads are next analyzed to evaluate the effective heat transfer coefficients and to assess the accuracy of an approximate one-dimensional model.

2.2 Description of flow regimes

Early studies [29] proposed a flow regime map for thin liquid films flowing down thin vertical strings. The regime map, Figure 2.1, is drawn in the plane R_f/l_c versus $\alpha_N = h_N/R_f$ to facilitate practical use. Here, R_f is the string radius, and l_c is the capillary length of the liquid (e.g., 1.5 mm for Rhodorsil v50 silicone oil). The Nusselt thickness h_N is the thickness of the cylindrical liquid film prior to the onset of any instability, i.e., near the inlet. The aspect ratio α can be varied by

changing the flow rate, independent of the ratio R_f /l_c. This regime map does not account for the dependence of the flow regime on liquid substrate thickness and other complications [28].

The R-P instability of a thin liquid film flowing down a string can be arrested by the mean flow of the film when the film thickness h_N is sufficiently small compared with the ratio R_f^3/l_c^2. The arrest of the growth of the R-P instability by the flow advection was referred to as a saturation mechanism. The saturation number β^* is defined as

$$\beta^* = \left[\frac{3u_N}{2u_i}\frac{\alpha}{(1+\alpha)^4}\right]^{\frac{2}{3}}\left(\frac{l_c}{R}\right)^{\frac{4}{3}} \tag{2.1}$$

The Nusselt average liquid velocity and the maximum velocity at the free interface are denoted as u_N and u_i respectively. The two are all functions of the aspect ratio α and the viscosity of the liquid. Note then that, for a given liquid, β^* is a function only of α_N and R_f/l_c.

The curve of equation $\beta^* = 1$ divides the plane into two regions. At the left hand side of the curve, β^* is larger than 1 and the characteristic time of growth of the R-P instability τ_g is smaller than the characteristic time necessary to displace the waves over their length τ_a. One then expects the R-P instability mechanism dominates over the flow advection. To the left of the curve $\beta^* = \beta_{ca}^* \sim 1.507$ lie the regions where the onset of a self-sustained dynamics of the flow is prompted by an absolute instability [30] of the Nusselt uniform film as opposed to noise-driven convective instability. We experimentally studied three flow conditions within the drop-like regime as shown in Figure 2.1. In this regime, the inertia effect plays a minor role and the Rayleigh-Plateau instability dominates over the Kapitza instability.

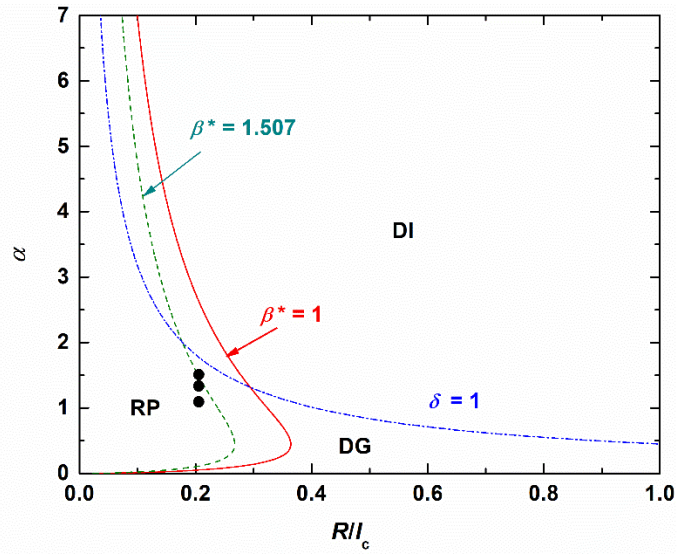

Figure 2.1: Flow regime map proposed in an early study [29]. RP refers to the drop-like regime, DI refers to the drag inertia regime, and DG refers to the drag gravity regime. Three black symbols indicate the experiment conditions used in our study.

2.3 Experimental

2.3.1 Experimental setup

The experimental setup is schematically illustrated in Figure 2.2. A polymer string of a radius R_f = 0.305 mm is vertically suspended using a weight. A liquid is pumped from the storage tank to the top reservoir with the gear pump. The liquid is distributed over the string inside a nozzle head and flows down as an annular film. At the bottom of the string, the liquid is collected in the collection reservoir. After each run, the accumulated liquid is fed back to the storage tank. A precision weighing scale is used to monitor the mass of the collection reservoir and thereby determine the mass flow rate. Three different mass flow rates (0.01, 0.021, and 0.033 g/s) were used in the present work. We used a well-wetting liquid of low surface energy, Rhodorsil silicone

oil (density ρ = 963 kg/m^3, kinematic viscosity ν = 50 mm^2/s, surface tension γ = 20.8 mN/m at 20 °C, thermal conductivity k = 0.15 W/m K, and specific heat c_p = 1507 J/kg K), as received from the vendor. A high frame rate (> 1000 fps) video camera was used to obtain basic geometric parameters of the liquid film flows.

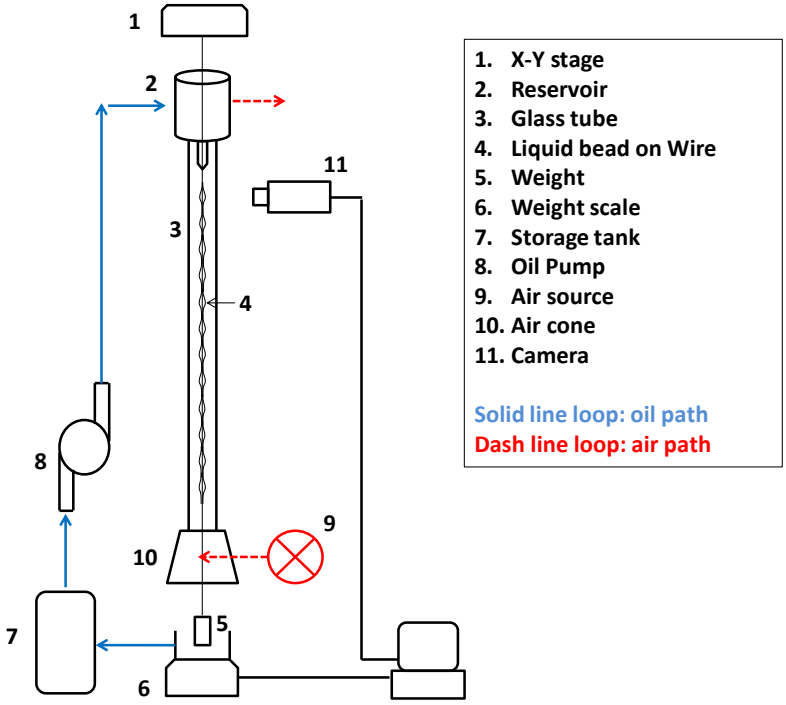

Figure 2.2: A schematic of the experimental setup used to study characteristics of a non-volatile liquid film flowing down a vertical string.

2.3.2 Spatiotemporal diagram

To quantify the characteristics of the wavy liquid film flows, such as the traveling bead shape and speed, we construct spatiotemporal diagrams. At one chosen time step (i.e., video frame), we extract a vertical pixel line that is selected to pass through liquid beads. We repeat this procedure for later time steps at a constant time interval and juxtapose the extracted pixel lines to reveal

spatiotemporal trajectories of the beads. Parallel striations reflect the motion of constant height structures (drops or waves). A sample spatiotemporal diagram obtained from our experiment is shown in Figure 2.3. The slopes of striations and spacing between them reveal the traveling speeds and spatial/temporal frequencies of the beads.

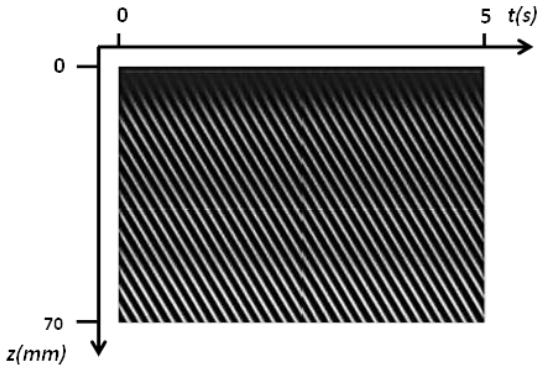

Figure 2.3: A representative spatiotemporal diagram obtained in one of our experiments

2.3.3 Bead profile/shape in the drop-like regime

In the drop-like regime, solitary waves formed by the Rayleigh-Plateau instability resemble isolated drops sliding under gravity on a wetted string. In this regime, $R_f << l_c$ where l_c is the capillary length. The azimuthal surface tension effects therefore dominate over gravity.

As a result, the normalized bead profiles have a nearly generic shape of axisymmetric drops with front-to-back symmetry. The bead length and height scale with the radius of the string.

As shown in Figure 2.4, Following the previous study [34], we quantify the bead profiles in terms of L_b, the longitudinal distance between the maximum curvature points along the bead; R_b, the maximum horizontal dimension of the bead; and R_s, the radius of the cylindrical liquid substrate between two neighboring beads. The effective radius of the bead is then calculated as $R_{eff} = [(4L_b R_b^2)^{1/3}]/2$.

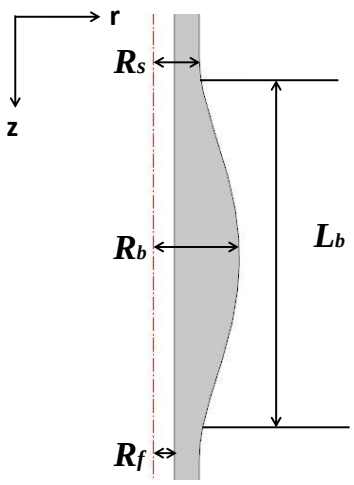

Figure 2.4: The characteristic dimensions of a travelling bead along a vertical fiber

The bead profile in the drop-like regime may be approximated with that of a static liquid drop with zero contact angle sitting on a string coated with a cylindrical liquid substrate [28]. These shapes can be obtained by solving the Laplace equation [52, 53]:

$$-\frac{\ddot{r}}{(1+\dot{r}^2)^{\frac{3}{2}}}+\frac{1}{r(1+\dot{r}^2)^{\frac{1}{2}}}=\frac{\Delta P}{\gamma} \tag{2.2}$$

$$\frac{\Delta P}{\gamma}=\frac{2}{R_s+R_b} \tag{2.3}$$

Here $r = r(z)$ is the distance between the center of the string and the wave profile. The values of R_s and R_b were obtained from experimentally obtained optical images for each mass flow rate. The bead profiles obtained from the Young-Laplace equation are compared with our experimental results in Figure 2.5. The two sets of profiles agree well with each other.

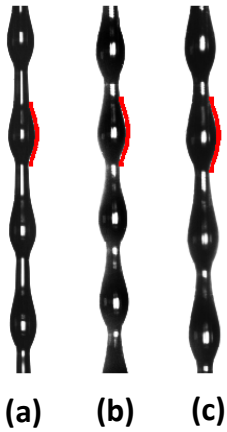

Figure 2.5: The liquid bead profiles obtained by solving the Young-Laplace equation (red solid lines) and those obtained from the optical images taken in our experiments. The mass flow rates are (a) 0.01 g/s, (b) 0.021 g/s, and (c) 0.033 g/s, respectively

The traveling liquid beads are separated from each other by smooth cylindrical liquid films, often referred to as the liquid substrates. The volume flow rate associated with such a smooth cylindrical liquid film of thickness h_s down a vertical string of radius R_f, can be expressed using the Nusselt solution by balancing the viscous and gravitation forces:

$$Q = \frac{2\pi}{3}\frac{g}{\nu}R_f^4\alpha_s^3\frac{3\left[(1+\alpha_s)^4\{4\log(1+\alpha_s)-3\}+4(1+\alpha_s)^2-1\right]}{16\alpha_s^3} \tag{2.4}$$

Here, $\alpha_s = h_s/R_f$ and ν is the kinematic viscosity of the liquid.

Table 2.1 summarizes the bead geometric parameters and the mass flow rates calculated using Eq. (2.4) and the liquid bead volume and speed. The calculated mass flow rates agree with the experimentally measured values to within approximately 10%. The discrepancy is due in part to

uncertainties in the geometric parameters extracted from our image analysis and in part to deficiency in approximating the bead profiles with solutions to the Laplace equation. The fraction of the liquid mass carried by the liquid substrates is small, accounting for only 1-5% of the total mass flow rates.

If a counterflowing gas stream is sufficiently strong such that its dynamic head approaches or exceeds the capillary pressures associated with the surface curvatures of liquid beads and substrates (of the order of 10 Pa for millimeter beads of low surface tension liquids), one expects the bead profiles to be distorted. The present study aims to develop early basic understanding of heat transfer phenomena in the R-P regime. We therefore limit ourselves to situations where such hydrodynamic distortion is negligible.

Table 2.1 Bead geometric parameters and mass flow rates

Measured Mass flow rate (g/s)	0.01	0.021	0.033
R_s (mm)	0.44	0.46	0.52
L_b (mm)	3.86	4.09	4.5
R_b (mm)	0.83	0.88	0.96
R_{eff} (mm)	1.10	1.17	1.27
Bead volume (mm^3)	2.98	3.66	5.88
Air-Bead area (mm^2)	15.8	17.7	21.2
Liquid-bead area (mm^2)	10.2	11.8	14.6
Liquid bead flow rate (g/s)	0.0109	0.0191	0.0351
Liquid substrate flow rate (g/s)	0.00044	0.00069	0.002
Total mass flow rate (g/s)	0.0114	0.0198	0.371
Difference with the experimental data in %	12.5	4.87	11.7

2.4 Numerical simulation

2.4.1 Boundary conditions

We solve the time-dependent Navier-Stokes equation and the energy equation to obtain the velocity and temperature distributions in the liquid and the counter-flowing air. The simulation domain and boundary conditions used to simulate the flows are shown in Figure 2.6. We assume two-dimensional axisymmetric flows. The laminar fully-developed velocity profile from the Nusselt solution is specified at the liquid inlet, which can be expressed as

$$u_x = \frac{g}{\nu}\left[\frac{1}{2}\left(R_f + h_s\right)^2 \log\left(\frac{r}{R_f}\right) - \frac{1}{4}\left(r^2 - {R_f}^2\right)\right] \tag{2.5}$$

Here R_f is the radius of the string, g is the gravity acceleration, ν is the kinematic viscosity of the liquid, r is the radial position, h_s is the cylindrical liquid substrate thickness obtained from our experiments.

At the interface, the zero shear stress and zero normal velocity conditions are specified for the liquid. The velocity continuity condition is applied along the interface between the liquid and the gas (air). The no-slip boundary condition is specified at the string surface. The ambient pressure is specified at the liquid and gas outlets.

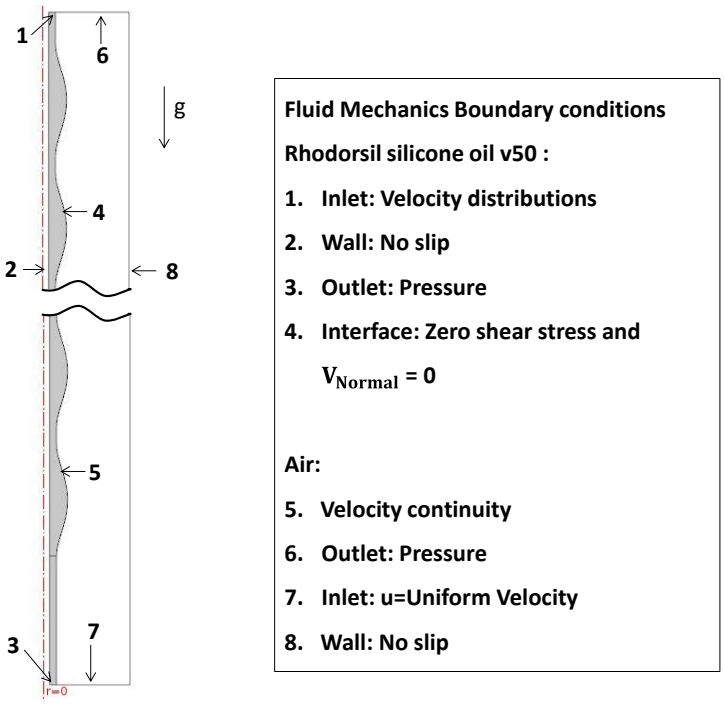

Figure 2.6: The boundary conditions used for the fluid mechanics simulations. The simulation domains included 24 liquid beads uniformly spaced between the liquid inlet and the outlet

We first solved the Navier-Stokes equation in a moving frame traveling at the average bead velocity, and then transferred the solutions back to the stationary frame for heat transfer simulation. The relative gas-liquid velocity is dominated by the gas velocity as the bead velocity is only of the order of 0.01 m/s.

The initial and boundary conditions for the heat transfer simulations are shown in Figure 2.7. The simulation domain is divided into three subdomains: region 7 for the liquid initially at 353.15K, region 8 for the liquid initially at 293.15K, and region 9 for the air initially at 293.15K. Adiabatic boundary conditions are specified at the surfaces of the string and the outer boundary. Uniform temperatures are assigned to the liquid and air inlets. Heat conductions along the string and at the

outlets are neglected. Since non-volatile liquid will be used in DILSHE, liquid evaporation is neglected.

A two-dimensional locally refined mesh of approximately 150000 elements was used for our simulation. The mesh size is varied from 0.00145 mm to 0.126 mm. Adaptive time steps of an upper limit of 0.01 second were used. A mesh independence study was carried out to ensure that the solutions do not change by more than 2% with further mesh refinement

Simulation was first performed with the stationary beads for 1.5 seconds to establish initial flow and temperature distributions. A moving mesh was then employed for region 7 to capture beads traveling along the string. The average bead traveling speeds were obtained experimentally as discussed in Sec. 2.3.2.

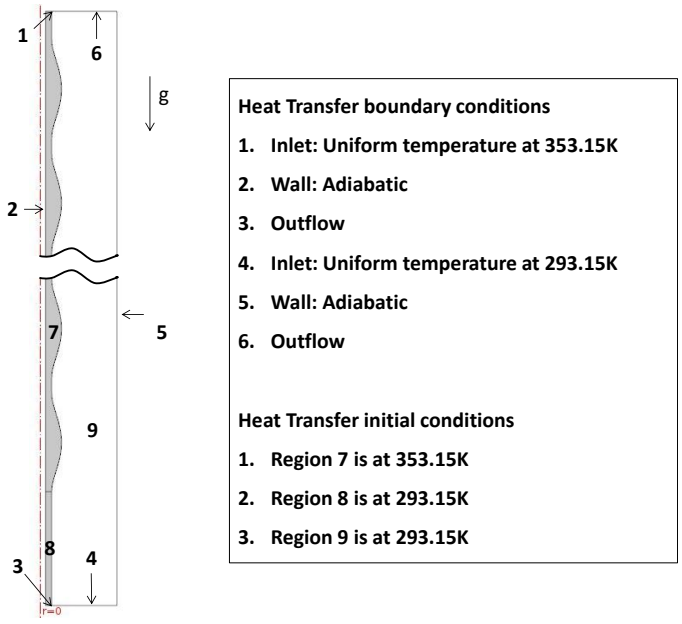

Figure 2.7: The boundary and initial conditions used for the heat transfer simulations. The simulation domains included 24 liquid beads uniformly spaced between the liquid inlet and the outlet

2.4.2 Heat transfer simulation for an array of stationary beads

To independently determine the heat transfer coefficient between the travelling beads and the counterflowing air and between the liquid substrate and the air, we also performed heat transfer simulation using an array of stationary "solid" beads. The boundary conditions used are shown in Figure 2.8. The domain geometry and mesh size are the same as those used for traveling liquid beads for fair comparison.

The effective bead-to-air heat transfer coefficient is evaluated from [54]

$$h_d = \frac{q}{A_s(T_s - T_0)} \tag{2.6}$$

Here, q is the total heat transfer rate from a single bead to the air, A_s is the bead surface area exposed to the air, T_s is the average bead surface temperature, and T_0 is the air inlet temperature.

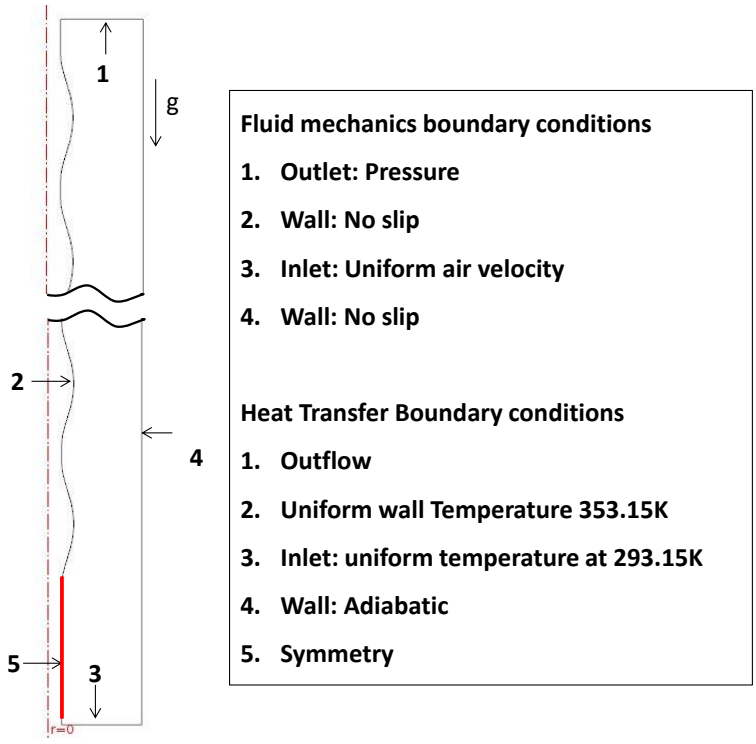

Figure 2.8: The simulation domain and boundary conditions used for heat transfer simulation on an array of stationary beads.

2.5 Results and discussion

2.5.1 Velocity distributions

In Figure 2.9 and Figure 2.10, we plot the velocity magnitude distributions and streamlines predicted in our simulations for three different mass flow rates. The streamlines are presented in a reference frame that is moving at an average bead traveling speed. One can note circulatory fluid motions inside the beads for all three flow rates studied. The liquid beads are subjected to shear stress on the surface of the strings. This causes the formation of internal circulation in each bead, analogous to the vortices that develop inside a drop falling in a viscous medium. The liquid is in

effect partly trapped in the bead, which appears separated from the string by a thin liquid substrate and carries mass while "riding" on the more slowly moving liquid substrate. The recirculation zone decreases somewhat in size with increasing mass flow rates but increases in strength (relative velocity magnitude) with increasing mass flow rates.

The simulation results also show that the maximum flow velocity in the liquid substrate is less than the value calculated from the Nusselt solution for a liquid film of the same thickness. For the 0.01 g/s case, the predicted velocity is 0.0015 m/s while the corresponding Nusselt solution is 0.002 m/s. This observation is consistent with the results in an independent numerical simulation study [55].

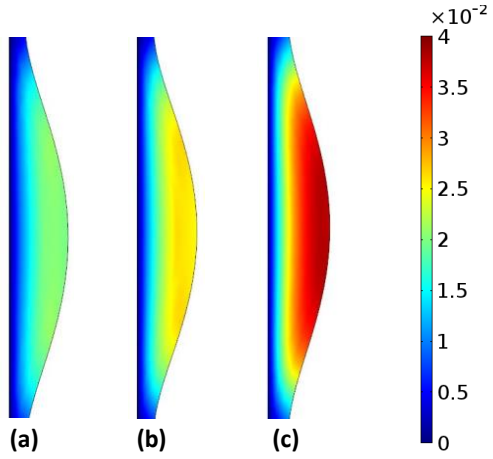

Figure 2.9: The predicted velocity magnitude profiles for three different liquid mass flow rates: (a) 0.01 g/s, (b) 0.021 g/s, and (c) 0.033g/s.

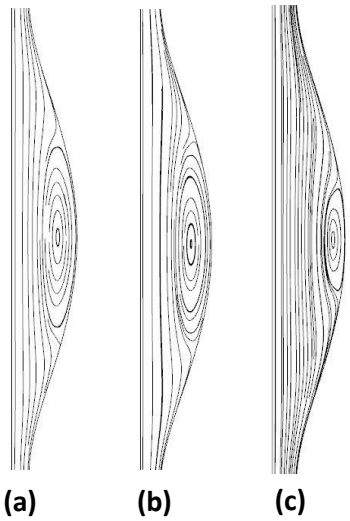

Figure 2.10: The predicted streamlines in a reference frame moving at the average bead traveling speed for the three different liquid mass flow rates as in Figure 2.9

2.5.2 Temporal bead temperature profiles

The temporal variations in the average bead temperatures are shown in Figure 2.11 for the case with a liquid mass flow rate of 0.01 g/s. The other two cases of higher mass flow rates show qualitatively similar behavior.

For the first 1.5 sec, the beads were held stationary and their cooling is due primarily to convection heat transfer to the counter-flowing air (air cooling dominant). As the beads start moving, they exchange thermal energy with both the air and the slower moving and "cold" liquid substrate. This switch leads to significant changes in the cooling rates.

The leading bead experiences the highest cooling rate because it encounters the coldest part of the liquid substrate in the front. As the downstream liquid substrate and air gradually heat up with each passing liquid bead, the subsequent beads exhibit smaller cooling rates. For beads that were initially far removed from the cold liquid substrate downstream, a quasi-steady state is established

where the temperature varies only with respect to axial locations. This region is amenable to a simple analytical model [34].

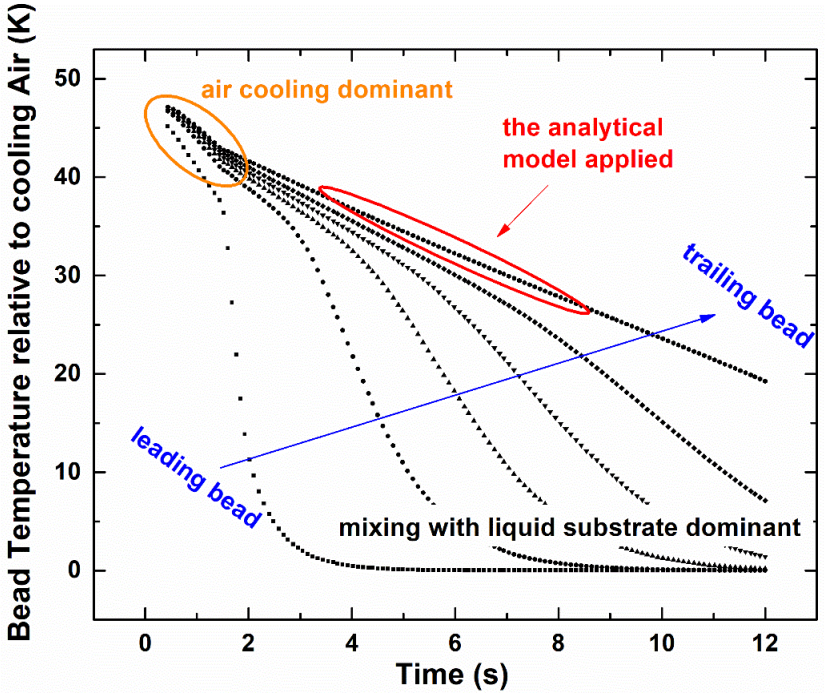

Figure 2.11: Temporal variations of the average bead temperature for six travelling beads. The total liquid mass flow rate is 0.01 g/s.

2.5.3 Approximate Analytic Model for the Liquid Bead Temperatures

Hattori et al. [34] proposed an approximate model to predict the evolution of the average temperature of travelling beads and the quasi-steady state liquid substrate temperature distribution. Assuming complete mixing between a local liquid substrate and a travelling bead as it travels down the string, one can write the energy conservation equation for a liquid bead

$$\rho_l c_{pl} V_d{}' \frac{dT_d{}'}{dt} = A_d h_d (T_G - T_d{}') + \rho_l c_l S_s (U_d - U_s)(T_s{}' - T_d{}') \tag{2.7}$$

and the quasi-steady state temperature distribution for the liquid substrate:

$$\frac{T_{s2}{}'(x)-T_{d1}{}'(x+2R_{eff}-U_s\tau_{sg})}{T_G-T_{d1}{}'(x+2R_{eff}-U_s\tau_{sg})} = 1-\exp\left(-\frac{2\pi R_s h_s \tau_{sg}}{\rho_l c_l S_s}\right) \tag{2.8}$$

Here, $V_d{}'$ is the combined volume of the travelling bead and the local liquid substrate underneath, A_d is the bead surface area exposed to the air, S_f is the surface area of the annular liquid substrate per unit length of the string, U_d is the bead average velocity, U_s is the average flow velocity in the liquid substrate. ρ_l and c_{pl} are the density and specific heat of the liquid, respectively. $T_s{}'$ is the liquid substrate temperature just ahead of the travelling bead and $T_d{}'$ is the average temperature of the combined bead and the liquid substrate underneath. Referring to Figure 2.12, we define τ_{sg} as the time period over which the liquid substrate is exposed to the air as it rebuilds from the rear of a previous bead and reaches the next bead:

$$\tau_{sg} = \frac{U_d\tau-2R_{eff}}{U_d-U_s} \tag{2.9}$$

Here, τ is the inverse of the temporal frequency of the travelling bead.

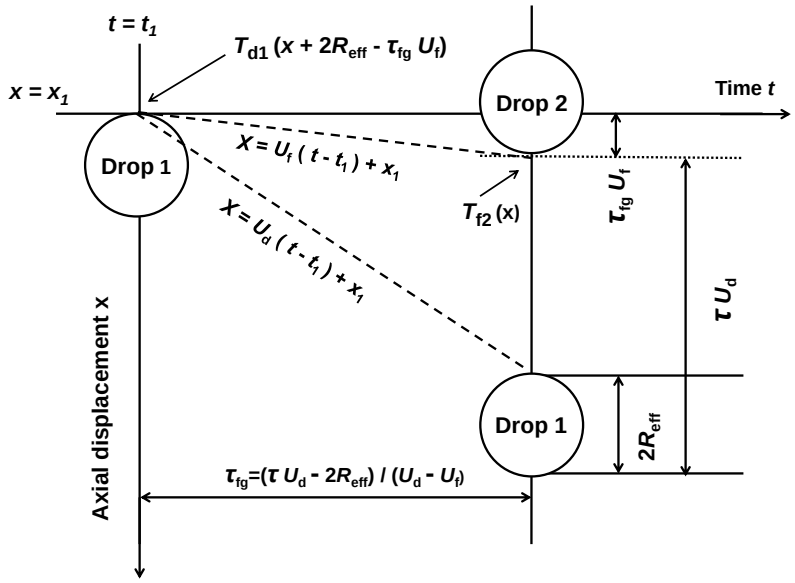

Figure 2.12: A schematic illustration of droplet progression used to develop an analytic model for the bead and liquid substrate temperature distributions

By iteratively solving Eqs. (2.7-2.8), we obtain $T_d{}'$ as the average bead temperatures as the bead travels down the string and $T_s{}'$ as the quasi-steady state liquid substrate temperature distribution along the string.

As defined earlier, h_d is the effective bead-to-air heat transfer coefficient and h_s is the average liquid substrate-to-air heat transfer coefficient. These two parameters are independently determined from steady-state simulations performed on an array of stationary beads as discussed in Sec. 2.4.2.

Figure 2.13 compares the liquid bead-to-the air heat transfer coefficients at a liquid mass flow rate of 0.01 g/s for three different air inlet velocities (0.2 m/s, 0.6 m/s and 1.0 m/s). The leading bead exhibits the largest heat transfer coefficient. As we move toward the air outlet, the thermal boundary layer grows and the heat transfer coefficient decreases, approaching approximately constant values. The three dash lines correspond to the results from an independent previous

numerical simulation study [56] of convective heat transfer over a linear array of eight spheres of spacing comparable to our beads. The two sets of results agree reasonably well with each other.

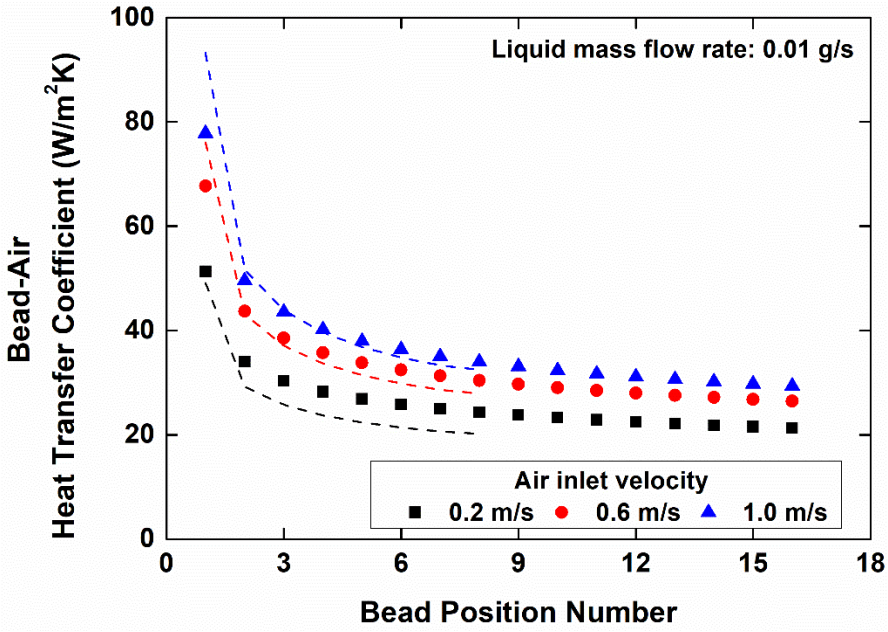

Figure 2.13: Numerically predicted liquid bead-to-air Heat transfer coefficients as a function of the bead position for a liquid mass flow rate of 0.01 g/s for three air inlet velocities: 0.2 m/s, 0.6 m/s, and 1.0 m/s.

The liquid bead-to-air heat transfer coefficients are also predicted for different liquid mass flow rates with different bead profiles and spacings. Figure 2.14 shows the results.

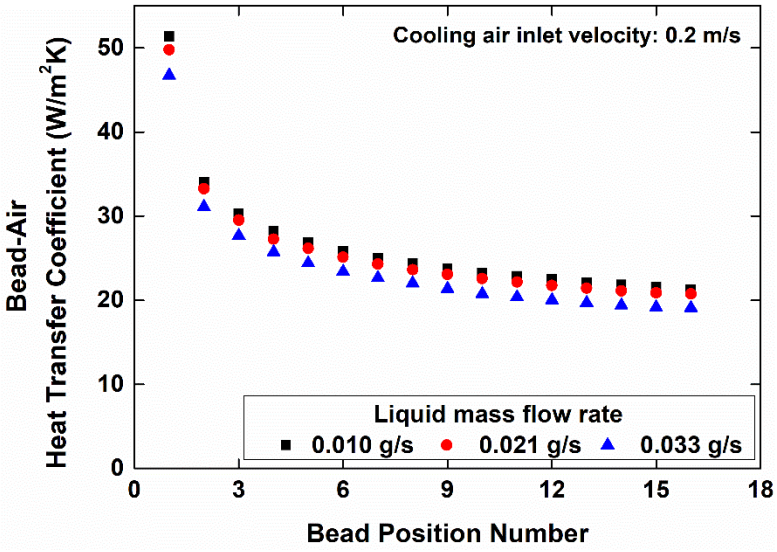

Figure 2.14: Numerically predicted liquid bead-to-air heat transfer coefficients as a function of the bead position for an air inlet velocity of 0.2 m/s for three liquid mass flow rates: 0.01 g/s, 0.021 g/s, and 0.033 g/s.

The liquid substrate-to-air heat transfer coefficient was obtained from the simulations. Figure 2.15 compares the heat transfer coefficients for a liquid mass flow rate of 0.01 g/s for three different air inlet velocities. The results exhibit similar trend as the liquid bead-to-air heat transfer coefficients, but the absolute values are smaller.

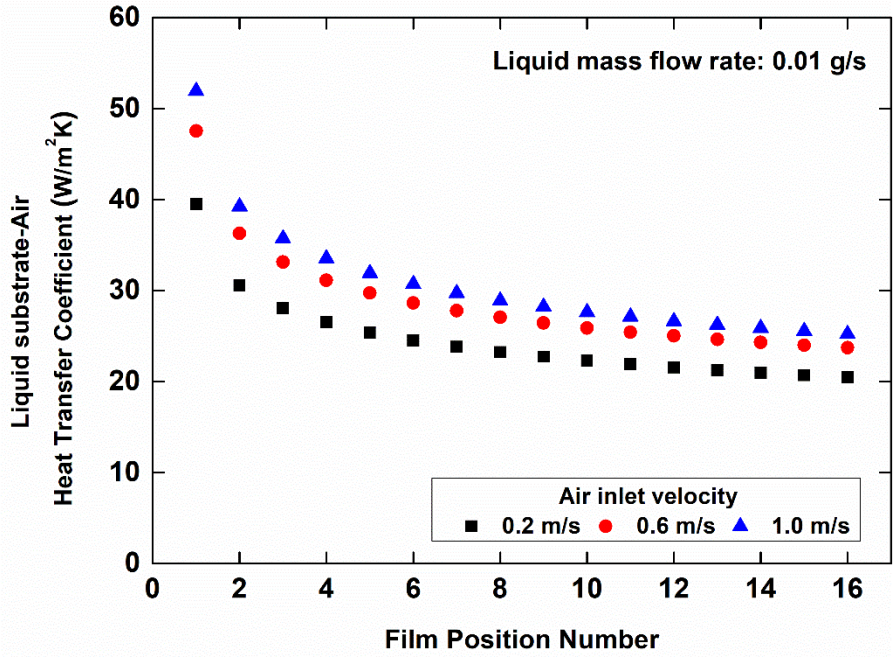

Figure 2.15: Numerically predicted liquid substrate-to-air heat transfer coefficients as a function of the bead position for a liquid mass flow rate 0.01 g/s for three different air inlet velocities: 0.2 m/s, 0.6 m/s, and 1.0 m/s.

Figure 2.16 compares the normalized temporal temperature profiles of the average bead temperature obtained from our numerical simulation and those obtained from the approximate analytic model. We note that the numerical simulation considered only a finite train of liquid beads whereas the approximate analytic model considered an infinite train of liquid beads. We consider only beads far removed from the leading end in our numerical simulation results such that the liquid substrate has established a quasi-steady state distribution as assumed in the analytic model. The two predicted profiles agree reasonably well with each other, suggesting that the assumption of complete mixing is reasonable due to strong internal flows within liquid beads and relatively flow rates of the liquid substrate.

Figure 2.16 shows results for three different air velocities. Higher convective heat transfer rates and hence higher cooling rates are reflected in the steeper slope of the profiles at higher air velocities.

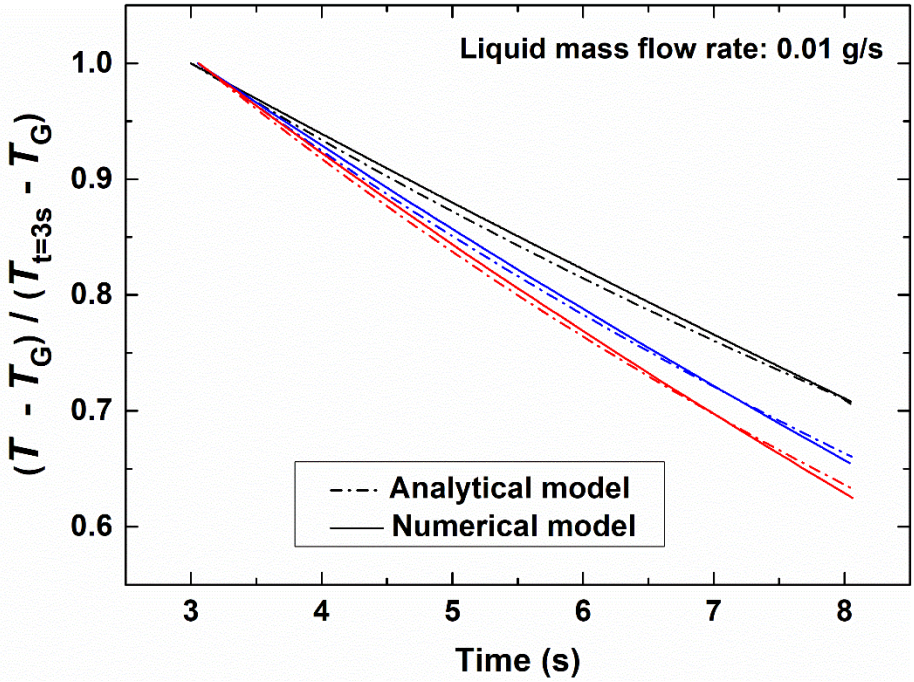

Figure 2.16: The temporal variations in the normalized average bead temperature predicted using either numerical simulation (solid lines) or the analytic model (dashed lines). The results are presented for different air inlet velocities of 0.2 m/s (black line), 0.6 m/s (blue line) and 1.0 m/s (red line).

2.6 Summary

In summary, we constructed a numerical model to study heat transfer phenomena for liquid films falling over highly curved surfaces in the drop-like flow regime dominated by the Rayleigh-Plateau instability. We experimentally characterized the travelling bead geometric parameters, which were then incorporated into our numerical simulation model to predict velocity distributions

and temporal variations in the temperature of travelling liquid beads. Our numerical simulation results agree well with the prediction from an analytical model for the evolution of the average bead temperature, when combined with independently predicted liquid bead-to-air and liquid substrate-to-air heat transfer coefficients. The present work helps establish foundation for a systematic design and optimization of a new generation of dry cooling systems.

CHAPTER 3

Experimental study of heat transfer between thin liquid films flowing down a vertical string in the Rayleigh-Plateau instability regime and a counterflowing gas stream

The previous chapter discusses using a moving mesh method to predict the temperature profile of the liquid film with imported film shape in the experiment. In this chapter, we experimentally examine the flow and heat transfer characteristics of thin liquid films flowing down strings of a diameter approximately 0.1 mm against a counterflowing air stream. Numerical simulations are also performed to help interpret and validate our experimental results. The relationship between flow characteristics and heat transfer effectiveness are examined experimentally for different combinations of the air velocities, liquid mass flow rates, and nozzle radii. We show that the liquid mass flow rate and the air velocity are two primary factors influencing heat transfer effectiveness whereas details of the liquid flow instability affect local bead-to-air heat transfer coefficients. We also compare the heat transfer effectiveness and the pressure drop between a wetted string column that consists of an array of vertical strings and a well-established structured packing that consists of vertical plates. The multi-string column is shown to deliver comparable heat transfer performance but at a lower air pressure drop than the structured packing.

3.1 Background

Many experimental studies focus on investigating heat transfer performance of a turbulent liquid film around a uniformly heated tube [40–48]. Shmerler et al. [41, 42] measured the wall heat flux

and temperature gradients across the liquid films to develop correlations for the normalized liquid-side heat transfer coefficients and the Reynolds number. These experiments focused on subcooled liquid films or saturated liquid films undergoing evaporation. However, very few studies were reported on heat transfer characteristics of liquid films flowing down thin strings with a counterflowing gas. A previous study [7] reported a rather limited experimental investigation of the cooling of thin films of a heated silicone oil flowing down single strings. By using strings with different diameters, they successfully achieved the string-of-bead flow and annular film flow at the same liquid flow rate, and demonstrated that the string-of-bead flow exhibited a higher overall heat transfer coefficient than the annular film flow. However, the impact of the air velocity, liquid flow rate and nozzle radius on liquid film flow characteristics, and the relationship between the flow characteristics and heat transfer effectiveness still need further investigations.

To rigorously understand the flow and heat transfer characteristics of thin liquid films flowing along strings, we previously experimentally studied the fluid dynamics of thin silicone oil film flowing down a vertical string against a counterflowing air stream. We demonstrated that the liquid flow rate and air velocity were two primary factors affecting the flow characteristics [57]. We then constructed a numerical model based on the geometric parameters obtained from our experiments to predict velocity distributions and temporal variations in temperature of liquid beads [58]. The simulation results of the average bead temperature evolution agree well with the prediction from an analytical model [34].

3.2 Description of flow regimes

Previous studies [28, 29] suggested a flow regime map for thin liquid films flowing down a vertical string. The regime map (Figure 3.1) is presented in the plane R_w/l_c versus $\alpha = h_N/R_w$ to facilitate practical use. Here, R_w is the string radius, and l_c is the capillary length of the liquid (e.g., 1.5 mm for Rhodorsil v50 silicone oil). Here ρ and γ denote the liquid density and surface tension, respectively. The Nusselt thickness h_N is the thickness of a cylindrical liquid film one would have for a given liquid flow rate in the absence of any instability. The aspect ratio α, which is independent of the ratio R_w/l_c, can be varied by changing the liquid flow rate. This approximate regime map does not account for the influence of the liquid substrate thickness and other complications [28].

The RP instability can be arrested by the mean flow when the film thickness h_N is sufficiently small compared with the ratio R_w^3/l_c^2. This arrest of the growth of the RP instability by the flow advection, often referred to as saturation [29], is characterized by the saturation number β^*:

$$\beta^* = \left[\frac{3u_N}{2u_i}\,\frac{\alpha}{(1+\alpha)^4}\right]^{\frac{2}{3}}\left(\frac{l_c}{R}\right)^{\frac{4}{3}} \tag{3.1}$$

Here, the Nusselt average liquid velocity and the maximum velocity at the free interface are denoted as u_N and u_i respectively. The two are in turn functions of the aspect ratio α and the viscosity of the liquid. Note that, for a given liquid, β^* is a function only of α and R_w/l_c.

The curve representing $\beta^* = 1$ approximately divides the plane into two regions. On the left-hand side of the curve, β^* is larger than 1 and the characteristic time of growth of the RP instability

is smaller than the characteristic time necessary to displace the waves over their length. One then expects the RP instability mechanism to dominate over the flow advection [30]. By analyzing the dispersion relation of traveling beads/waves, one can determine $\beta^* \approx 1.507$ as a more refined characteristic number defining transition between the absolute instability of the Rayleigh-Plateau instability regime and the convective instability.

We focus in the present study on the RP regime that exhibits the absolute instability where a uniform train of traveling liquid beads are observed along the entire length of a string. his greatly facilitates interpretation of our heat transfer characterization experiments. The black symbols in Figure 3.1 represent the liquid flow rates studied in this article, ranging from 0.03 g/s to 0.09 g/s.

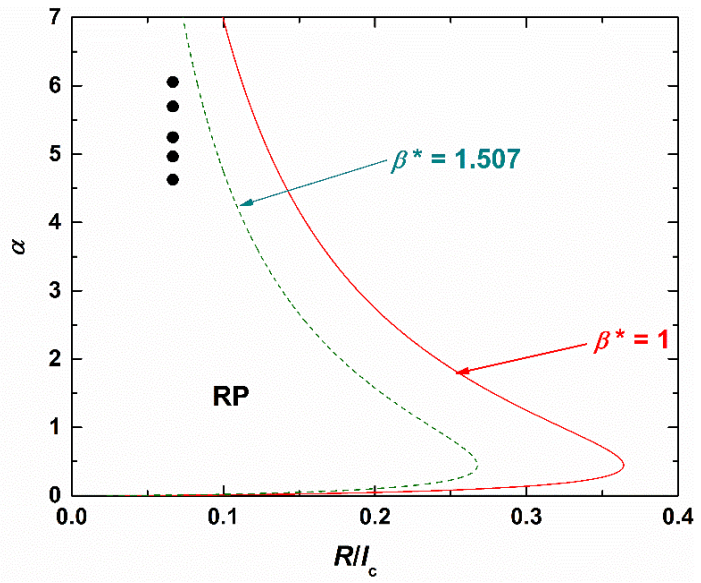

Figure 3.1: A flow regime map proposed in an early study [29]. The regime map is constructed for v50 silicone oil. RP refers to the drop-like regime dominated by the Rayleigh-Plateau instability. Black symbols indicate the experiment conditions used in our study.

3.3 Experimental setup and numerical model

3.3.1. Experimental

Figure 3.2 shows a schematic of the experimental setup used in the present study. The setup consists of a vertical glass tube (inner diameter = 10.2 mm), a top liquid reservoir, a polymer string and an air cone. The polymer string (R_w = 0.1 mm) with a weight attached at the end is suspended along the glass tube. The string is aligned using a X-Y stage to be concentric with a circular nozzle attached to the bottom of the liquid reservoir (Figure 3.3). An electrical heater is used to heat the liquid inside the reservoir before it enters the nozzle. After exiting the nozzle, the liquid flows along the string and is then collected at the bottom container. The collected liquid is fed back to the top reservoir using a gear pump.

Compressed air (inlet pressure ~ 1.3 bar, temperature ~ 22 °C) is fed into the glass tube from the bottom. The converging cone at the bottom of the glass tube is fitted with a flow straightener to ensure uniform air distribution. A variable-area flow meter is used to measure the volumetric air flow rate. A high speed video camera (capable of up to 16000 fps) is used to record liquid film profiles. These high-speed video recordings are analyzed using a custom made imaging processing code to extract the geometric parameters of the liquid films. The liquid nozzle radius, R_n (Figure 3.3) is one of the parameters that influence the liquid bead size and spacing. We use nozzles with three different radii, 0.4 mm, 0.5 mm, and 0.6 mm, in the present study. The uncertainty in nozzle radius measurement is ± 0.02 mm.

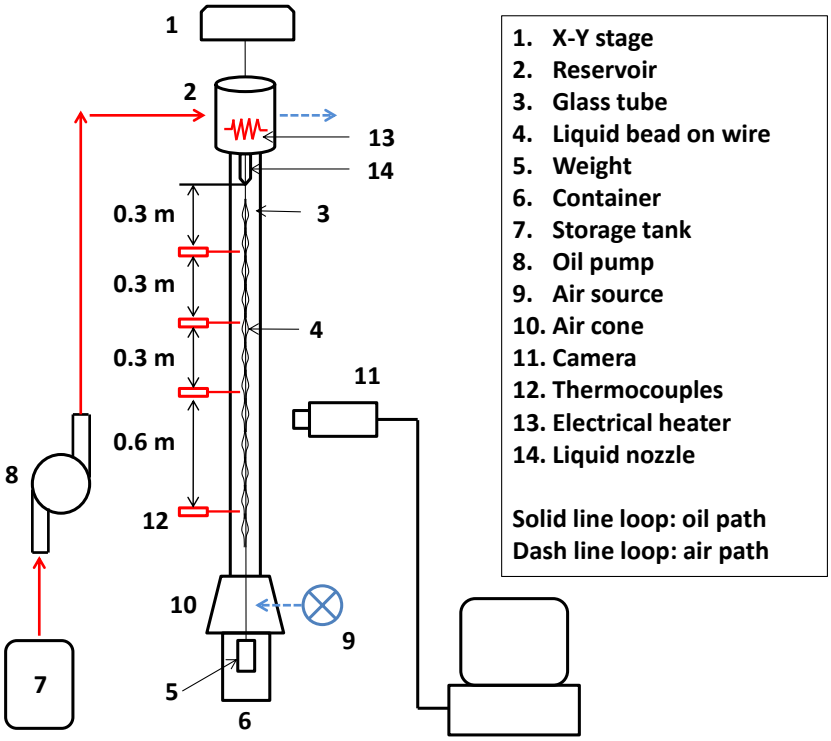

Figure 3.2: Schematic of the experimental setup used to study flow and heat transfer characteristics of a non-evaporating liquid film flowing down a vertical string.

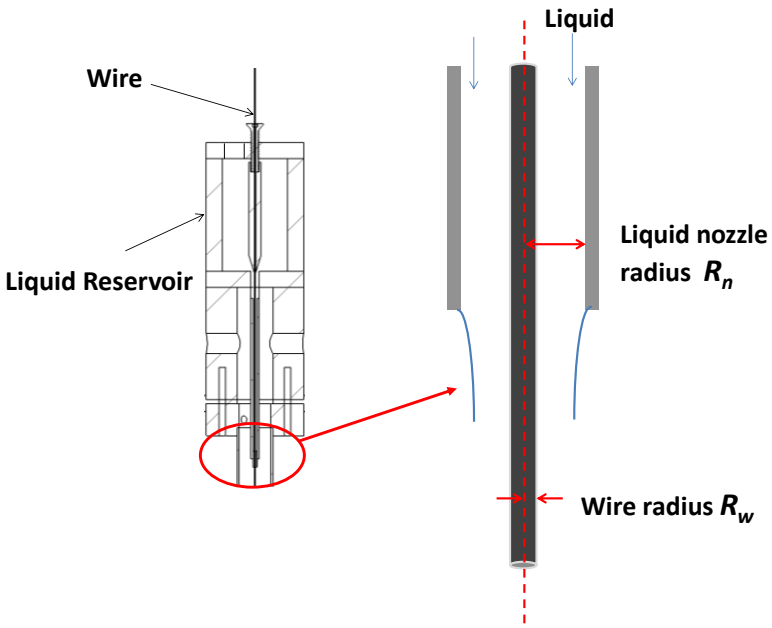

Figure 3.3: An enlarged view of the top liquid reservoir and the liquid nozzle

Four micro-thermocouples of diameter 250 μm are placed at axial locations 0.3 m, 0.6 m, 0.9 m, and 1.5 m from the nozzle to measure liquid temperatures. The thermocouples are mounted on the shafts of micro-positioners so that we can adjust their positions to coincide with the center of traveling liquid beads. Outputs from the thermocouples are monitored using a 24-bit high-precision data acquisition system. The power applied to the heater is adjusted for each flow rate such that the liquid temperature at the first thermocouple location is maintained at 37 °C.

A micro-thermocouple located at a fixed position is "immersed" to temporally varying extents in the liquid as a train of liquid beads travel past that location. Fast Fourier transform of the temporal temperature recordings therefore yields well-defined frequencies, which correlate well with liquid bead traveling frequencies obtained from video recordings as discussed further in Section 3.4.2.

We use a well-wetting liquid of low surface energy, Rhodorsil v50 silicone oil. Its key properties are: density ρ = 963 kg/m^3, kinematic viscosity ν = 50 mm^2/s, surface tension γ = 20.8 mN/m at 20 °C, thermal conductivity k = 0.15 W/(m·K), and specific heat c_p = 1507 J/(kg K).

The liquid mass flow rate is calculated from the geometric parameters of the liquid beads and liquid substrates obtained through image analyses. In an independent set of experiments, we confirmed that the liquid mass flow rates measured using a weight scale placed under the bottom collection container agreed with those obtained using image analyses to within 10%. The average air velocity in the glass tube is calculated from the measured volumetric flow rates.

Following a previous study [34], we quantify the liquid profiles in terms of R_b, the longitudinal distance between the centerline and the maximum curvature point along the bead; R_s, the radius of the cylindrical liquid substrate between two neighboring beads; and L, the distance between two adjacent travelling beads. Figure 3.4 schematically illustrates these geometric parameters for a representative case.

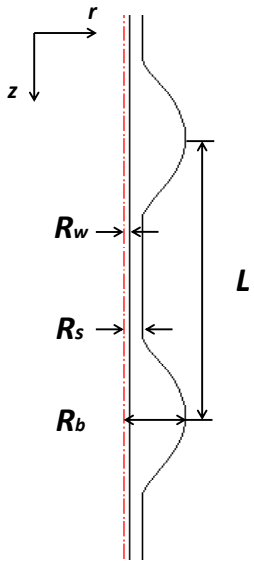

Figure 3.4: Geometric parameters of liquid beads traveling along a string on a thin liquid substrate.

The uncertainty in the geometric parameters obtained through optical image analyses is estimated to be ± 0.03 mm. For each run, we typically analyze 3000 images for the bead radius, liquid substrate radius, and spacing between two subsequent beads. The uncertainty in the air velocity is estimated to be 0.1 m/s and the uncertainty in thermocouple readings ± 0.1°C.

3.3.2. Numerical Model

To help interpret and indirectly validate our experimental data, we construct a quasi-steady model for heat transfer between the liquid film and the counterflowing air. We note that the mean velocities of air are at least an order of magnitude higher than those of liquid beads in all our experiments. In view of this, our model assumes that liquid beads are stationary and considers only relative air flows. We further assume two-dimensional axisymmetric flows.

Our experimental results are used to specify geometric parameters in the model: the thickness of the liquid film, the length and maximum radius of the liquid beads, and the spacing between beads. In an earlier work [59], it proved that the profile of liquid beads in the drop-like regime can be well-approximated by that of a static liquid drop placed on a string coated with a cylindrical liquid substrate. We also solve the Laplace equation to obtain the liquid bead profile using the experimentally determined liquid substrate thickness and maximum bead radius as input parameters [58].

A commercial computational fluid dynamics package was used for our simulation. The simulation domain and the relevant boundary conditions are summarized in Figure 3.5. We solve

the steady state Navier-Stokes equations and the energy equations, Eqs. (3.2-3.4), to obtain velocity fields and temperature distributions in both the liquid film and the air.

$$\rho(\boldsymbol{u}\cdot\nabla)\boldsymbol{u} = \nabla\cdot[-p\boldsymbol{I} + \mu(\nabla\boldsymbol{u} + (\nabla\boldsymbol{u})^T)] + \boldsymbol{F} \tag{3.2}$$

$$\rho(\nabla\cdot\boldsymbol{u}) = 0 \tag{3.3}$$

$$\rho C_P\boldsymbol{u}\cdot\nabla T = \nabla\cdot(k\nabla T) \tag{3.4}$$

Here, $\boldsymbol{u}$ and T are the velocity and temperature fields, respectively. p is the pressure. $\boldsymbol{I}$ is the unit tensor. $\boldsymbol{F}$ denotes the gravitational force. C_p is the heat capacity at constant pressure, k the thermal conductivity, ρ the density, and μ the dynamic viscosity.

The Navier-stokes equations are first solved to obtain the velocity fields. These were then input into the energy equation to obtain the temperature distributions. The velocity fields of the liquid and the air are coupled by the interface boundary conditions. At the liquid-gas interface, the zero shear stress condition, Eq. (3.5), the zero normal velocity condition, Eq. (3.6), and the tangential velocity continuity condition Eq. (3.7) are applied.

$$\tau_l = \tau_g = 0 \tag{3.5}$$

$$\boldsymbol{u_l}\cdot\boldsymbol{n} = \boldsymbol{u_g}\cdot\boldsymbol{n} = 0 \tag{3.6}$$

$$\boldsymbol{u_l} - (\boldsymbol{u_l}\cdot\boldsymbol{n})\boldsymbol{n} = \boldsymbol{u_g} - (\boldsymbol{u_g}\cdot\boldsymbol{n})\boldsymbol{n} \tag{3.7}$$

Here, $\boldsymbol{n}$ represents the normal vector. $\boldsymbol{u_l}$ and $\boldsymbol{u_g}$ denote the velocity fields in the liquid and the air, respectively.

The adiabatic condition ($-\boldsymbol{n}\cdot\boldsymbol{q} = 0$) and the no-slip boundary condition ($\boldsymbol{u}_l = 0$) are applied at the string surface. An isothermal wall condition is applied at the glass tube wall based on our experimental observation that there were negligible temperature variations along the glass tube wall. The ambient pressure is assigned at the outlets of the liquid and the gas. Heat conduction along the string and at the outlet is neglected.

A two-dimensional locally refined triangular mesh of approximately 240,000 elements was used for our simulation. The element size is varied gradually from 0.005 mm in the liquid substrate to 0.1 mm in the air. A mesh independence study was carried out to ensure that the liquid film temperatures do not change by more than 3% with further mesh refinement.

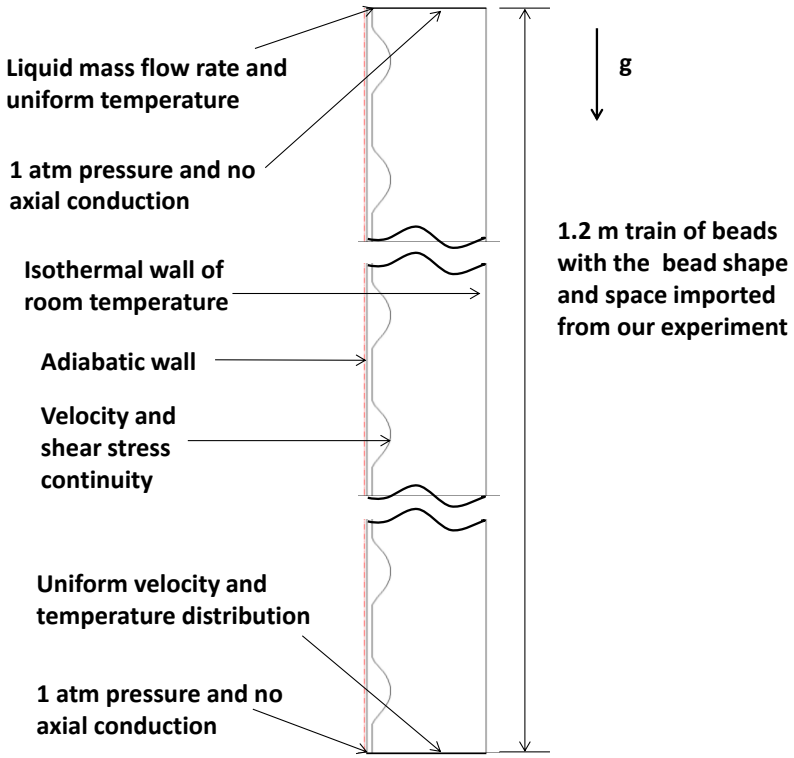

Figure 3.5: The simulation domain and boundary conditions for our quasi-steady model. All the geometric parameters of the liquid films are those obtained from the experiments

3.4 Results and discussion

3.4.1. Spatiotemporal diagrams

To help quantify the flow characteristics of liquid films, we first construct a spatiotemporal diagram [51] from acquired video images. Briefly, at one chosen time step (i.e., video frame), we extract a vertical line of pixels, which is selected to pass through roughly the centers of liquid beads. We repeat this procedure for subsequent time steps at a constant time interval and then juxtapose the extracted pixel lines to reveal spatiotemporal trajectories of the beads.

Two representative spatiotemporal diagrams obtained from our experiment are shown in Figure 3.6. Striations in the spatiotemporal diagram reflect the motions of constant height structures (i.e., traveling liquid beads). The spacing between adjacent striations in the *z*-direction corresponds to the spatial frequency of traveling beads. The spacing between adjacent striations in the *t*-direction corresponds to the temporal frequency. The slope of each striation represents the traveling velocity of each corresponding liquid bead.

In the RP instability regime, a series of parallel striations is observed along the entire length of a string, indicating that no coalescence of liquid beads takes place.

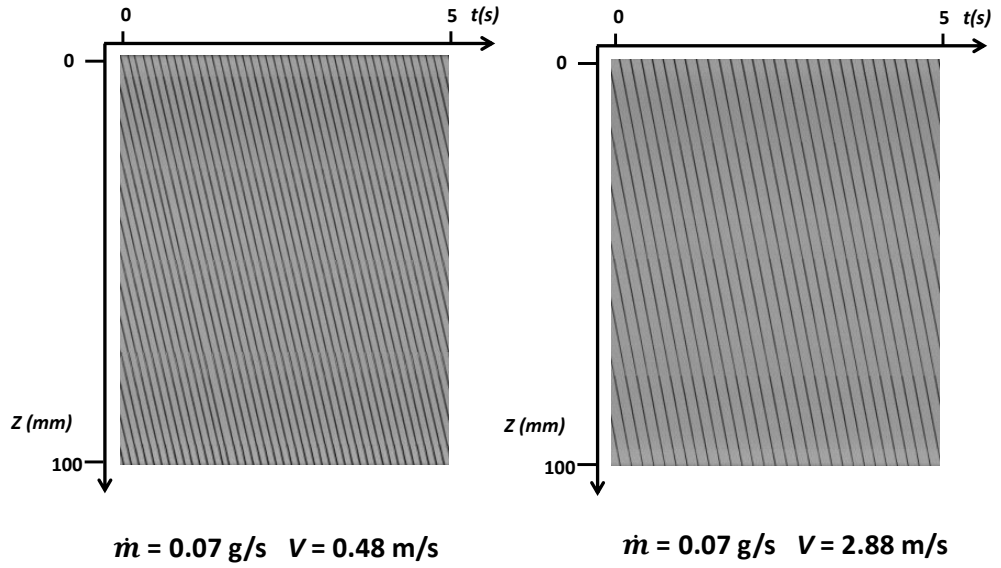

Figure 3.6: Two spatiotemporal diagrams with the same liquid flow rate but different air velocities.

3.4.2 Liquid bead radius and frequency

A counterflowing air stream exerts aerodynamic drag on liquid beads and influences liquid film flow patterns. Comparing the two spatiotemporal diagrams shown in Figure 3.6, for example, we note that the bead (spatial and temporal) frequencies are lower for the higher air velocity.

Figure 3.7 shows a set of optical images of liquid beads obtained at different air velocities for a fixed liquid mass flow rate. The bead radius R_b increases slightly as the air velocity V_{air} increases up to approximately 3 m/s. As the aerodynamic drag deforms the liquid beads, their frontal areas increase, further increasing the drag force. As the motion of the liquid beads becomes retarded, their volumes become larger, increasing the gravitational force to counteract the drag force. This increase in the liquid volume in turn leads to increase in the spacing between two adjacent beads and hence the bead frequency. That is, the liquid beads become bigger but fewer. The liquid bead

radii and spatial frequency extracted from our image analysis are shown in Figure 3.8, Figure 3.9, and Figure 3.10.

As the air velocity is increased even further, the air streams turn turbulent. The liquid beads deform appreciably and may even be pushed upward by strong aerodynamic drag. We limit our heat transfer characterization to laminar air flows.

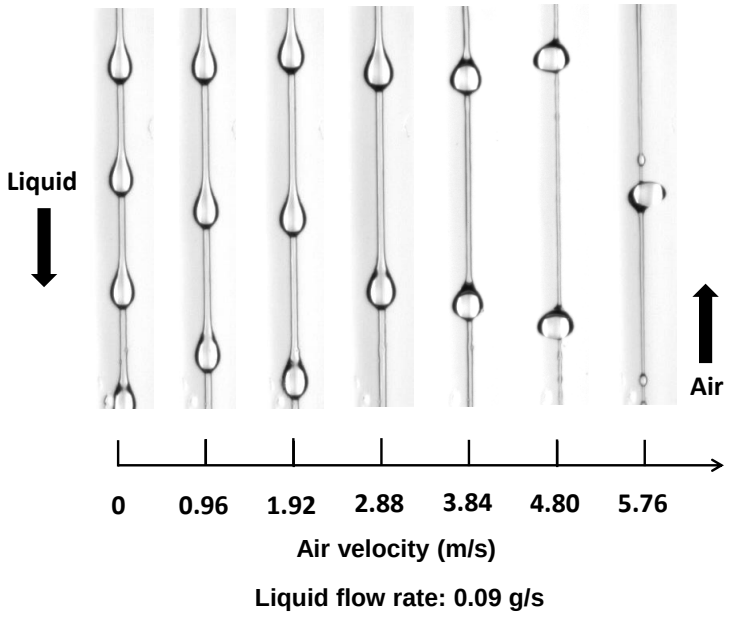

Figure 3.7: Optical images of liquid film flows at different velocities of counterflowing air streams. The liquid flow rate is fixed at 0.09 g/s.

Figure 3.8 quantitatively shows variations in the liquid bead radius R_b as a function of the air velocity. The liquid mass flow rate $\dot{m}_L$ is varied from 0.05 g/s to 0.09 g/s by using nozzles with different values of the inner radius R_n.

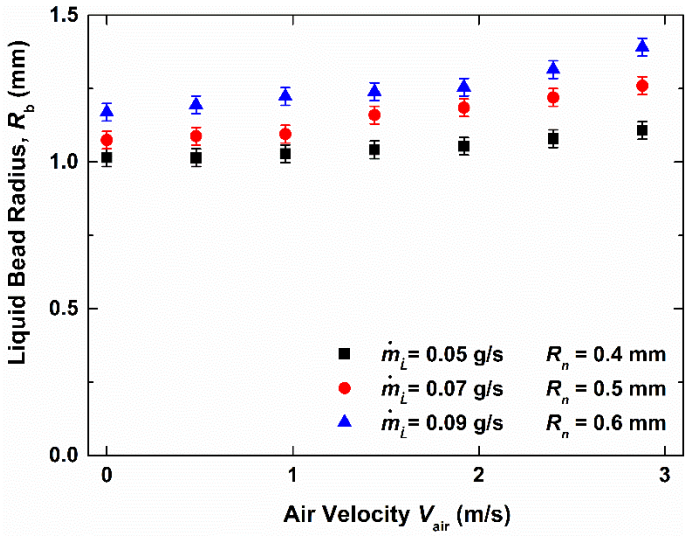

Figure 3.8: Experimental results for the liquid bead radius, R_b, as a function of the air velocity, V_{air}. Three different liquid mass flow rates are achieved using nozzles of different radii

One can also vary the liquid mass flow rate by adjusting the height of the liquid column in the top liquid reservoir while keeping R_n constant. Figure 3.9 compares the measured values of R_b from a set of experiments where we vary the mass flow rate in this manner for two nozzles of different radii (0.4 and 0.5 mm). For a given nozzle radius, the measured bead radii at two different mass flow rates remain within 5% of each other. In contrast, at a fixed mass flow rate of 0.05 g/s, the measured bead radius for the nozzle with R_n = 0.5 mm (triangles) is larger than that for the nozzle with R_n = 0.4 mm (squares). The impact of these changes in liquid flow patterns on heat transfer will be discussed later.

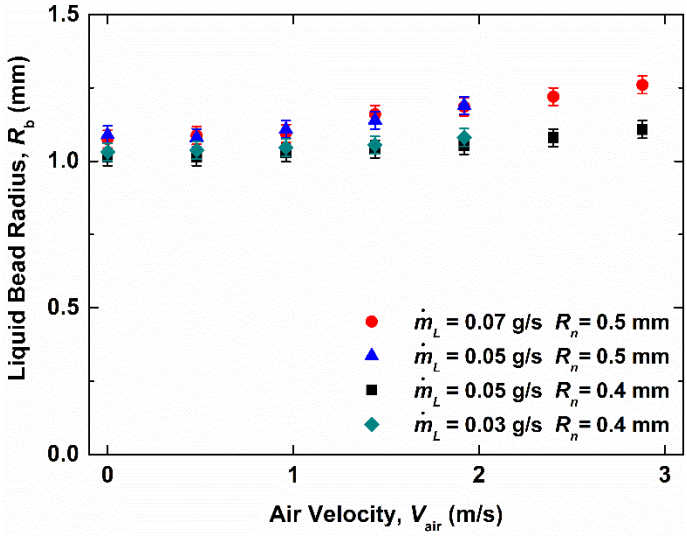

Figure 3.9: Variations in the liquid bead radius R_b for different combinations of the nozzle radii and liquid mass flow rates. A 0.4 mm-radius nozzle is used for liquid flow rates of 0.03 g/s and 0.05 g/s. A 0.5 mm-radius nozzle is used for liquid flow rates of 0.05 g/s and 0.07 g/s. Both the 0.4 mm- and 0.5 mm-radii nozzles are used to generate a liquid mass flow rate of 0.05 g/s.

Figure 3.10 quantitatively shows that the liquid bead frequency generally decreases with the increasing air velocity. More importantly, as the liquid bead size changes with the decreasing nozzle radius, from 0.5 mm (triangles) to 0.4 mm (circles), for a fixed mass flow rate of 0.05 g/s, the frequency of liquid beads changes in order to keep the mass flow rate constant. Figure 3.10 also shows that, for a given nozzle radius (R_n = 0.4 mm), the smaller mass flow rate of 0.03 g/s (squares) leads to the smaller bead frequency than the larger flow rate of 0.05 g/s (circles).

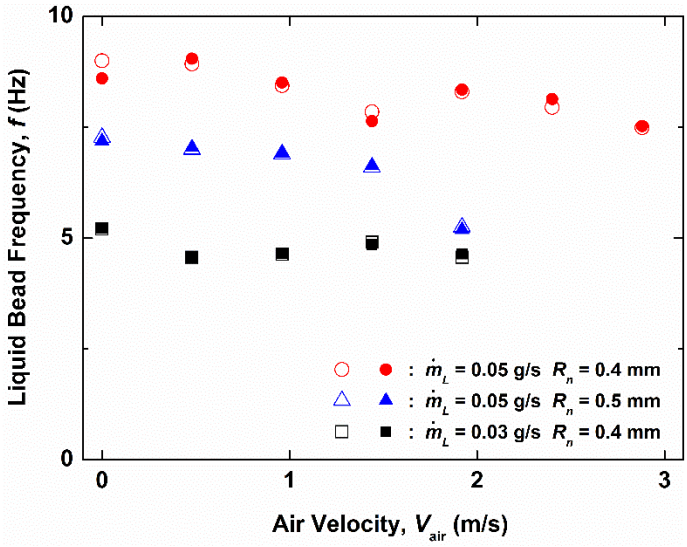

Figure 3.10: The dependence of the bead frequency on the air velocity for liquid mass flow rates of 0.03 g/s and 0.05 g/s. The frequencies are obtained either through optical image analyses or through FFT of temporal temperature recordings. The solid symbols correspond to the results from FFT, and the hollow symbols to the result from image analysis

Although the bead radius R_b increases with increasing V_{air}, the liquid substrate radius R_s (see Figure 3.4) remains nearly unaffected by the air flows. We estimate the liquid substrates account for less than 5% of the total liquid mass flow rate under the present experimental conditions.

A previous study [60] used liquids with different values of surface tension and made qualitatively similar observations. That is, for liquids with both high and low surface tension, the liquid bead radius increased with increasing gas loads whereas the liquid substrate thickness remained nearly unchanged. Large differences in the liquid flow rates and the resulting differences in the bead size and dominant instability mechanism, however, make direct quantitative comparison with the previous study difficult.

3.4.3. Bead velocity

Figure 3.11 shows the liquid bead velocity V_b as a function of V_{air} for two nozzles with different radii. V_b is relatively insensitive to the air velocity for small liquid beads. V_b can be expressed as $V_b = L \times f$, where L is the spacing between two adjacent liquid beads and f is the temporal bead frequency. Changes in the two parameters tend to offset each other as V_{air} increases.

The bead velocities measured for $\dot{m}_L$ of 0.03 g/s and 0.05 g/s are nearly the same when the nozzle radius is fixed at 0.4 mm. However, for a nozzle of 0.5 mm radius, V_b slightly increases with increasing V_{air} for a given $\dot{m}_L$ and with increasing $\dot{m}_L$ for a given V_{air}. This can be attributed to the fact that larger liquid beads are more susceptible to aerodynamic drag.

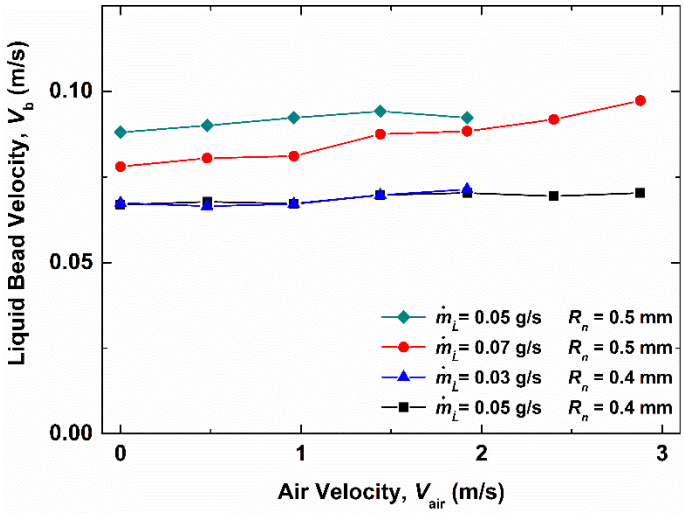

Figure 3.11: The experimentally measured liquid bead velocity as a function of the air velocity. Four different liquid flow rates obtained using two different radii nozzle are shown. Note that the error bars are small compared with the plotted symbol.

3.4.4. Overall heat transfer effectiveness

Figure 3.12 shows the temperature drops measured at different axial locations as a function of V_{air}. The liquid mass flow rate is set to be 0.05 g/s. The liquid temperature at 0.3 m from the nozzle exit (set to be z = 0) is fixed at 37 °C and this value is used as the reference temperature in calculating the temperature drops. The temperature drops increase with increasing V_{air}. This is due in part to enhanced forced convection and in part to increased spacing between liquid beads. The effect of spacing between adjacent liquid beads on heat transfer is further discussed later (Section 3.4.5). The experimental results agree well with our simulation results.

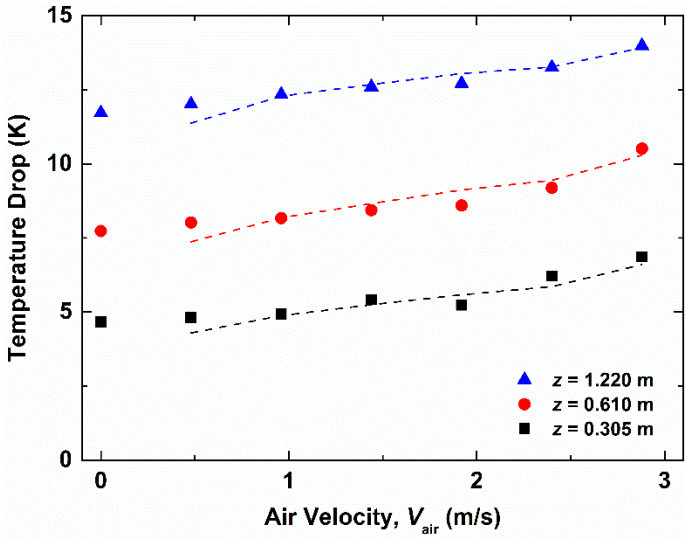

Figure 3.12: Temperature drops measured as a function of the air velocity at three different axial locations. The liquid mass flow rate is 0.05 g/s. The solid symbols are experimental data. The dash lines are our simulation results. The uncertainties are smaller than the plotted symbols.

We use the "*local*" heat transfer effectiveness [61] at a specific downstream axial location to further quantify the heat transfer performance:

$$\varepsilon_{\text{local}} = \frac{C_L(T_{L0} - T_L(z))}{C_{min}(T_{L0} - T_G)} \tag{3.8}$$

Here, T_{L0} denotes the inlet liquid temperature, and T_G denotes the air temperature. We note that the mean air temperature remains nearly constant at 22 °C along the axial direction due to a relatively large glass tube diameter and hence air volume flow rates. The "*local*" heat transfer effectiveness is then only a function of the liquid heat capacity rate, C_L, the minimum heat capacity rate, C_{min}, and the liquid temperature at a specific axial location, $T_L(z)$. In all the cases considered in our work, $C_{min} = C_L$. The inlet liquid temperature and the inlet gas temperature are both fixed in all our experiments. We can therefore calculate the "*local*" heat transfer effectiveness using the liquid temperature profile alone.

Figure 3.13 shows the calculated heat transfer effectiveness as a function of the axial position *z* for different liquid mass flow rates. The experimental results agree well with the predictions from our quasi-steady heat transfer model. For a given V_{air}, the local heat transfer effectiveness $\varepsilon_{\text{local}}$ improves as the liquid mass flow rate decreases, which is consistent with the general behavior of counterflow heat exchangers.

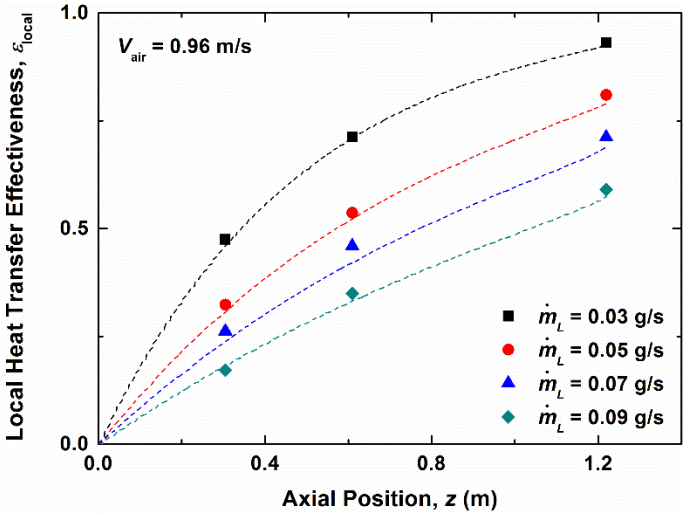

Figure 3.13: The local heat transfer effectiveness as a function of the axial position. Four different liquid flow rates are examined. The symbols are experimental data and the dash lines represent our simulation results.

As noted before, a nozzle with a smaller radius generally produces smaller but more liquid beads than a nozzle with a larger radius at a fixed liquid mass flow rate. We examine the impact of this behavior on the heat transfer effectiveness. Our experimental results, shown in Figure 3.14, indicate that the heat transfer effectiveness is rather insensitive to the liquid bead size (R_n = 0.4 mm versus R_n = 0.5 mm). Due to internal recirculation flows within liquid beads and hence efficient internal mixing [7, 29, 34], the details of liquid film profiles play a rather minor role. The total liquid mass flow rate is the dominant factor affecting the heat exchanger effectiveness. The same trends are observed for both air velocities (0.96 and 1.92 m/s) examined.

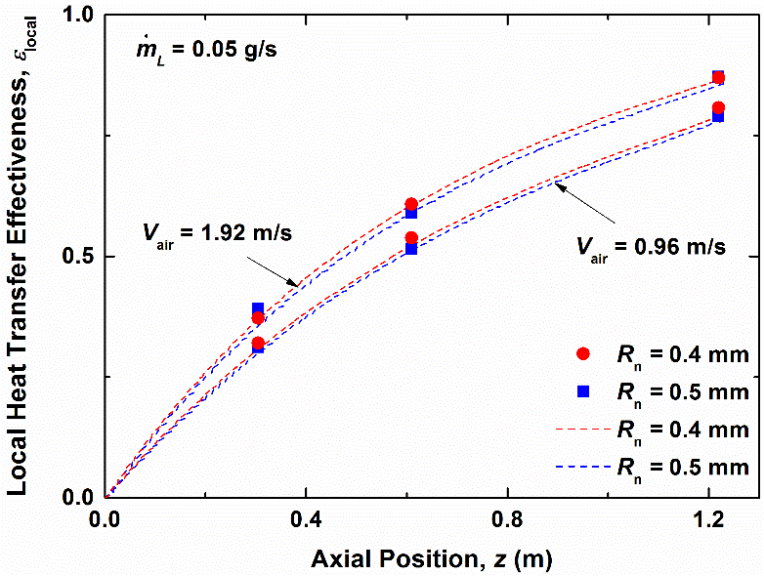

Figure 3.14: Comparison of the local heat transfer effectiveness between the case with R_n = 0.4 mm and the case with R_n = 0.5 mm for the same liquid flow rate of 0.05 g/s. Two sets of results with different air velocities (0.96 m/s and 1.92 m/s) are shown. The symbols are experimental data and the dash lines are simulation results

3.4.5 Bead-to-air heat transfer coefficient

Although the two cases with different nozzle radii discussed above deliver the same "local" heat transfer effectiveness ε_{local}, "local" heat transfer coefficients for convective heat transfer between individual liquid beads and air h can still differ. To examine this further, we use a lumped capacitance analysis [54] to estimate the liquid bead-to-air heat transfer coefficient:

$$\frac{T-T_G}{T_{Lo}-T_G} = \exp\left[\left(-\frac{hA_s}{\rho Vc}\right)\frac{z}{v}\right] \tag{3.9}$$

Here, A_s represents the surface area of a liquid bead and V represents its volume. ρ and c represent the density and the specific heat of the liquid, respectively. v represents the liquid bead velocity and h represents the liquid bead-to-air heat transfer coefficient. Eq. (3.9) is used to fit the measured axial temperature distribution and extract h.

Figure 3.15 shows the liquid bead-to-air heat transfer coefficients, h, obtained for the same two cases with different nozzle radii at a fixed $\dot{m}_L$ of 0.05 g/s. The heat transfer coefficient h is larger for the bigger nozzle radius at a given $\dot{m}_L$ and a given V_{air}. A larger surface area of liquid beads exposed to the air and a larger inter-bead spacing lead to enhanced heat transfer for liquid film flows produced by the bigger nozzles.

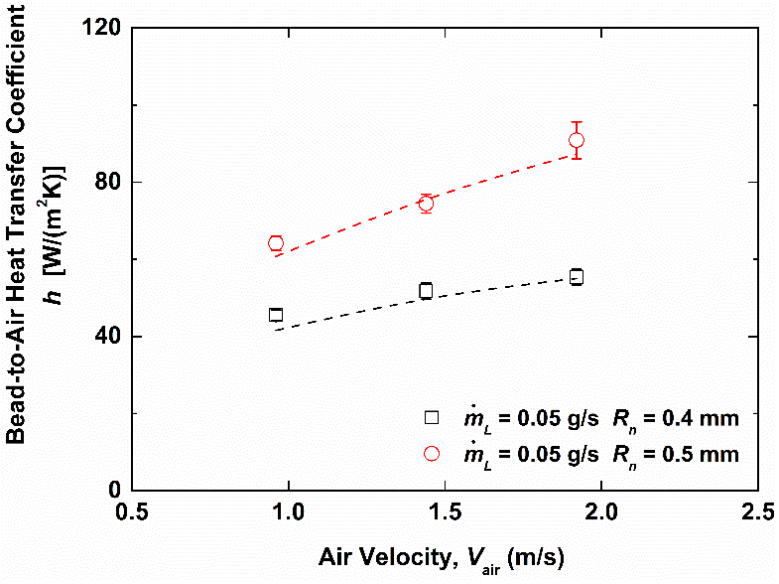

Figure 3.15: The liquid bead-to-air heat transfer coefficient obtained from the lumped capacitance analyses. The results from the two nozzles with different radii (0.4 mm and 0.5 mm) are shown. The liquid flow rate, ṁL, is fixed at 0.05 g/s are compared. The symbols are experimental data and the dash lines are simulation results.

When the inter-bead spacing is changed, the heat transfer rate is also changed due to the influence of recirculation/ wake zones formed in the inter-bead region [62]. Figure 3.16 compares representative streamlines and temperature profiles obtained in our numerical simulation for two cases with the same liquid bead size but different inter-bead spacing values (and hence different mass flow rates). At the larger inter-bead spacing, the flow separation angle (measured from the forward stagnation point) increases and the recirculation zone narrows in width. This then leads to increased radial temperature gradients and hence local heat transfer rates. A similar trend of enhanced heat transfer with increased inter-sphere spacing values was observed in an earlier study of linear arrays of spheres [56].

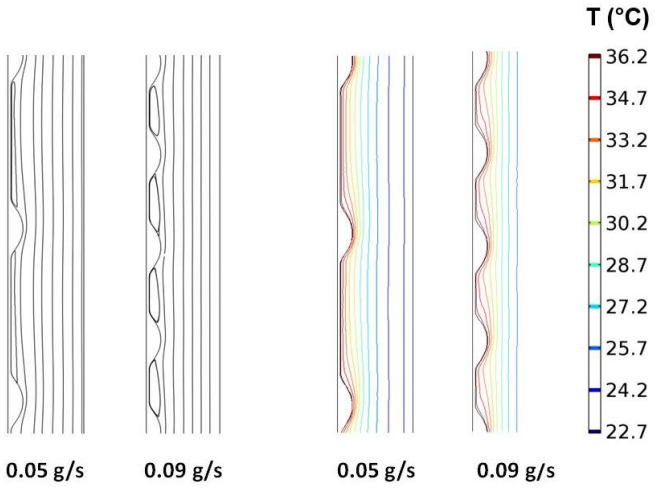

Figure 3.16: The predicted streamlines (left) and temperature profiles (right) for liquid film flows with the same liquid bead size but with different inter-bead spacing values

Figure 3.17 compares the heat transfer coefficients obtained from two different mass flow rates for a fixed nozzle radius R_n. Under the conditions used, the liquid bead size and the bead traveling velocity remains nearly unchanged, whereas the inter-bead spacing is larger for the smaller liquid

mass flow rate. And indeed, the lower mass flow rate leads to enhanced bead-to-air heat transfer coefficients.

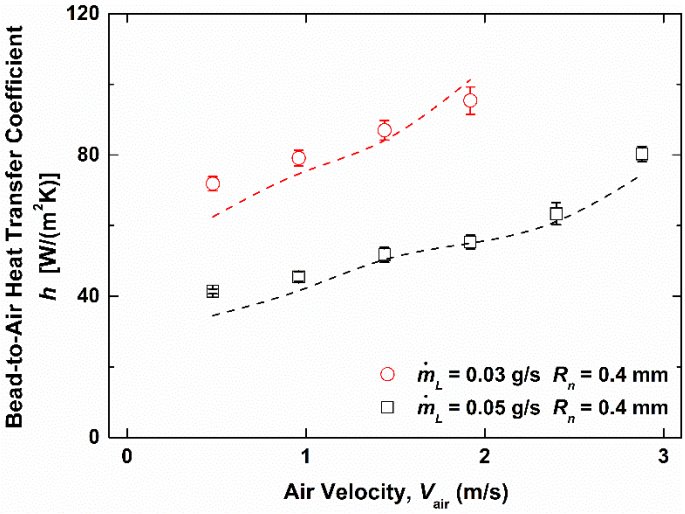

Figure 3.17: The liquid bead-to-air heat transfer coefficients as a function of the air velocity. The nozzle radius is fixed while the liquid flow rate is changed from 0.03 g/s to 0.05 g/s by adjusting the liquid heads in the reservoir. The symbols are experimental data.

Combining Eq. (3.8) and Eq. (3.9), we rewrite the "local" heat transfer effectiveness as

$$\varepsilon_{\text{local}}(z) = 1 - \exp\left[\left(-\frac{hA_s}{\rho V c}\right)\frac{z}{v}\right] \tag{3.10}$$

This offers one way to visualize how the heat transfer effectiveness for liquid films is nearly independent of the nozzle radii for a given value of $\dot{m}_L$. Changes in the heat transfer coefficient h and the liquid bead velocity are counteracted by changes in the liquid volume and hence thermal capacitance of liquid beads.

3.4.6. The comparison with a structured packing

Liquid films falling down the surfaces of vertical plates or large-diameter tubes have been widely used for mass and heat transfer applications. Comparing heat transfer performance of these "planar" liquid films with that of liquid films flowing down on small-diameter strings is not straightforward as one must account for system-level constraints (for example, total cross-sectional area/volume).

For an illustrative purpose, we compare the heat exchange effectiveness and the gas-phase pressure drop in two different direct-contact heat exchangers. One consists of an array of wetted strings (our system) and the other incorporates a vertical plate structured packing [3, 63, 64] (Figure 3.18). The two systems have the same overall dimensions: 1 m wide, 1 m long and 1.2 m tall.

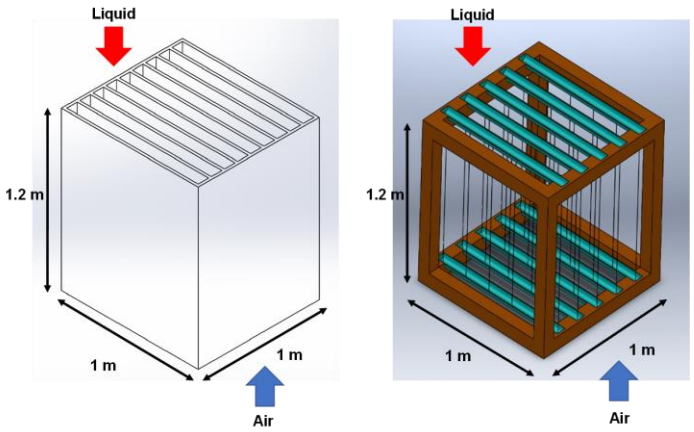

Figure 3.18: The schematics of a wetted string column (left) and a vertical plate structured packing (right).

We keep the superficial liquid velocity $V_L = \dot{m}_L/(\rho_L A_f)$, and the superficial air velocity $V_G = \dot{m}_G/(\rho_G A_f)$ the same for both systems. Here, $\dot{m}_L$ and $\dot{m}_G$ denote the total inlet liquid and air mass

flow rate, respectively. ρ_L and ρ_G denote the liquid and air density, respectively. A_f is the column cross-sectional area (1 m^2).

For our wetted string column system, the string pitch is selected to be 10 mm, resulting in a total of 10,000 strings in the unit. For the vertical wall structure packing, we also choose the same mm pitch (p = 10 mm). The plate thickness t is set to be 1 mm such that the total thickness (plate and liquid films) is comparable to that for the wetted strings. The air flow is in the laminar regime.

For the wetted string array, we use 3D numerical simulation over a square unit cell to predict the overall heat exchanger effectiveness ε and pressure drop.

$$\varepsilon = \frac{C_l(T_{L,in} - T_{L,out})}{C_{min}(T_{L,in} - T_{G,in})} \tag{3.11}$$

For a vertical plate structured packing, the heat exchanger effectiveness and the pressure drop are evaluated using the empirical correlations for the heat transfer coefficients and friction factor [3, 65–67]. The heat exchanger effectiveness, and pressure drop for a vertical wall structured packing are evaluated based on the empirical correlations. The overall heat transfer coefficient, U of the structured packing is determined to evaluate the heat exchanger effectiveness of the system. The overall heat transfer coefficient is defined as Eq. (3.12) [54]

$$\frac{1}{U} = \frac{1}{h_G} + \frac{1}{h_L} \tag{3.12}$$

Here, h_G and h_L represent the air side heat transfer coefficient and liquid side heat transfer coefficient respectively. The following empirical correlations can determine the air side heat transfer coefficient [63].

$$Re_G = \frac{\left(\frac{\dot{m}_G}{A_c}\right)D_h}{\mu_G} \tag{3.13}$$

$$Re_L = \frac{4\Gamma}{\mu_L} = \frac{2\left(\frac{\dot{m}_L}{A_f}\right)p}{\mu_L} \tag{3.14}$$

$$A_c = A_f\left(1 - \frac{t+2\delta}{p}\right) \tag{3.15}$$

$$D_h = 2[\,p - (\,t + 2\delta)\,] \tag{3.16}$$

$$Nu_G = \frac{h_G D_h}{k_G} = 0.00814 {Re_G}^{0.83} {Pr_G}^{0.44} {Re_L}^{0.15} \tag{3.17}$$

$$\delta = 0.909 {Re_L}^{\frac{1}{3}} \left(\frac{{\upsilon_L}^2}{g}\right)^{\frac{1}{3}} \tag{3.18}$$

Here Re_G and Re_L denote gas-side Reynolds number and liquid-side Reynolds number. Pr_G is the Prandtl number for gas. D_h is the hydraulic diameter defined as Eq. (3.16). p represents the distance between two plates. δ denotes the liquid film thickness, and t the plate thickness. A_c is the flow cross-section area while A_f denotes the column cross section area which in our case is 1 m^2. k_G is the thermal conductivity of air, μ_L and ν_L are respectively the dynamic and kinematic viscosity of the liquid.

The liquid side heat transfer coefficient can be obtained from the following empirical correlations. Since the Re_L is smaller than 30 in all cases, the liquid film along the plate is in laminar regime [63].

$$St_L = \frac{h_L}{C_{pL}(\upsilon_L g)^{1/3}} = 0.233 Re_L^{\frac{2}{3}} Pe_h^{-\frac{1}{2}} \quad (3.19)$$

$$Pe_m = \frac{u_\delta H}{\alpha_L} \quad (3.20)$$

$$\frac{u_\delta}{(\upsilon_L g)^{1/3}} = 0.413 Re_L^{\frac{2}{3}} \quad (3.21)$$

Here Pe_h is the heat transfer Peclet number, which is defined as Eq. (3.19). u_δ is the film surface velocity and can be determined from empirical Eq. (3.21). H is the packing column height and α_L is the thermal diffusivity of liquid.

The following empirical correlations are used to obtain the friction factor to calculate the pressure drop for structured packings for the present study [67]. f is the friction factor. C and n are the constant which can be determined by Eqs (3.23 and 3.24). δ^* and $D_h{}^*$ are the normalized film thickness and hydraulic diameter. These two terms have been normalized with respect to the capillary length defined as Eq. (3.27)

$$f = 4(0.005 + C\delta^{*n}) \quad (3.22)$$

$$log_{10} C = -0.56 + \frac{9.07}{D_h{}^*} \quad (3.23)$$

$$n = 1.63 + \frac{4.74}{D_h{}^*} \quad (3.24)$$

$$\delta^* = \frac{\delta}{L_c} \quad (3.25)$$

$$D_h{}^* = \frac{D_h}{L_c} \quad (3.26)$$

$$L_c = [\frac{\sigma}{(\rho_l - \rho)g}]^{1/2} \quad (3.27)$$

Figure 3.19 shows the heat exchanger effectiveness of both the array of wetted strings and the structured packing as a function of the superficial air velocity. Two different superficial liquid velocities, consistent with our experimental values for a single string, are examined. Figure 3.19 shows that the array of wetted strings has generally higher heat exchanger effectiveness values than the structured packing. At the higher liquid superficial velocity, the heat exchanger effectiveness is lower for both systems. For the lower V_L, especially at sufficiently high air velocities, the two systems exhibit nearly identical heat transfer performance.

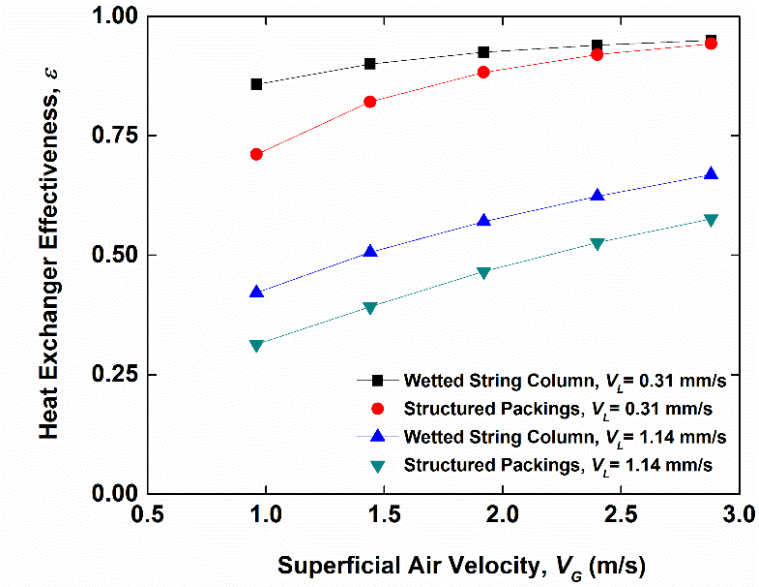

Figure 3.19: The comparison of the heat exchanger effectiveness between the array of wetted strings and the vertical plate structured packing under the same gas and liquid supply conditions

In contrast to the heat transfer performance, the air pressure drops of the two systems show significant difference (Figure 3.20). At a given superficial liquid velocity, the air pressure drop along the structured packing is almost one order of magnitude higher than that along the wetted

string column. This is consistent with the observations of prior studies [36, 37]. We also note that the air pressure drop along the array of wetted string is less sensitive to the superficial liquid velocity than the structured packing. This is in part because the fraction of the cross-sectional area available for air flows varies less for the array of wetted strings than the structured packing.

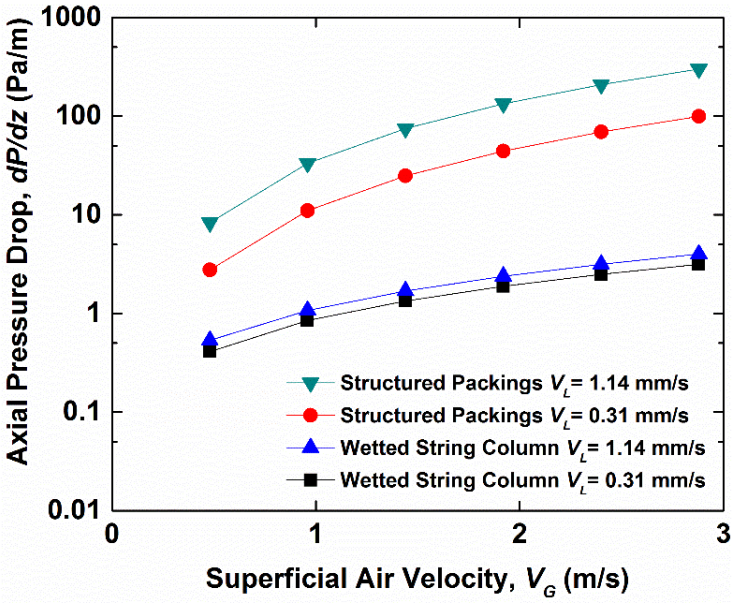

Figure 3.20: The comparison in axial gas phase pressure drop between a wetted string column and a vertical plate structured packing at the same gas-liquid supply conditions

We repeat similar comparison for different values of the pitch p and plate thickness t under the fixed liquid and air superficial velocities. The results, shown in Figure 3.21 and Figure 3.22, are consistent with the earlier results in that the two types of heat exchange systems (the array of wetted strings and the vertical plate structured packing) show comparable heat transfer performance but very different air pressure drops. Both ε and dP/dz decrease as the pitch increases in part because the flow area is larger, and the effective air velocity is lower. At a given pitch, the

systems with thicker plates show slightly higher heat exchanger effectiveness and larger air pressure drop due in part to higher effective air velocities.

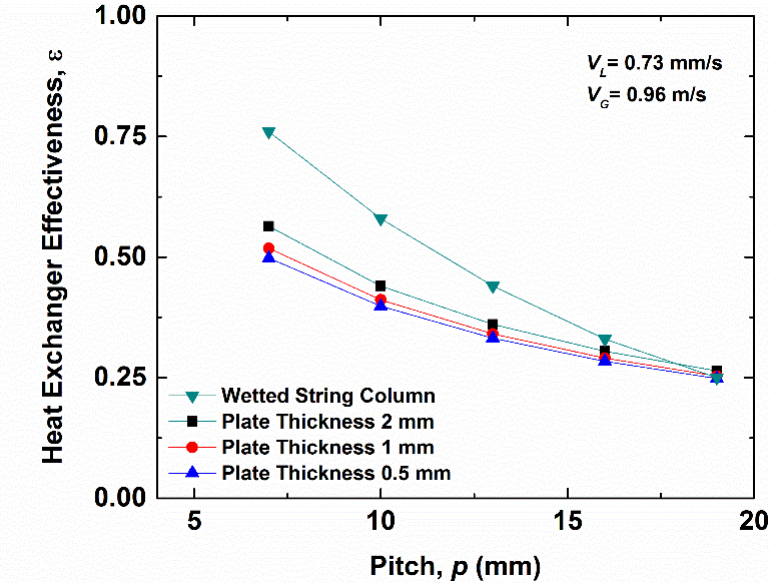

Figure 3.21: The comparison in the heat exchanger effectiveness between the array of wetted strings and the vertical plate structured packing for different pitches and plate thickness.

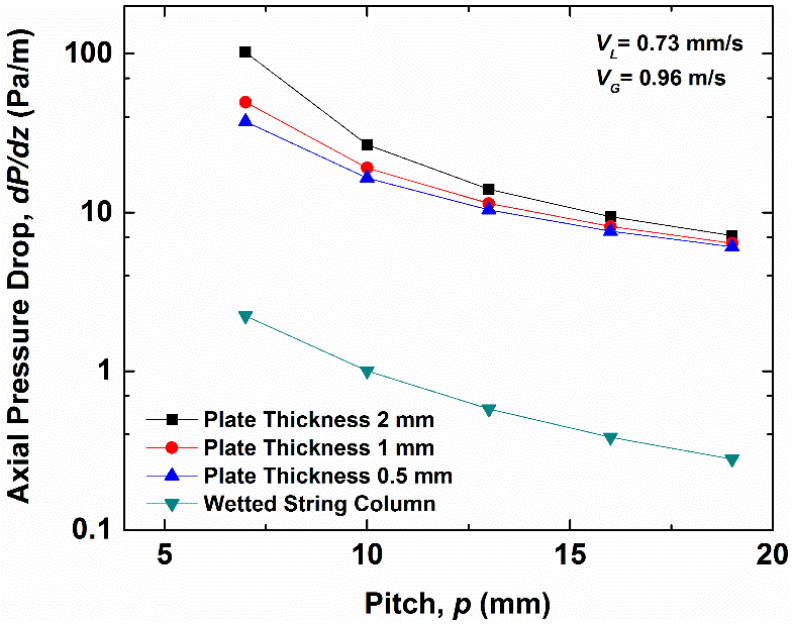

Figure 3.22: The comparison in the pressure drop between the array of wetted strings and the vertical plate structured packing for different pitches and plate thickness.

3.5 Summary

In summary, we experimentally studied the relationship between flow characteristics and overall heat exchanger effectiveness for the thin liquid film flowing down a single string against a counterflowing air stream.

The experimental results demonstrate that the flow characteristics are affected by the liquid mass flow rate, air velocity, and nozzle radius. The increase in air velocity or nozzle radius for a fixed liquid flow rate leads to the increase in liquid beads volume but at a compromise of temporal frequency. Smaller liquid flow rate for a fixed nozzle only lowers the temporal bead frequency. Liquid substrate radius remains nearly unchanged for all cases.

The overall heat exchanger effectiveness is determined experimentally and validated by a numerical simulation. we show that the liquid mass flow rate and the air velocity are two dominant

factors affecting heat transfer effectiveness whereas the details of the flow pattern only affect local bead-to-air heat transfer coefficients. The increase in air velocity or inter-bead spacing results in the increase in local bead-to-air heat transfer coefficient.

We also compare the heat exchanger effectiveness and the gas phase pressure drop between a wetted string column and a structured packing of vertical plates. The wetted string column shows comparable heat exchanger effectiveness but lower gas phase pressure drop than the structured packing.

CHAPTER 4

Thermohydraulic characteristics of a multi-string direct contact heat exchanger

Chapter 3 shows the heat transfer effectiveness of liquid film flowing along a single string against a laminar counterflowing gas stream. This chapter aims to extend the study from one single string to multiple strings. We constructed a 1.6 m-tall prototype heat exchanger with an array of as many as 112 vertically aligned strings. Thin films of a non-evaporating liquid are flown down the strings by gravity and exchange thermal energy with a counterflowing gas stream. We obtained axial liquid temperature profiles and frictional loss in the gas stream for different combinations of liquid and gas flow rates and two different string pitches. Numerical simulation is also performed to help interpret and indirectly validate our experimental results. The overall, gas-side, and liquid-side heat transfer coefficients extracted from the experimentally measured temperature profiles are examined to evaluate the impact of instability in liquid film flows and inter-bead spacing. The applicability of the Reynolds analogy is also assessed using the measured gas-stream pressure drops and air-side heat transfer coefficients.

4.1 Background

Several previous studies investigated liquid films flowing down strings in the Rayleigh Plateau regime for mass transfer applications with counterflowing air velocities below 1 m/s. One such study [35] experimentally investigated the CO_2 absorption by water films. It reported that multi-string mass exchangers achieved higher CO_2 absorption effectiveness than spray columns and

packed beds under nominally the same operating conditions. A later study [5] reported the development and validation of an analytical model for the CO_2 absorption performance [35]. Another study [38] developed a numerical model for CO_2 absorption by water/monoethanolamine liquid films along a single string and performed a parametric study on absorption efficiency. More recent studies reported numerical fluid dynamics simulation of liquid films in the Kapitza instability regime under high counterflowing gas loads [60]. These studies also found the CO_2 absorption effectiveness to be higher for liquid films flowing on strings than liquid films on planar surfaces [68].

Migita et al. [36, 39] constructed a prototype multi-string mass exchanger containing an array of 109 strings to study CO_2 absorption and gas-stream pressure drop. They demonstrated that multi-string mass exchanger has higher absorption effectiveness and lower pressure drop than conventional packed beds. A more recent study [37] investigated hydrazine absorption by a multistring column, and confirmed the advantage of low air side pressure drop.

Relatively few previous studies focused on heat transfer in multi-string exchangers. Hattori et al. [34] presented an approximate analytical model for temperature distribution along a liquid film flowing down a string in the presence of cross-flows of a cooling gas. A modified version of the model in the counterflow configuration was validated in our previous study using a single-string [69]. A later study [7] constructed an experimental setup consisting of a single string and determined the liquid-to-gas overall heat transfer coefficient. The study reported enhanced heat transfer in wavy films in the Rayleigh-Plateau regime, which was ascribed to enhanced internal mixing. However, the study was limited in that it reported the experiments at one fixed gas velocity and that it did not separate the gas-side and air-side thermal resistance. It also did not explore how

convective instability, also referred to as the Kapitza instability, in liquid films flows affects heat transfer.

Although multi-string exchangers can generally be used in applications involving gas-liquid phase changes, such as evaporators and condensers, we will limit ourselves to non-evaporating liquids and non-condensing gases (air) in the present manuscript. We measure axial liquid temperature profiles and gas-stream pressure drop to examine the impact on the thermohydraulic performance of the liquid and air flow rates, instability modes, and string pitch. The applicability of the Reynolds analogy is also examined.

4.2 Experimental

A schematic of the experimental setup used in the present study is shown in Figure 4.1. The setup consists of a vertical acrylic cylinder of diameter 10 cm; a top liquid reservoir; a bottom chamber with flow conditioners to ensure a uniform inlet air stream; and a square array of either 112 polymer strings (7 mm pitch) or 56 strings (10 mm pitch). The polymer strings (R_w = 0.1 mm) are fixed to a metal rod to keep them under tension. The liquid is pumped to the top reservoir, where a cartridge heater with a maximum rating of 2000 W is used to heat the liquid before it exits from the liquid nozzles. After exiting the nozzles, the liquid flows along the strings and is then collected at the bottom. The collected liquid is later recirculated to the top reservoir through a gear pump. Compressed air (inlet pressure ~ 1.3 bar, temperature ~ 20.8 °C) is fed in to the bottom chamber through four plastic tubes with an inner diameter of 3.8 cm. A variable-area flow meter with a range of 6 – 60 SCFM is used to measure the volumetric air flow rate. The superficial air velocity is calculated by dividing the measured volumetric air flow rate by the cross-sectional area of the acrylic cylinder.

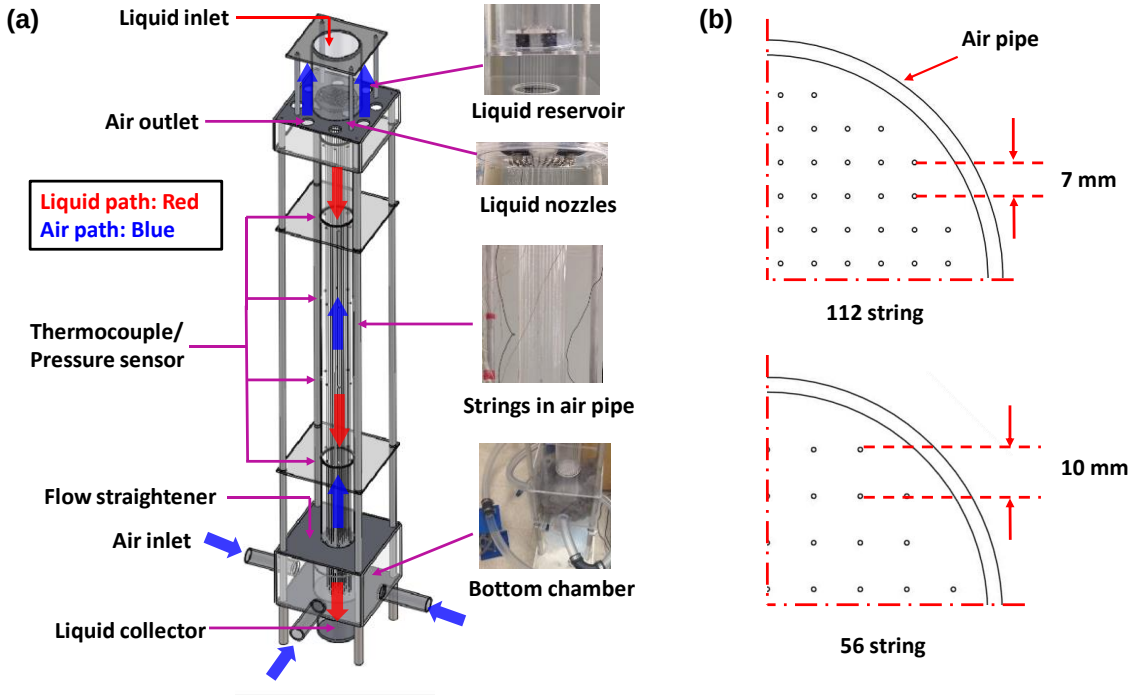

Figure 4.1: (a) Schematic of the experimental setup we used for studying the heat transfer effectiveness and air-side pressure drop of a multi-string heat exchanger. (b) Top views of two arrays with different string pitches.

The liquid nozzles have a diameter of 1 mm and are made of stainless steel. The silicone oil is a well-wetting liquid and tends to rise along the nozzle outer surface, especially during a flow start-up phase where the liquid flow rate is negligible (Figure 4.2a). For our nozzles and working fluid, nozzle lengths greater than 2.5 mm are necessary to prevent the liquid from merging with the top plate and forming an undesired liquid puddle that can impede the liquid flow (Figure 4.2b). The minimum necessary nozzle lengths are generally smaller for liquids with higher viscosities.

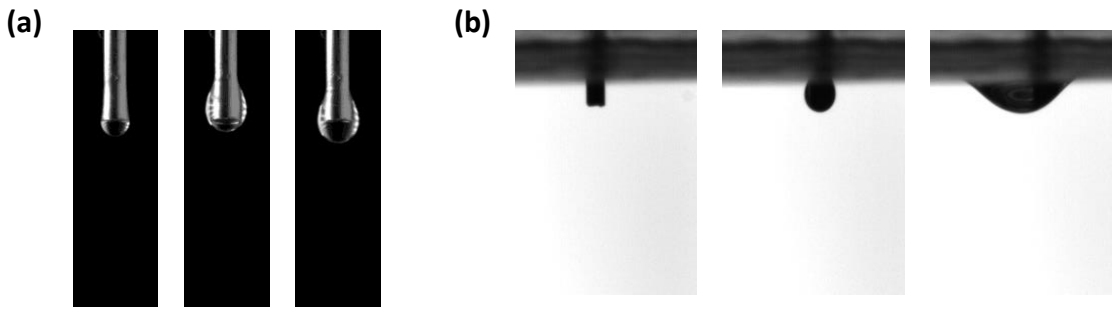

Figure 4.2: (a) Capillary rise of silicone oil along the nozzle outer wall. (b) A liquid puddle formed around the nozzle can impede the liquid flow.

Four groups of 3 micro-thermocouples with tip diameter of 250 μm are placed at three radial locations (i.e. next to 3 different strings) and several axial locations (0.4 m, 0.7 m, 1.0 m, and 1.3 m from the liquid nozzle as indicated in Figure 4.1) to measure the liquid temperatures. We position the micro-thermocouples nominally 0.1 mm away from the strings. The micro-thermocouples are an order of magnitude smaller than liquid beads and they become fully immersed in the liquid as liquid beads flow past them. The thermal response time of the micro-thermocouples ($r^2\rho c_p/3k$ for a sphere immersed in a much larger medium) is estimated to be 0.03 second, which is shorter than the liquid bead transit time over each micro-thermocouple (~ 0.1 second). Although the micro-thermocouple wires slightly drag a portion of a liquid bead off the string, we observe that the liquid bead returns to the string once it passes the micro-thermocouple when the inter-bead spacing is greater than approximately three times the liquid bead length (i.e. $L > 3L_b$, see Figure 4.3). At a smaller inter-bead spacing, the liquid film flow can be disturbed substantially, and two successive beads may merge. In all the experiment reported in the manuscript, the inter-bead spacing is at least four times larger than the bead length. Nevertheless,

we positioned the twelve micro-thermocouples at different strings to avoid any potential complication from upstream micro-thermocouples.

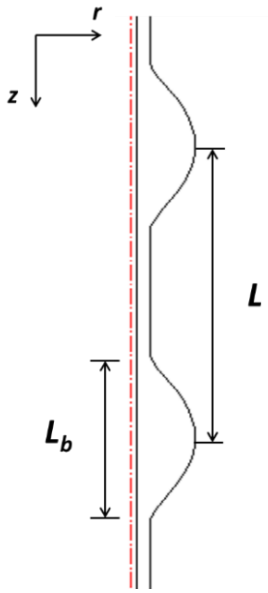

Figure 4.3: The geometric parameters of the travelling beads

A previous study by Nozaki et al. [7] and our numerical simulation study [58] indicated that spatial temperature variations within a liquid bead is less than 2% of the bead mean temperature. At measurement locations, secondary flows generated by interactions with the micro-thermocouples are expected to further enhance mixing and temperature uniformity. Measured fluctuations in micro-thermocouple readings are less than 0.1 °C. We also note that, under the experimental conditions used in the present study, liquid beads account for nearly 95% of the total liquid mass flow. The rest is carried by a thin contiguous liquid substrate flowing down the string. This liquid substrate is periodically entrained by and mixes with liquid beads. Given these, we consider the measured liquid bead temperature as a good approximation of the local bulk mean temperature of the liquid film at the corresponding axial location.

Three thermocouples are also placed inside the top liquid reservoir to monitor liquid inlet temperature. The heater power is adjusted for each run to maintain the liquid temperature inside the top reservoir at 41°C. Outputs from the thermocouples are monitored using a 24-bit high data acquisition system.

Two pressure transducers are placed along axial locations 1 m apart to measure gas-stream pressure drops for each run. The liquid flow rate is measured using a weight scale with a resolution of 0.1 g placed under the liquid collector. The liquid used in our study is low surface tension Rhodorsil v50 silicone oil. Its key properties are: density ρ = 963 kg/m^3, kinematic viscosity ν = 50 mm^2/s, surface tension γ = 20.8 mN/m at 20 °C, thermal conductivity k = 0.15 W/(m·K), and specific heat C_{pL} = 1507 J/(kg K).

For each experimental run, the liquid and air flow rate were first adjusted to respective desire values. The measurements were taken after the readings from all the thermocouples and pressure transducers were stabilized to within 1% over a 15 minutes period. At each liquid and air flow rate combination, experiments were repeated at least three times to confirm reproducibility in temperature and pressure readings to within 5%. Uncertainty in thermocouple readings is estimated to be ± 0.1°C. Radial variations in the liquid temperature, which may be attributed to slight differences in the liquid flow rate among the strings, is estimated to be ± 0.5°C for flows in the Rayleigh-Plateau regime and ± 1°C in the Kapitza instability regime. Uncertainty in the measured pressure drops is estimated to be 0.05 Pa at the air velocity of 0.4 m/s and 0.5 Pa at the air velocity of 4 m/s. Uncertainty in the measured air velocities is estimated to be 0.1 m/s, and uncertainty in the measured liquid flow rates 0.1 g/s.

4.3 Numerical simulation

To help interpret and indirectly validate our experimental results, we constructed a 3D steady-state numerical model to simulate flow and heat transfer characteristics of the multi-string heat exchanger. For each liquid flow rate, we assumed flat liquid films with the same interfacial areas as wavy films observed in the actual experiment. To reduce computational times, we selected a quarter of the one string unit for our simulation, as illustrated in Figure 4.4 (a). Figure 4.4 (b) shows the simulation domain and the corresponding boundary conditions. The adiabatic and no slip condition are applied at the string surface. The zero shear stress and adiabatic condition are applied at all the symmetry surfaces. The coupled-wall condition is applied at the liquid film and air interface to ensure velocity, shear stress, and temperature continuity.

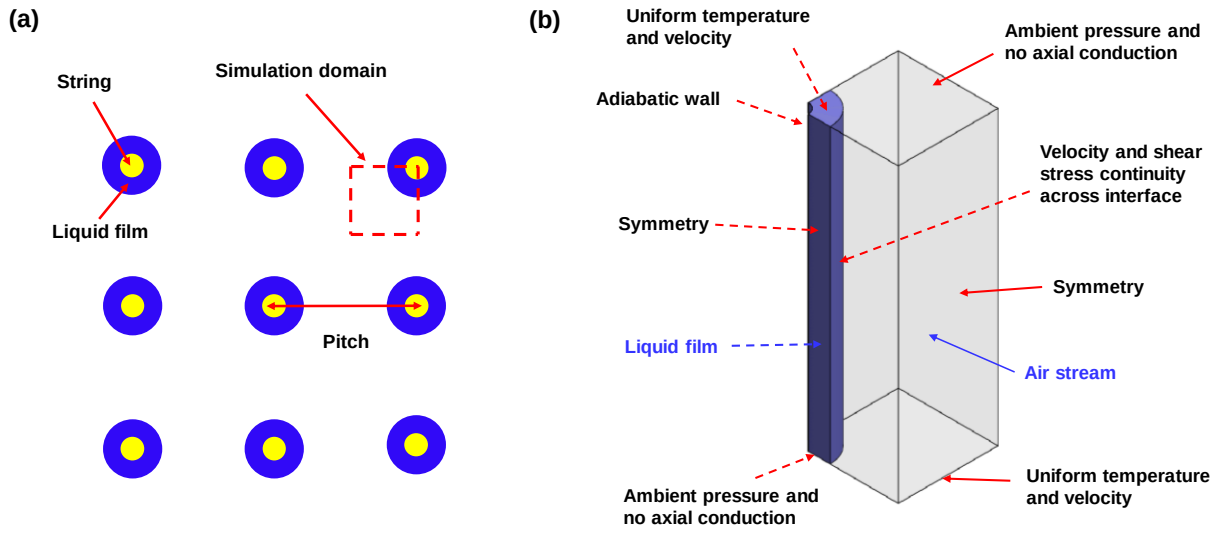

Figure 4.4: Schematic of the simulation domain of the multi-string heat exchanger and the corresponding boundary conditions

A commercial computational fluid dynamics package (ANSYS-Fluent) was used in our simulation. We solved the steady state Navier-Stokes equations and the energy conservation equations to obtain the temperature distributions in both the liquid film and the air stream. Air flows in our experiment are expected to transition to turbulent flow at a Reynolds number of 2300. We used a laminar flow module for the cases with laminar air stream and the transitional shear stress transport (SST) model [70, 71] for the cases with turbulent air flow. For improved accuracy, we use the k-ω model close to the solid surfaces and the k-ε model in the free stream [72].

A multi-zone mesh method was used in the current simulation, which consisted of mainly hexahedral meshes and some tetrahedral meshes. Approximately four million elements used in typical simulation runs. The element size varied gradually from 5 μm in the liquid film to 250 μm in air. At the liquid-gas interface, 25 boundary layers were applied with the first layer thickness smaller than 1 μm to resolve the turbulent viscous sublayer. A mesh-independence study and numerical convergence study were performed to ensure that the predicted liquid film temperatures do not change by more than 2% with further mesh refinements and larger iteration numbers.

4.4 Results and discussion

4.4.1 Axial profiles of the dimensionless temperature

We first analyze the operation of the multi-string heat exchanger under different combinations of the total liquid and air flow rates for its interpretation as a counterflow heat exchanger. To quantify the heat transfer performance of a multi-string heat exchanger, we use a dimensionless liquid temperature [61] defined as:

$$\theta(z) = \frac{T_{\mathrm{L}}(z) - T_{\mathrm{G,in}}}{T_{\mathrm{L,in}} - T_{\mathrm{G,in}}} \tag{4.1}$$

Here, $T_{\mathrm{L}}(z)$ denotes the liquid temperature at a specific axial location z. $T_{\mathrm{L,in}}$, and $T_{\mathrm{G,in}}$ denote the inlet liquid temperature and the inlet gas temperature, respectively.

Figure 4.5(a) shows the dimensionless temperature as a function of the axial location z for a given liquid flow rate but three different air velocities. Figure 4.5(b) shows the dimensionless temperature as a function of the axial location z for a given air velocity but three different liquid flow rates. The dimensionless temperature at the liquid outlet is lower for higher air velocities and lower liquid flow rates, consistent with the general behavior of counterflow heat exchangers.

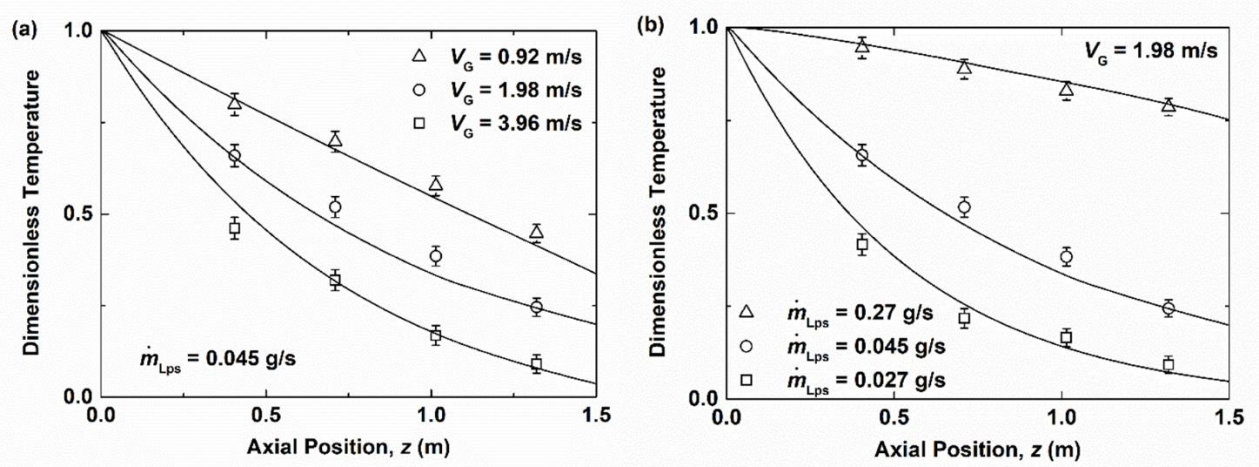

Figure 4.5: (a) Dimensionless liquid temperature as a function of the axial location for a given liquid flow rate under three different air velocities. (b) Dimensionless liquid temperature as a function of the axial location for a given superficial air velocity of 1.98 m/s under three different liquid flow rates. Here $\dot{m}_{\mathrm{Lps}}$ denotes the liquid mass flow rate per string. The symbols represent experimental data and the solid lines the simulation results. All the experimental results shown here are from the square array of 112 strings (7 mm pitch).

Figure 4.6 shows the dimensionless temperature as a function of the axial location for three groups of data. Each group consists of a data set obtained from the 7 mm-pitch array (112 strings in total) and a data set obtained using a 10 mm-pitch array (56 strings in total). In all cases, the liquid flow rate per string are fixed at 0.045 g/s. When the air flow rates are adjusted to keep the heat capacity rate ratio C_r constant, the dimensionless temperatures from the two string arrays remain within 5% of each other. This suggests that the overall heat transfer coefficient does not depend sensitively on the string pitch and hence the hydraulic diameter for the present two cases. The lines represent the numerical simulation results, which agree well with our experimental data. The experimentally measured temperature profiles shown here are further analyzed to extract the heat transfer coefficients in Section 4.4.2.

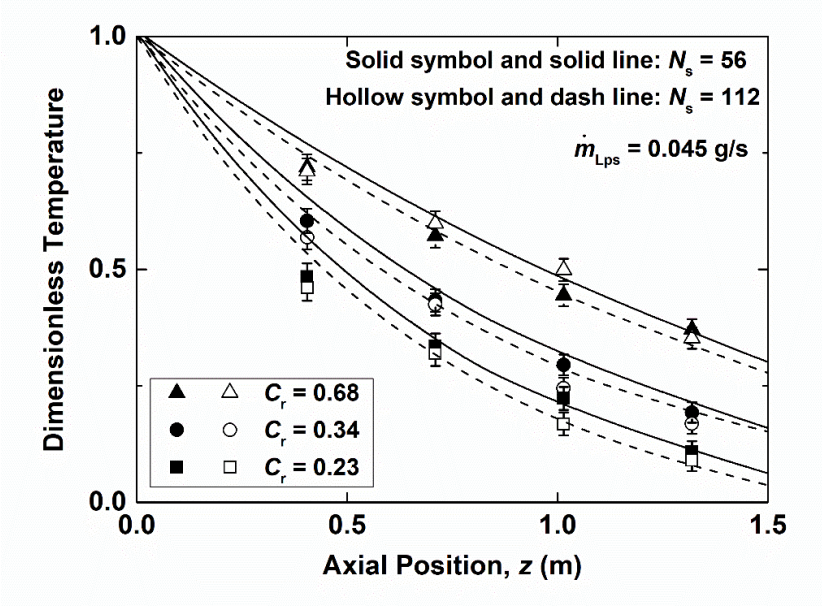

Figure 4.6: Dimensionless liquid temperature as a function of the axial location. The symbols correspond to the experimental data. The solid lines represent the simulation results for the array of strings with 10 mm pitch and the dash lines the simulation results for the array of strings with 7

mm pitch. $\dot{m}_{Lps}$ denotes the liquid flow rate per string, which is fixed, and N_s the total number of strings. For all the data shown in Figure 4.6, the smaller of the heat capacity rates, C_{min}, is that of the liquid.

We next consider cases where we vary the liquid flow rate per string while adjusting the air velocity to keep the heat capacity rate ratio constant. Figure 4.7 shows the dimensionless temperature as a function of the axial location for three different liquid flow rates per string under a fixed heat capacity rate ratio. The liquid film with a liquid flow rate of 0.045 g/s is in the Rayleigh-Plateau regime whereas the liquid films with the two higher liquid flow rates exhibit the Kapitza instability regime. All three sets of data shown in Figure 4.7 are obtained using the square string array of 7 mm pitch (112 strings in total).

The dimensionless temperatures deviate from each other as we move down the strings, with the highest flow rate case showing almost 20% higher dimensionless temperature than the lowest flow rate case near the liquid outlet. This is attributed to transition from the Rayleigh-Plateau regime to the Kapitza instability regime. Although the instability transition enhances heat transfer coefficient (as discussed in Sec 4.4.2), the reduced surface area to volume ratios and shorter liquid residence times on the string lead to a higher dimensionless temperature.

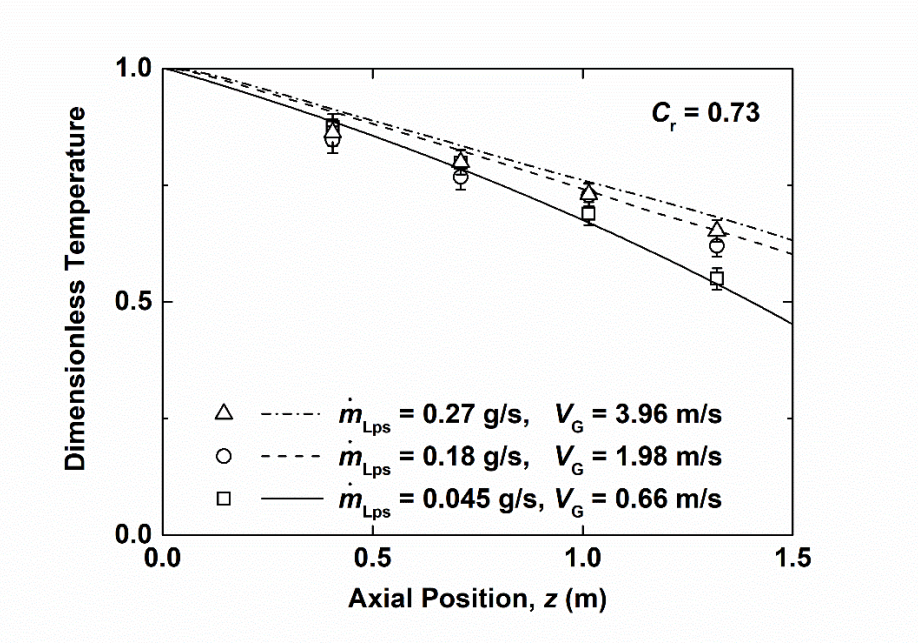

Figure 4.7: Dimensionless liquid temperature as a function of the axial location for three different liquid flow rates per string. The symbols represent the experimental data and the lines represent the numerical simulation result. The three cases share the same The three cases share the same heat capacity rate ratio. The smaller of the two heat capacity rates, C_{min}, is that of air for the cases shown.

4.4.2 Heat transfer coefficients

To further elucidate the impact of the liquid film thickness and morphology, hence the instability regime, on heat transfer, we analyze the axial temperature profiles to extract the overall heat transfer coefficients. Under the assumptions of the constant overall heat transfer coefficient and no axial conduction, the energy conservation equations [54] can be written as

$$\dot{m}_{\mathrm{L}}\, \mathrm{C}_{\mathrm{p,L}}\, dT_L = U\, dA\, \Delta T_{\mathrm{local}} \tag{4.2}$$

$$\dot{m}_{\mathrm{L}}\, \mathrm{C}_{\mathrm{p,L}}\, dT_{\mathrm{L}} = \dot{m}_{\mathrm{A}}\, \mathrm{C}_{\mathrm{p,A}}\, dT_{\mathrm{A}} \tag{4.3}$$

Here $\dot{m}_{\mathrm{L}}$, T_{L}, $C_{\mathrm{P,L}}$, denote the flow rate, temperature, and specific heat of the liquid, respectively. Likewise, the parameters $\dot{m}_{\mathrm{A}}$, T_{A}, and $C_{\mathrm{P,A}}$ denote the corresponding quantities for air. U represents the overall heat transfer coefficient and $\Delta T_{\mathrm{local}}$ represents the local temperature difference between the liquid film and the air stream. We iteratively solved these two equations numerically using U as an adjustable parameter until the liquid film temperature matched the experimental data. The quality of the fits is comparable to that of the numerical simulation results shown in Figure 4.6 and Figure 4.7.

The gas side heat transfer coefficient in general depends non-linearly on the air velocity. Figure 4.8 shows the reciprocal of overall heat transfer coefficients as a function of $1/V_{\mathrm{G}}^{\mathrm{m}}$ where V_{G} is the superficial air velocity. We use a previously reported value of 0.8 for the exponent m in turbulent flows [63]. Following a previous study [73], we consider the y-intercept, corresponding to the infinite air velocity, of the linear fit to each data set as a measure of the liquid-side heat transfer coefficient (or its reciprocal, to be precise). For the liquid films flowing in the Rayleigh-Plateau regime shown in Figure 4.8(a), the estimated liquid-side heat transfer coefficients are 37 – 55 W/(m^2 K). The string array pitch (7 or 10 mm) has a negligible effect on the liquid side heat transfer coefficient.

The estimated liquid-side heat transfer coefficients values are comparable to the conduction resistance of approximately 30 W/(m^2 K) across liquid spheres of the same equivalent radii as travelling liquid beads. The actual liquid-side heat transfer coefficient would be higher than this value because internal circulation within each bead enhances heat transfer [34]. Note that, for a

fixed nozzle diameter, liquid films flowing in the Rayleigh-Plateau regime at different flow rates produce liquid beads of approximately the same radii but different inter-bead spacings [69, 74].

We note that the cases with a liquid flow rate per string of 0.027 g/s show larger overall heat transfer coefficients than the case with a higher liquid flow rate per string of 0.045 g/s. This results from the smaller spacing between two successive liquid beads at the higher flow rate. As discussed in [69], at a smaller inter-bead spacing, downstream liquid beads are strongly affected by wakes (i.e., recirculation zones in the gas stream) formed behind upstream liquid beads [56, 62]. The convective heat transfer in the gas phase is therefore degraded.

At air velocities smaller than 1.2 m/s, the overall heat transfer coefficient of the heat exchanger with 10 mm string pitch (56 strings) is larger than that with 7 mm pitch (112 strings). This rather surprising result arises because transition to turbulence occurs at lower air velocities for the heat exchanger with the larger string pitch, which has an approximately 1.5 times larger hydraulic diameter than the heat exchanger with the smaller string pitch. At higher air velocities, when the air flows are turbulent in both heat exchangers, the overall heat transfer coefficients are comparable and nearly within their estimated uncertainties.

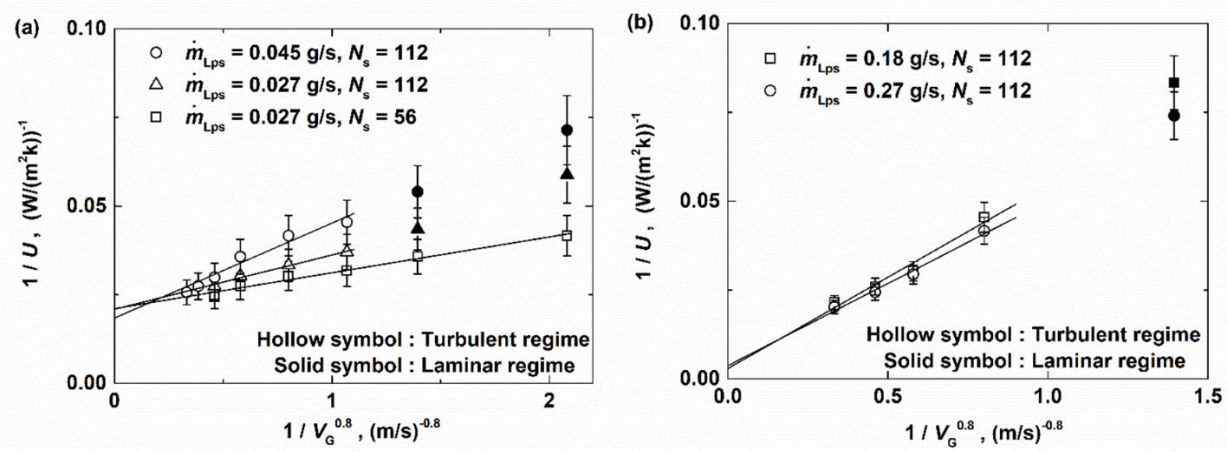

Figure 4.8: The reciprocal of the overall heat transfer coefficient as a function of the reciprocal of the superficial air velocity. Part (a) shows the cases of liquid films flowing in the Rayleigh-Plateau regime whereas Part (b) shows the cases of liquid films flowing in the Kapitza instability regime.

Figure 4.8(b) shows the overall heat transfer coefficient of the liquid films flowing in the Kapitza instability regime as a function of the reciprocal of the air velocity. Following a similar approach as Figure 4.8(a), we estimate the liquid-side heat transfer coefficients from the *y*-intercepts. The estimated liquid-side heat transfer coefficients range 100 - 400 W/(m^{2}K), up to an order of magnitude higher than those for the liquid films flowing in the Rayleigh Plateau regime. This enhanced heat transfer in the liquid can be attributed to coalescence of liquid beads traveling at different speeds in the Kapitza instability regime, as shown in Figure 4.9.

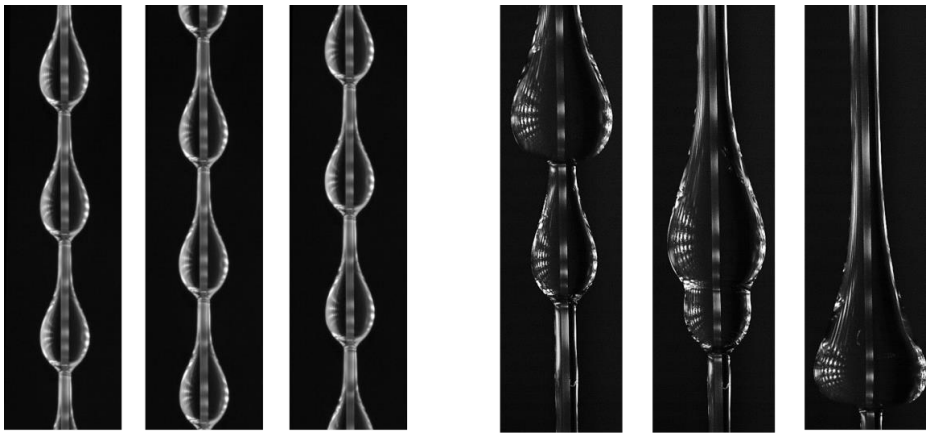

Figure 4.9: Comparison between liquid films flowing (a) in the Rayleigh-Plateau regime and (b) in the Kapitza instability regime. The liquid bead coalescence only happens in the latter regime

4.4.3 Air-side pressure drop

Gas-stream pressure drop is another important characteristic of heat or mass exchangers. Figure 4.10 shows our experimental data we obtain using the two string arrays of different pitches as a function of the air velocity. We compare the measured pressure drops with predictions from existing empirical correlations for longitudinal flows along rod bundles [75–78].

For laminar flows along an infinite extension of rod bundles, we adapt the reported correlation [75] for our multi-scale heat exchangers as

$$Re = \frac{\rho u D_{\mathrm{h}}}{\mu} \tag{4.4}$$

$$\sigma = 1 - \frac{\pi}{4\left(\frac{s}{D_N}\right)^2} \tag{4.5}$$

$$f_L\, Re\, \left(\frac{D_N}{D_{\mathrm{h}}}\right) = \frac{8\sigma^2}{2(1-\sigma) - \ln(1-\sigma) - 0.5(1-\sigma)^2 - 1.5} \tag{4.6}$$

$$\frac{\Delta P}{\Delta z} = \frac{2 f_L \rho u^2}{D_{\mathrm{h}}} \tag{4.7}$$

Here, *Re* represents the gas stream Reynolds number based on the hydraulic diameter. D_h and D_N represent the hydraulic diameter and the average liquid film diameter calculated from Nusselt solution, respectively [29]. The parameter *s* denotes the center-to-center distance between two adjacent strings, *u* the air velocity, and f_L the friction factor in the laminar flow regime.

The gas flows in our multi-string exchangers are considered to undergo transition to turbulence at a Reynolds number of 2300. The air streams for the 10 mm-pitch string array are expected to be in the turbulent regime for all the experimental conditions reported here. For the 7 mm-pitch string array, the cases where the air flows are in the laminar flow regime are indicated in Figure 4.10 using the solid symbols.

For turbulent flows along an infinite extension of rod bundles, the correlation reported in [76–78] for our multi-string heat exchangers is

$$x = \sqrt{\frac{4}{\pi}}\,\frac{s}{D_N} \tag{4.8}$$

$$\sqrt{\frac{8}{f_T}} = 2.5\ln\left(Re\sqrt{\frac{f_T}{8}}\right) + 5.5 - \frac{3.966+1.25x}{1+x} - 2.5\ln(2+2x) \tag{4.9}$$

$$\frac{\Delta P}{\Delta z} = \frac{f_T \rho u^2}{2D_h} \tag{4.10}$$

Here *x* denotes the geometric factor and f_T the friction factor in the turbulent regime

Figure 4.10 shows that the gas-stream pressure drop increases approximately linearly with increasing air velocities in the laminar flow regime. When the air flow reaches the turbulent regime, the pressure drop increases approximately quadratically with increasing air velocities.

Figure 4.10 also shows that, at a fixed array pitch and an air velocity, a larger liquid flow rate per string leads to a higher gas-phase pressure drop. Larger liquid flow rates per string lead to thicker liquid films, which not only reduce the cross-sectional area for gas flows but also increases the liquid-air interface areas. At a given liquid flow rate per string, the array with the larger string pitch has a lower pressure drop.

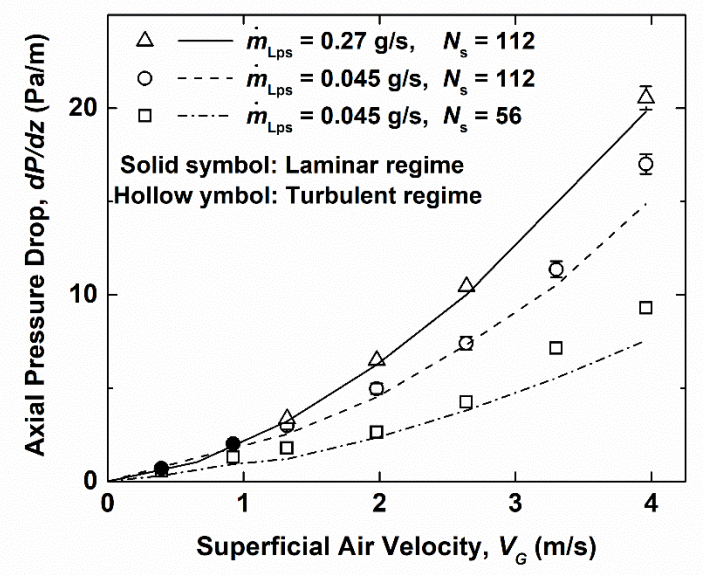

Figure 4.10: Experimentally measured air-stream pressure drop (symbols) and the prediction from the empirical correlations (lines).

As shown in Figure 4.10, the experimental data and the predictions from the empirical models for rod bundles match each other within 10%. The reasonably good agreement between the experimental data and the prediction does suggest relatively low form drag at superficial air

velocities (< 3 m/s) used in the present study. In our experiments, the inter-bead spacing is at least four times larger than the bead length as discussed in Sec 4.2. Under this condition, our numerical simulation [69] indicates that the skin friction dominates over the form drag as the flow separation angle (measured from the forward stagnation point) is large and the recirculation zone is narrow (Figure 4.11a). For an example case (liquid flow rate per string = 0.045 g/s, superficial gas velocity = 1.32 m/s), the form drag is predicted to account for approximately 20% of the pressure drop. This is somewhat counteracted by the fact that the assumed smooth cylindrical rods have larger interfacial areas than the actual liquid films with discrete liquid beads, leading to approximately 10% "over"-prediction of the skin friction. These are consistent with the fact that the empirical model does underpredict the measured pressure drops by approximately 10%.

The situation is different at higher air velocities (larger than approximately 3 m/s) for liquid films flowing in the Rayleigh-Plateau regime. This may be attributed to finite bead deformation caused by aerodynamic drag as illustrated in Figure 4.11(b). This leads to much larger form drag. Indeed, the measured pressure drops are almost 20% larger than the model predictions. For liquid films flowing in the Kapitza instability regime, the liquid bead deformation is observed to be less pronounced, which may be due to their larger inertia and flatter profiles as illustrated in Figure 4.11(c). The model prediction agrees better with the measured data in the Kapitza instability regime.

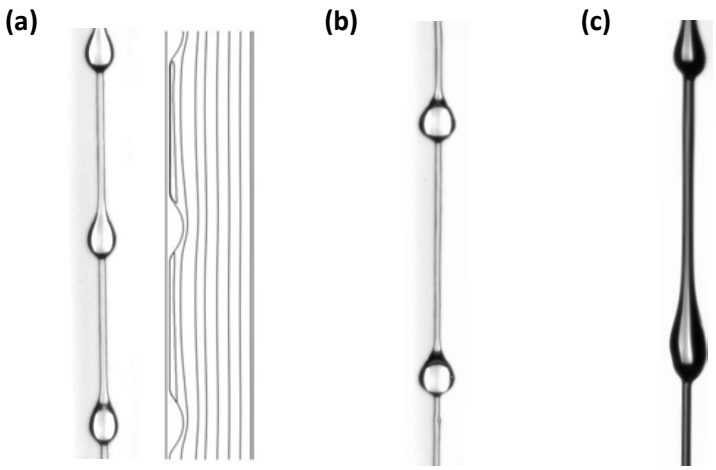

Figure 4.11: (a) Predicted streamlines for a liquid film flowing in the Rayleigh-Plateau regime at a large inter-bead spacing and a low (< 3 m/s) gas velocity (b) Deformed liquid beads at a higher (> 3 m/s) gas velocity. (c) A typical liquid film profile with Kapitza instability

4.4.4 Air-side heat transfer coefficient and Reynolds analogy

Using the liquid side heat transfer coefficients we estimated in Sec. 4.4.2, we next calculate the corresponding air-side heat transfer coefficient from

$$\frac{1}{h_{\mathrm{air}}} = \frac{1}{U} - \frac{1}{h_{\mathrm{L}}} \tag{4.11}$$

Here h_{air}, U, and h_{L} are the air-side heat transfer coefficient, overall heat transfer coefficient, and liquid-side heat transfer coefficient, respectively. The calculated air-side heat transfer coefficients have very large uncertainty at high air velocities when the overall heat transfer coefficient is very close to the liquid side heat transfer coefficient. We therefore perform this calculation for air velocities below 1.98 m/s when the liquid flow rate per string is lower than 0.05 g/s.

As shown in Figure 4.12, the air-side heat transfer coefficients thus calculated are consistent with the modified Reynold analogy, $C_f/2 = j_H$ [79, 80]. Here, j_H is the Colburn j factor and C_f is the Fanning friction factor [54]:

The apparent applicability of the Reynolds analogy may be attributed to relatively small contribution from the form drag afforded by liquid beads under the experimental conditions used in the present study as discussed in Sec. 4.4.3.

$$j_H = StPr^{\frac{2}{3}} \tag{4.12}$$

$$St = \frac{h_{\text{air}}}{\rho_G C_{PG} V_G} \tag{4.13}$$

$$C_f = \frac{\Delta P\, A_c}{A(\frac{1}{2}\rho_G {V_G}^2)} \tag{4.14}$$

In the above, St is the Stanton number, Pr is the Prandtl number of air, A_c denotes the cross-sectional area of the gas stream, A denotes the total liquid-air interfacial area, and ΔP is the gas-stream pressure drop.

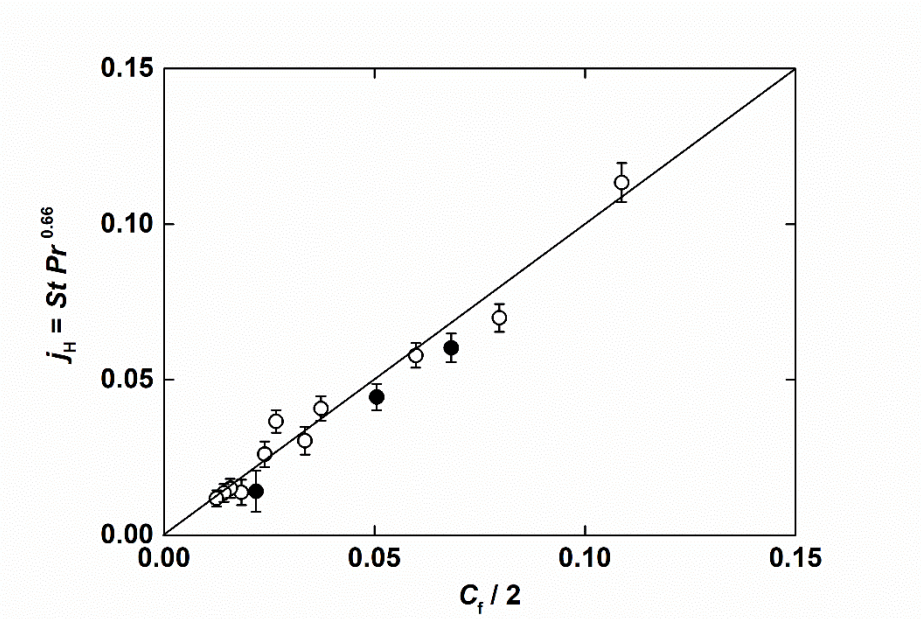

Figure 4.12: Relationship between the Colburn j factor and the Fanning friction factor from our experiments. The solid line is a line of slope unity. The hollowed symbols are for air flows projected to be in the turbulent regime and the solid symbols in the laminar regime

4.4.5 Comparison of heat exchanger performance with parallel-plate structured packing

Liquid films flowing down the surfaces of vertical plates or tubes are widely used for heat and mass transfer applications. Directly comparing these heat or mass exchange configurations is difficult because one must account for system-level constraints, including the cross-sectional area/volume and the superficial liquid and air velocities. As a limited comparison, we consider two direct contact heat exchangers of the same size under the nominally identical working condition. One consists a square array of strings with 7 mm pitch (our system), and the other consists of a well vertically aligned parallel-plate structured packing [63]. The thickness of the plates is set to be 1 mm. The two systems have the same overall dimension (1 m wide, 1 m long and 1.6 m tall). We also keep the superficial liquid velocity $V_L = \dot{m}_L/(\rho_L A_f)$, and air velocity $V_G = \dot{m}_G/(\rho_G A_f)$ the

same. Here, $\dot{m}_L$ and $\dot{m}_G$ denote the total inlet liquid and air mass flow rate, respectively. ρ_L and ρ_G denote the liquid and air density, respectively. A_f is the column cross-sectional area (1 m^2).

We use our experimental data for both the outlet temperature and gas phase pressure drop of the multistring heat exchanger. The outlet temperature and gas phase pressure drop of the parallel structured packing are evaluated using empirical correlations [3, 65–67]. The equations for evaluating the liquid side heat transfer coefficient is indicated in Sec 3.4.6. Since the air flow in this comparison is the turbulent flow ($Re_G > 2300$). We use the following correlation to calculate the frictional factor and the air side heat transfer coefficient [54]:

$$f_p = (0.79\ln(Re_G) - 1.64)^{-2} \tag{4.15}$$

$$Nu_G = \frac{h_G D_h}{k_G} = \frac{(\frac{f_p}{8})(Re_G - 1000)Pr_G}{1+12.7\left(\frac{f_p}{8}\right)^{\frac{1}{2}}(Pr_G{}^{\frac{2}{3}}-1)} \tag{4.16}$$

Here f_p is the friction factor for and Re_G denotes the gas side Reynolds number. Pr_G is the Prandtl number for gas. D_h is the hydraulic diameter of the structured packings, and k_G is the thermal conductivity of air.

For each combination of the superficial liquid and air velocities, we adjust the distance between two parallel plates of the structured packing to yield the same outlet temperature as the multistring column. We considered 2 mm plate thickness of a structured packing as in practical applications [63]. The corresponding gas phase pressure drop are then compared between two systems and shown in Figure 4.13. Two superficial liquid velocities were selected for a comprehensive comparison. The superficial liquid velocity of 4.5 mm/s represents an industrial level liquid flow rate. Figure 4.13 indicates that the wetted string column shows approximately 1.5 times lower

pressure drop than the parallel plate structured packing for the same heat transfer performance, consistent with the conclusions from the previous experimental studies on multistring mass exchangers [36]. Figure 4.13 also show that the air-side pressure drop of a multistring heat exchanger is less sensitive to the liquid superficial velocity than a structured packing. This is due to larger variation of the available air path cross-sectional area in structured packings.

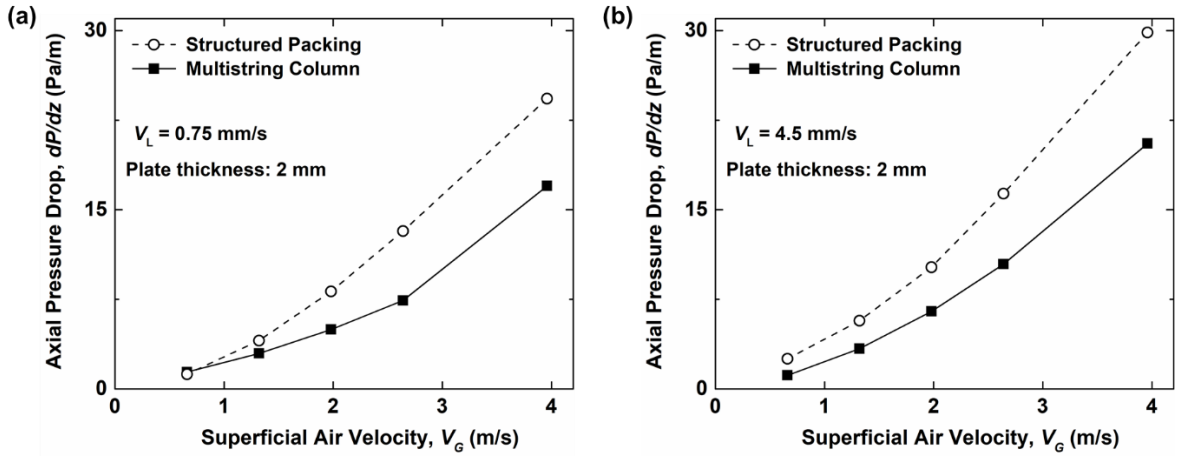

Figure 4.13: A comparison of measured air-side pressure drop between a string column and a vertically aligned parallel plate structured packing. Circles represent structured packing and squares represent multistring column used in our study.

4.5 Summary

We experimentally investigated the influence of liquid flow rate, gas velocity and string pitch on the heat transfer performance and frictional loss of a multi-string heat exchanger. By analyzing the axial liquid temperature profiles, we extract the overall, liquid-side, and air side heat transfer coefficients under different combinations of air and liquid flow rates. The liquid films flowing in the Kapitza instability regime are found to have significantly smaller liquid-side thermal resistance

than the liquid films flowing in the Rayleigh-Plateau regime. Merging of liquid beads traveling down the strings in the Kapitza instability regime is very effective in enhancing liquid-side thermal resistance. The overall heat transfer coefficient does not vary significantly between the two string pitches we examined (7 mm and 10 mm). For liquid films flowing in the Rayleigh-Plateau regime, the gas-side heat transfer coefficient is lower at higher liquid flow rates due to the increased interference of wake regions (of air) between successive liquid beads. The measured gas-stream pressure drop agrees reasonably well with the prediction from existing correlations for bundles of parallel solid tubes. The applicability of the Reynolds analogy for the gas streams has been observed under the present experimental conditions, which is consistent with a relatively small contribution of form drag afforded by the wavy liquid films. The present work helps improve our understanding of the heat transfer performance and frictional loss in a multi-string heat exchanger.

CHAPTER 5

A highly effective multi-string humidifier with a low gas stream pressure drop for desalination

The previous chapter discussed investigating the multi-string heat exchanger. This chapter aims to extend the transfer process from only heat transfer to simultaneously heat and mass transfer. In this chapter we report a new design of compact light-weight humidifiers with high effectiveness and low electric energy consumption for HDH systems. The new design consists of a dense array of vertically aligned strings, along which thin films of a heated liquid feed are allowed to flow under gravity. A counterflowing gas stream makes direct contact with liquid films carrying the generated water vapor to a dehumidifier. The unique geometric configuration of our design affords high interface-to-volume ratios necessary for high heat/mass exchange effectiveness and straight contiguous gas flow paths for reduced gas-phase pressure drops. We constructed a 0.4 m-tall prototype and examined the effects of the liquid flow rate, air velocity and feed liquid salinity on the heat/mass transfer performance and the gas stream axial pressure drop. Compared with previously reported pad humidifiers and spray columns, the present multi-string humidifier achieves almost 5 times the evaporation rate per humidifier volume at comparable gas stream pressure drops or an order of magnitude reduction in the gas stream pressure drop at comparable total evaporate rates. Our work demonstrates a highly-effective but compact and light-weight

multi-string humidifier with a small gas stream axial pressure drop for HDH and related applications.

5.1 Background

Understanding the influence of various operating parameters (e.g., flow rates, inlet temperatures, and salinity) on the humidification process contributes significantly to the optimization of HDH systems. For example, a previous study [81] experimentally examined a pad humidifier and a tubular spray humidifier to determine how the seawater/air flow rate, seawater temperature and equipment dimension affect the evaporation rate. Another previous study [82] conducted a combined experimental and theoretical investigation of a pad humidifier used in a multi-stage solar desalination unit. A multi-stage humidifier [83] was also reported to maximize the humidity ratio at the humidifier exit for increased fresh water production. There was also a study [84] where an experimental and modelling study was conducted to determine the mass transfer coefficient of both natural and forced convection in a vertical channel with parallel plates, which emulate structured-packing humidifiers. A related study [85] investigated how the salinity affects water evaporation rates and integrated the salinity into their empirical correlations for the flat plate humidifier.

With a growing concern over the global climate change, many previous studies explore the use of renewable energy sources, such as solar energy or geothermal energy, for powering HDH. One such study [86] constructed a thermodynamics model for a solar powered desalination unit and predicted that the water productivity in summer is twice larger than winter based on the solar radiation intensity data from Xi'an, China. A later study [87] constructed a large-scale pilot system with a 100 m^2 solar air heater field and demonstrated 1200 L/day fresh water production at an

average solar radiation intensity of 550 W/m^2. Past studies [88] also successfully demonstrated utilization of geothermal energy for heat input.

Thermodynamically balancing the humidification and dehumidification processes in HDH systems helps effectively reduce overall entropy production and thereby improve the overall thermal efficiency of HDH processes [89, 90]. A parameter often used to quantify the performance of HDH systems is the gain output ratio (GOR), defined as the ratio between the latent heat of evaporation and the net thermal energy input. Previous studies performed thermodynamic optimization analyses to explore ways to improve the GOR of HDH systems [91–93].

Past studies [94], for example, aimed to optimize extractions and subsequent injections of a humidified gas between a humidifier and a dehumidifier and experimentally demonstrated that a single extraction-injection step could improve GOR from 2.6 to 4 using a commercial packed bed humidifier and a shell-and-tube exchanger dehumidifier. Theoretical analyses, indeed, projected that GOR values greater than 10 are possible by integrating multiple extraction/injection steps. Such high values of GOR, however, were achievable only for humidifiers and dehumidifiers with correspondingly high heat/mass exchange effectiveness. In other words, a critical challenge is often not whether one can achieve high GOR values using a given humidifier or dehumidifier design concept. A bigger challenge arises from the fact that existing design concepts would require very large and/or heavy units with high capital and installation costs or compact units with very high pressure drops and hence high operating costs.

A previous study using a non-volatile liquid as a working fluid demonstrated that a direct-contact heat exchanger of the same geometric design can deliver the same heat transfer effectiveness at a much lower pressure drop than traditional parallel-plate structured packings [69,

95]. Earlier studies of multi-string exchangers also suggested their applications in CO_2 absorption and hydrazine vapor separation [36, 37, 39].

In the present work, we report a combined experimental characterization and modeling study to validate our humidifier design, specifically with desalination applications in mind. The effects of the liquid flow rate, air velocity, and liquid salinity on the heat and mass transfer rates are experimentally characterized. The mass transfer conductance-interfacial area products obtained are next used to quantify the performance of a multi-string humidifier. The gas-stream pressure drop of the multi-string humidifier is also measured and compared with existing humidifier designs.

5.2 Experimental

A schematic of the experimental setup used in the present study is shown in Figure 5.1. The setup consists of a vertical acrylic cylindrical pipe of an inner diameter 6.35 cm for air flow; a top liquid reservoir; a bottom chamber with flow conditioners to ensure a uniform inlet air stream; and a square array of 24 cotton strings (R_w = 0.375 mm). The top view of the string array is shown in Figure 5.2. The string pitch used in the current study is 10 mm. All the strings are fixed to a metal rod to keep them under tension.

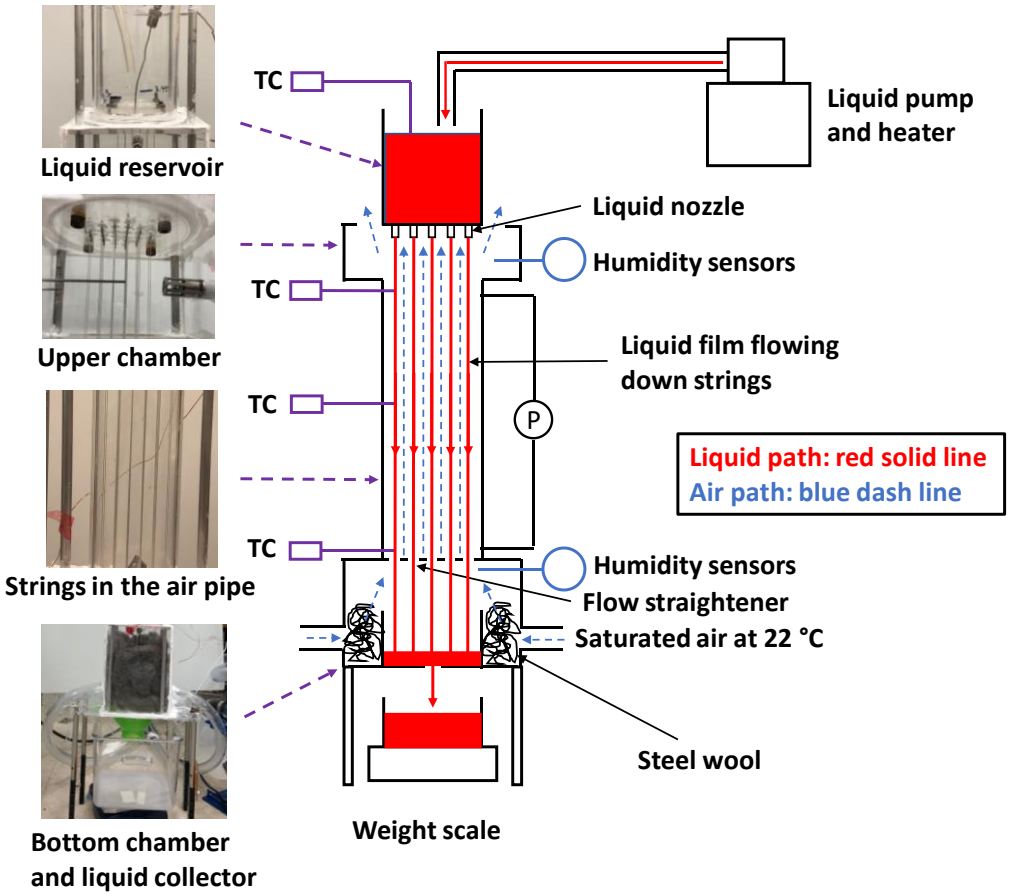

Figure 5.1: Schematic of the experimental setup used to characterize the heat/mass transfer and air-stream pressure drop in the multi-string humidifier

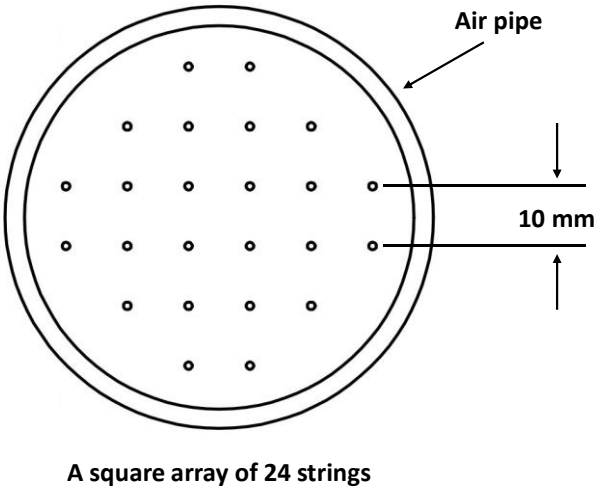

Figure 5.2: Top view of a square array of 24 strings. The string pitch used for the experimental results reported in the article is 10 mm.

A bath circulator is used to heat the feed water and pump it into the top reservoir. The heated liquid is divided into multiple streams using an array of nozzles built into the top reservoir. As the liquid streams flow down the strings under gravity, they form traveling liquid beads due to intrinsic instability caused by interplay among surface tension, viscous, gravity, and inertia forces [74]. The liquid is then collected in a bottom reservoir, whose weight is monitored using a weight scale to determine the liquid flow rate. A converging cone is used to facilitate the collection of the liquid. A stream of air, saturated with water at 22 °C (relative humidity = 100%), is introduced into the bottom of the main section to mimic a closed-air open-water HDH cycle. A steel wool is used to homogenize the air flow. A flow straightener is placed at the inlet of the test section to ensure a uniform inlet air stream. The gas flow rate is measured using a variable-area flow meter with a range of 0.8 - 8 SCFM.

The spatial temperature distributions of the liquid film and the air stream are measured using micro-thermocouples with a tip diameter of 250 μm. Three pairs of micro-thermocouples are

placed at three axial locations (0.1 m, 0.25 m, and 0.4 m) from the liquid nozzle, each at one of two different radial locations (i.e. next to 2 different strings), as shown in Figure 5.1 to measure local liquid temperatures. We place the micro-thermocouples nominally 0.1 mm away from dry strings such that the micro-thermocouples are fully immersed in liquid films without actually touching the string. One thermocouple is placed inside the top liquid reservoir to monitor the liquid inlet temperature.

To measure the air stream temperatures, we place six additional micro-thermocouples at three axial locations (0 m, 0.25 m, and 0.4 m), one group along the test section center and the other group near the test section boundary. Two humidity sensors are used to monitor the gas stream humidity at the air inlet and the air outlet. Pressure transducers are installed at two axial locations 0.3 m apart to measure the gas-stream pressure drops. Feed water streams at three different salinity levels are examined in the present study. They are the distilled water, the water with a salinity of 35 g/kg, and the water with a salinity of 108 g/kg, respectively. For each experimental run, the liquid and air flow rates are first adjusted to their respective set values. The measurements are taken after readings from all the thermocouples and pressure transducers are stabilized to within 1% over a 15-minute period. Each experimental run lasted for two minutes. A sampling frequency of 50 Hz is used for the thermocouples. At each liquid and air flow rate combination, experiments are repeated at least three times to confirm that the data are reproducible to within 5%. The liquid flow rates examined in the current study range from 0.7 to 3.6 g/s. The volumetric flow rates of the air stream vary from 1 to 6 SCFM.

Estimated uncertainty in thermocouple readings is ± 0.1 °C. Radial variations in the liquid temperature across the test section, which may be attributed to slight differences in the liquid flow rate among the strings, is estimated to be ± 2 °C. Radial variation in the air temperature at a given

axial location is estimated to be ± 1 °C. Uncertainty in the measured air velocities is estimated to be 0.05 m/s, uncertainty in the measured liquid flow rates 0.1 g/s, uncertainty in the measured pressure drops 0.05 Pa, and uncertainty in the relative humidity values 2%.

5.3 Theoretical analysis

To help interpret the experimental data, we construct a steady-state model based on the mass and energy balance following a previous study [3]:

$$\frac{d\dot{m}_{\mathrm{L}}}{dA_z} = \frac{d\dot{m}_{\mathrm{G}}}{dA_z} \tag{5.1}$$

$$\frac{d}{dA_z}(\dot{m}_{\mathrm{L}} h_{\mathrm{L}}) = \frac{d}{dA_z}(\dot{m}_{\mathrm{G}} h_{\mathrm{G}}) \tag{5.2}$$

Here $\dot{m}_{\mathrm{L}}$ and h_L denote the mass flow rate and enthalpy of the liquid, respectively. The symbols $\dot{m}_{\mathrm{G}}$ and h_G denote the mass flow rate and enthalpy of the air. The cumulative liquid-gas interfacial area, which increases linearly from the liquid nozzle as we move downstream, is labeled A_z.

High rates of evaporation can lead to a non-negligible normal velocity component of water vapor near the surface of water (Figure 5.3). This so-called convective component is suggested to be significant [3] when the water temperature exceeds approximately 50 °C

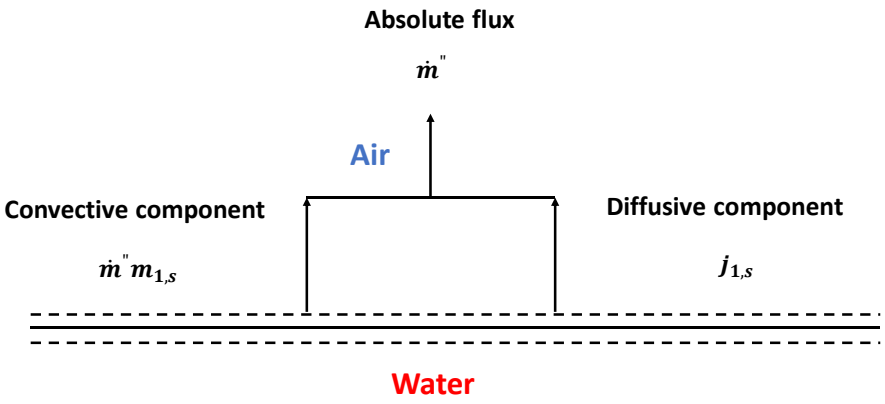

Figure 5.3: The convective and diffusive components of the absolute flux [3]

One writes the absolute flux of water vapor from the water surface $\dot{m}''$ as

$$\dot{m}'' = m_{1,s}\dot{m}'' + j_{1,s} = m_{1,s}\dot{m}'' - \rho D_{12}\frac{dm_1}{dr}. \tag{5.3}$$

Here, $j_{1,s}$ is the diffusive component of the mass flux, m_1 is the mass fraction of water, D_{12} is the water vapor-air diffusion coefficient, and ρ is the vapor density. The subscript s denotes the properties at the water surface and the subscript e denotes those in the gas stream.

After rearranging and integrating the equation across the boundary layer of width δ, we obtain

$$\int_{m_{1,s}}^{m_{1,e}} \frac{dm_1}{m_1\dot{m}'' - \dot{m}''} = \int_0^{\delta} \frac{\dot{m}'' dr}{\rho D_{12}}, \tag{5.4}$$

and

$$\frac{m_{1,e}-1}{m_{1,s}-1} = \exp\left(\frac{\dot{m}''\delta}{\rho D_{12}}\right). \tag{5.5}$$

We rewrite Equation (5.5) for later convenience as

$$1 + \frac{m_{1,s} - m_{1,e}}{1 - m_{1,s}} = \exp(\frac{\dot{m}'' \delta}{\rho D_{12}}). \tag{5.6}$$

Solving Eq. (5.6) for $\dot{m}''$ and using the mass transfer driving force B_{m1} defined as

$$B_{m1} = \frac{m_{1,s} - m_{1,e}}{1 - m_{1,s}}, \tag{5.7}$$

we obtain

$$\dot{m}'' = \frac{\rho D_{12}}{\delta} \ln(1 + B_{m1}) = \frac{\rho D_{12}}{\delta} \frac{\ln(1+B_{\mathrm{m1}})}{B_{\mathrm{m1}}} B_{\mathrm{m1}}. \tag{5.8}$$

Using the mass transfer conductance g_{m}^{*} defined as $\rho D_{12}/\delta$, we finally write

$$\frac{d\dot{m}_{\mathrm{L}}}{dA_z} = \dot{m}'' = g_{\mathrm{m}}^{*} \frac{\ln(1+B_{\mathrm{m1}})}{B_{\mathrm{m1}}} B_{\mathrm{m1}}. \tag{5.9}$$

We rewrite the energy balance equation by substituting the total evaporation rate in Eq. (5.2). The total energy transfer from liquid film to air stream includes both energy transfer from force convection and evaporation:

$$\frac{d}{dA_z}(\dot{m}_{\mathrm{L}} h_{\mathrm{L}}) = q_{\mathrm{conv}} + q_{\mathrm{evap}} \tag{5.10}$$

$$q_{\mathrm{evap}} = g_{\mathrm{m}}^{*} \frac{\ln(1+B_{\mathrm{m1}})}{B_{\mathrm{m1}}} B_{\mathrm{m1}} h_{1,s} \tag{5.11}$$

$$q_{\mathrm{conv}} = g_{\mathrm{h}} C_{\mathrm{p,G}} (T_{\mathrm{L}} - T_{\mathrm{G}}) \tag{5.12}$$

Here, q_{conv} and q_{evap} denote the convective and evaporative heat flux, respectively. $h_{1,\mathrm{s}}$ accounts for both the latent heat and the enthalpy variation due to temperature change. $C_{\mathrm{p,G}}$ is the air heat capacity. We estimate the heat transfer conductance using the heat and mass transfer analogy [3, 54]:

$$\frac{g_{\mathrm{m}}^{*}}{g_{\mathrm{h}}} = (Le)^{\frac{2}{3}} \approx 1.08 \tag{5.13}$$

The relative humidity of air is measured to be 100% at both the inlet and the outlet of our setup for all experimental conditions reported in the article. The properties of pure water and saturated air are obtained from existing literatures [96–99]. The latent heat and the specific enthalpy of the saline water are calculated from Eqs. (5.14 and 5.15).

$$h_{fg,sw} = h_{fg,w}(1 - S) \tag{5.14}$$

$$h_{sw} = h_w - S(a_1 + a_2 S + a_3 S^2 + a_4 S^3 + a_5 t + a_6 t^2 + a_7 t^3 + a_8 St + a_9 S^2 t + a_{10} St^2) \tag{5.15}$$

The coefficients are listed below:

$$a_1 = -2.348 \times 10^4, a_2 = 3.152 \times 10^5, a_3 = 2.803 \times 10^6, a_4 = -1.446 \times 10^7,$$
$$a_5 = 7.826 \times 10^3, a_6 = -4.417 \times 10^1, a_7 = 2.139 \times 10^{-1}, a_8 = -1.991 \times 10^4,$$
$$a_9 = 2.778 \times 10^4, a_{10} = 9.728 \times 10^1$$

Here, $h_{\mathrm{fg,sw}}$ and $h_{\mathrm{fg,w}}$ denote the latent heat of saline water and pure water in J/kg, respectively. h_{sw} and h_{w} are the enthalpy of saline water and pure water, respectively, in J/kg, S the salinity in kg/kg, and t the temperature in °C. The vapor pressure of saline water is estimated using Raoult's correlation:

$$\frac{P_{v,w}}{P_{v,sw}} = 1 + 0.57357 \times \left(\frac{S}{1-S}\right) \tag{5.16}$$

$P_{\mathrm{v,w}}$ and $P_{\mathrm{v,sw}}$ represent the vapor pressure of pure water and saline water, respectively.

The only unknown parameter in this model is g_m^*. We iteratively solve Eqs. (5.1) and (5.2) numerically, while treating g_m^* as the adjustable fitting parameter, until the calculated spatial temperature profile fits the experimental data. Linear temperature profiles based on the inlet and outlet temperatures are used as initial guesses for the liquid and air stream. The extracted value of g_m^* is then considered to be the overall mass transfer conductance. A typical fit is shown in Figure 5.4

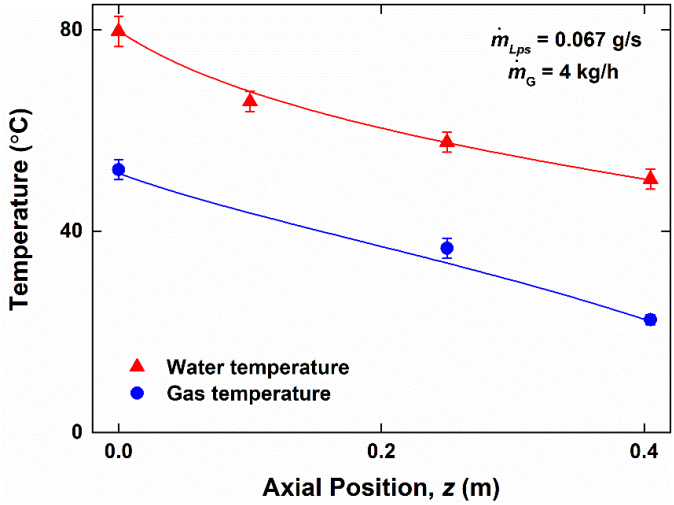

Figure 5.4: A representative fit of the experimentally measured spatial profiles of the liquid and air temperature using the heat/mass transfer model.

Following the convention for humidifiers in the literature, we report the total air flow rates. The superficial air velocity can be calculated from the total air flow rate by dividing them with the cross-sectional area of the acrylic pipe (3.16×10^{-3} m^2). A mass flow rate of 4 kg/h, for example, corresponds to a superficial air velocity of 0.3 m/s. The liquid flow rate is reported as the liquid

flow rate per string, $\dot{m}_{Lps}$. The corresponding total liquid mass flow rate is $\dot{m}_L$ can be calculated by multiplying $\dot{m}_{Lps}$ with the total number of the strings 24.

5.4 Results and discussion

5.4.1 Mass transfer conductance

We first examine the extracted values of the mass transfer conductance g_m^* to elucidate the effects of the liquid flow rate, air flow rate, and salinity. Following a previous study [36], we define the overall capacity coefficient as $g_m^* A/V$. Here, A and V denote the liquid-gas interfacial area and the volume of the humidifier, respectively. This parameter essentially helps quantify the mass transfer rate per unit volume of a humidifier.

Figure 5.5a shows that the overall capacity coefficient increases approximately linearly with the air flow rate. Differences in the overall capacity coefficients are within 10% for liquid streams of the three different salinities tested. In contrast, Figure 5.5b shows that the overall capacity coefficient increases as the liquid flow rate per string increases. Both results are consistent with the observed liquid film profiles shown in Figure 5.6.

Because the salinities used are not high enough to significantly alter the surface tension, viscosity or density, the liquid films of the three different salinities show very similar liquid film profiles. We remind the reader that the intrinsic instability of liquid films flowing down vertical strings result in the formation of traveling liquid beads. For a given liquid flow rate (either Figure 5.6a or Figure 5.6b), the liquid bead sizes and the inter-bead spacings are within 2% of each other. In contrast, when the liquid flow rate is changed, the inter-bead spacing also changes. As the liquid bead size is approximately constant, to accommodate a higher mass flow rate, the inter-bead spacing needs to decrease [74]. That is, per unit volume, there are more liquid beads that facilitate

mass transfer accompanying evaporation or condensation [100] with their localized curved interfaces. The overall capacity coefficient therefore increases with increasing liquid mass flow rates.

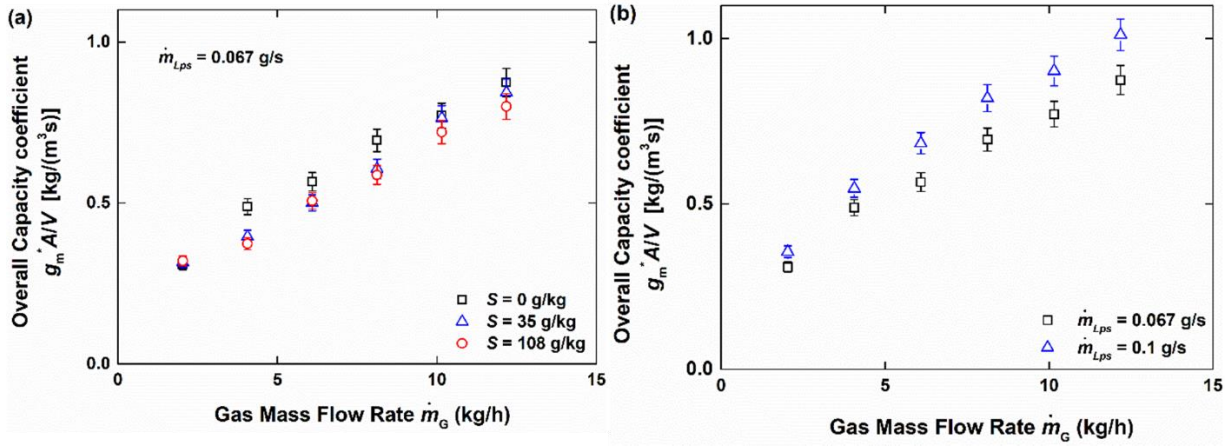

Figure 5.5: Overall capacity coefficients for the feed water streams of (a) three different salinities at a fixed liquid flow rate. (b) two different liquid flow rates at a fixed salinity. The inlet liquid and air temperatures are 80 ºC and 22 ºC, respectively. Air flow rates of 0 - 15 kg/h correspond to superficial air velocities of 0 – 1.1 m/s.

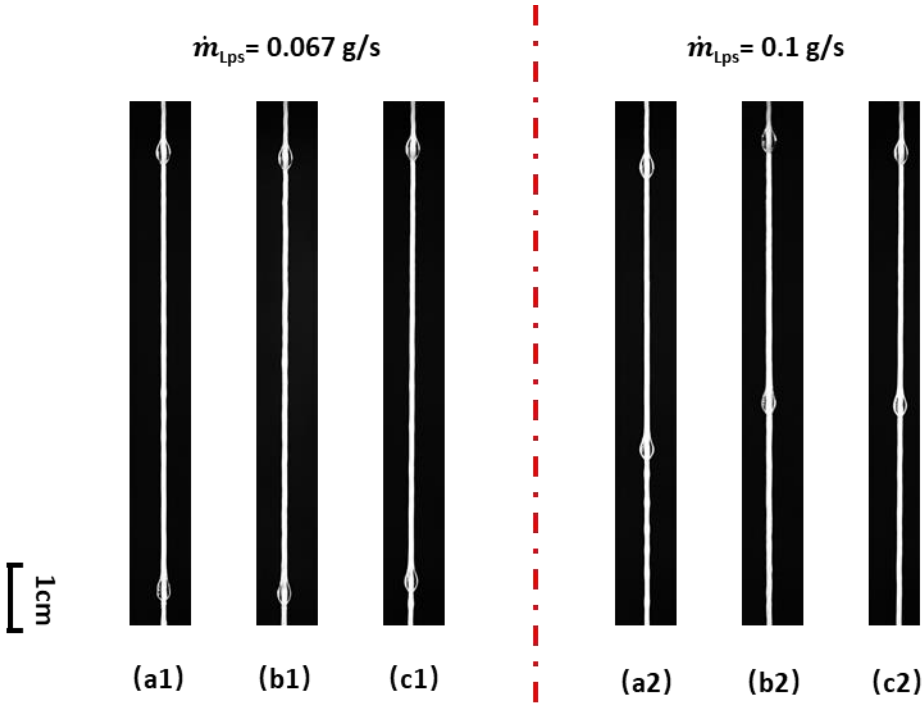

Figure 5.6: Liquid film profiles at two different liquid flow rates ($\dot{m}_{Lps}$ = 0.067 or 0.1 g/s) for liquid feed streams of three different salinities: (a) S = 0 g/kg (b) S = 35 g/kg (c) S = 108 g/kg.

5.4.2 Evaporation rate and humidifier effectiveness

The best fit value of g_m^* is then used to compute the total evaporation rate shown in Figure 5.7 using two methods to confirm the consistency of the model. In the first method, we numerically integrate Eq. (5.9) along the axial direction while approximating the liquid film as a smooth cylindrical surface of radius obtained from the Nusselt solution [29]. In the second method, we calculate the evaporation rate from a difference in the liquid mass flow rate $\dot{m}_L$ between the inlet and the outlet. We confirm that the two methods yield the same values of the total evaporation rate.

Figure 5.7 shows the obtained evaporation rates for feed streams with the three different salinities at a fixed liquid flow rate. Although the mass transfer conductance values are similar, the streams with higher salinity values yields slightly (5~ 10%) lower evaporation rates because of lower water vapor pressures, consistent with the results from previous studies [81, 85]. The lower vapor pressures lead to lower convective components of the absolute fluxes. Although the mass transfer conductance shows the same value, the total evaporation rate is affected by salinity because of different convective components.

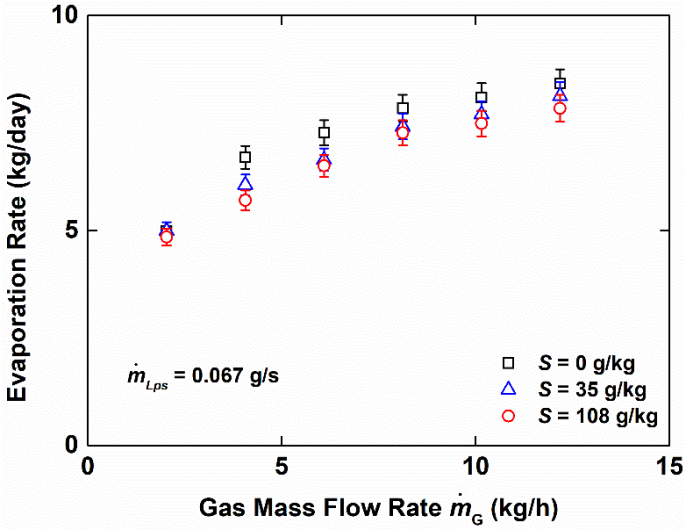

Figure 5.7: The water evaporation rate as a function of the air mass flow rate for liquid feed streams with three different salinities. The inlet liquid and air temperature are fixed at 80 ºC and 22 ºC, respectively.

We next normalize the water evaporation rate with the feed water flow rate (Eq. 5.17) to examine the influence of the liquid flow rate on the evaporation rate. The normalized evaporation rate is identical to the maximum water recovery ratio (RR) when one assumes that the water vapor completely condenses in a dehumidifier.

$$\beta = \frac{\dot{m}_{\mathrm{L,in}} - \dot{m}_{\mathrm{L,out}}}{\dot{m}_{\mathrm{L,in}}} \tag{5.17}$$

Figure 5.8a shows that the higher liquid flow rate leads to the higher evaporation rate. This is consistent with the increase in the overall capacity coefficient, which results largely from the decreased inter-bead spacing, as discussed in Sec 4.1. However, the normalized evaporation rate is smaller for the higher liquid flow rate (Figure 5.8b). This suggests that the enhancement in heat/mass transfer rates due to decreasing inter-bead spacing is not sufficient to fully counteract an increase in the liquid mass flow rate.

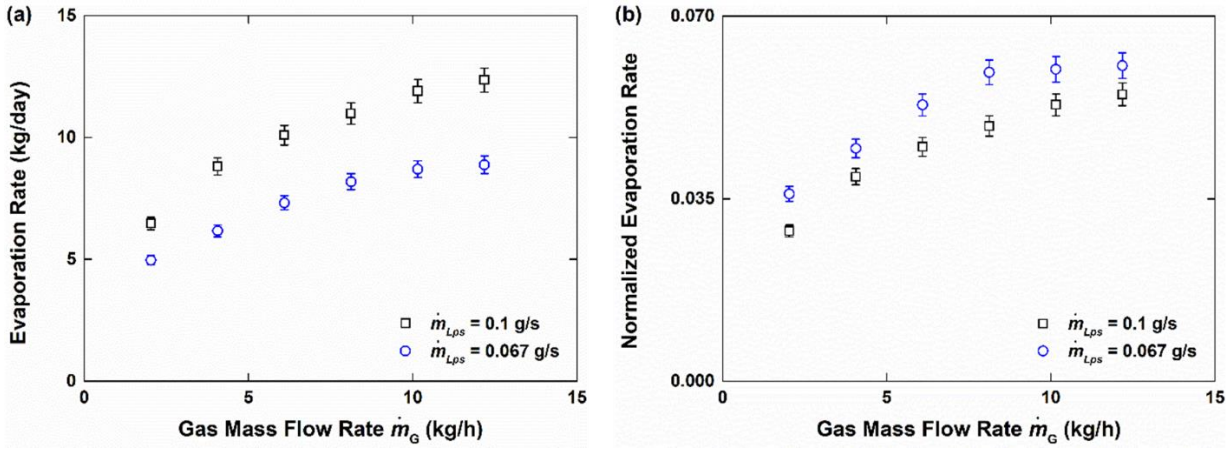

Figure 5.8: (a) The calculated evaporation rate as a function of the air mass flow rate for two different liquid flow rates. (b) The corresponding normalized evaporation rate as a function of the air mass flow rate. Distilled water is considered as the feed liquid. The inlet liquid and air inlet temperature are fixed at 80 ºC and 22 ºC, respectively.

The humidifier effectiveness is often defined as the ratio of the change in the real enthalpy to the maximum possible change in the liquid enthalpy [101]:

$$\varepsilon = \frac{\Delta H}{\Delta H_{\max}} \tag{5.18}$$

Here, ΔH denotes the enthalpy change of either the cold stream or the hot stream. $\Delta H_{\max}$ represents the maximum possible enthalpy change. Under the experimental conditions used in the present study, the maximum possible enthalpy change is that for the liquid stream.

Taking the ratio between the humidifier effectiveness and the normalized evaporation rate, we obtain

$$\frac{\varepsilon}{\beta} = \frac{\Delta H}{\Delta H_{\max}\,\beta} = \frac{h_{\mathrm{L,in}} - h_{\mathrm{L,out}}}{\Delta h_{\max}} \frac{\dot{m}_{\mathrm{L,in}}}{\dot{m}_{\mathrm{L,in}} - \dot{m}_{\mathrm{L,out}}} = \frac{(\dot{m}_{\mathrm{L,in}} - \dot{m}_{\mathrm{L,out}})\Delta h_L}{(\dot{m}_{\mathrm{L,in}} - \dot{m}_{\mathrm{L,out}})\Delta h_{\max}} = \frac{\Delta h_L}{\Delta h_{\max}} \tag{5.19}$$

Here, $h_{\mathrm{L,in}}$ and $h_{\mathrm{L,out}}$ denote the total specific enthalpy of the liquid at the inlet and the outlet, respectively. $\Delta h_{\max}$ is the difference between the total specific enthalpy at the liquid inlet temperature and the total specific enthalpy at the air inlet temperature. Since the latent heat dominates the total specific enthalpy, Δh_{L} varies by only 2% from 20 ºC to 90 ºC. $\Delta h_{,\max}$ is only a function of the liquid and air inlet temperatures. As a result, the normalized evaporation rate and the humidifier effectiveness depend linearly on each other for given liquid and gas inlet temperatures.

For one pair of the liquid inlet temperature and the air inlet temperature, we perform experiments with different combinations of liquid flow rates and air velocities. Figure 5.9 shows the relationship between the humidifier effectiveness and the normalized evaporation rate thus

obtained. The experimental results agree with the analytical prediction to within 5%, confirming that the normalized evaporation rate is thermodynamically limited by the liquid and gas inlet conditions.

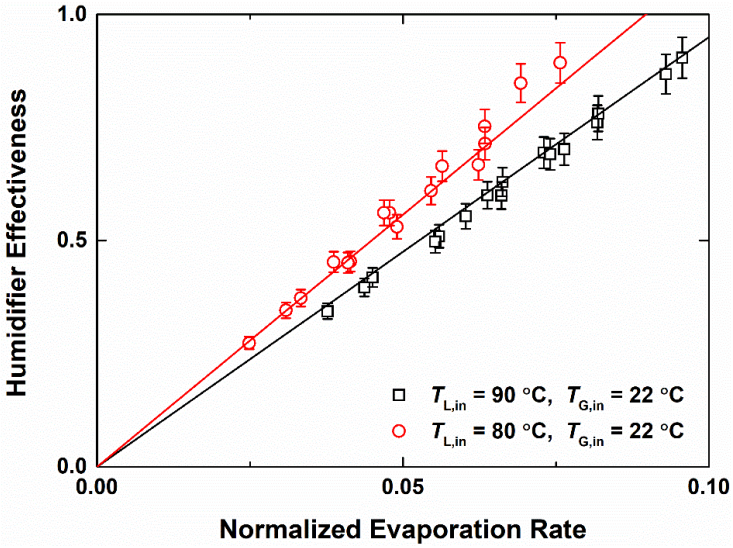

Figure 5.9: The relationship between the humidifier effectiveness and the normalized evaporation rate. The symbols are the experimental data and the solid lines are the prediction from Eq. (5.19).

5.4.3 Gas stream pressure drop

The overall pressure drop in the gas stream may be divided into two components: the frictional pressure drop P_f and the acceleration pressure drop due to evaporation P_e [17]:

$$\Delta P = \int_0^L \left(\frac{dP_f}{dz} + \frac{dP_e}{dz}\right) dz \tag{5.20}$$

Under the experimental conditions used in the present study, the gas streams are expected to be in the turbulent regime. For turbulent flows along an infinitely long rod bundles, previous studies [76–78] reported engineering correlations for the friction loss. These correlations present the friction factor in terms of a geometric parameter defined in Eq. (5.21). The geometric parameter is defined using an equivalent annular zone of radius r_0, which has the same area as a square unit cell around each string [76], and the radius of the cylindrical liquid film around strings, r_1 as shown in Figure 5.10.

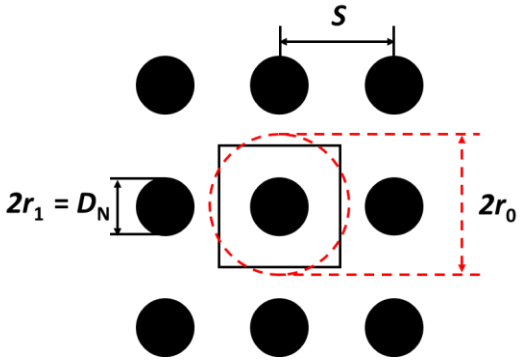

Figure 5.10: The geometric parameters of a square array of strings. The red circle represents the equivalent annual zone of a unit square cell (the black square).

The geometric parameter x [76] is defined as

$$x = \frac{r_0}{r_1} = \sqrt{\frac{4}{\pi}}\frac{s}{D_N} \tag{5.21}$$

Here D_N and s represent the average liquid film diameter calculated from the Nusselt solution [29], and the string pitch, respectively.

The universal velocity profile for turbulent flows on circular tubes was taken as [102]

$$u^+ = 2.5 \ln y^+ + 5.5 \tag{5.22}$$

Here, $u^+ = u/u^*$ is the dimensionless velocity, $u^* = \sqrt{(\tau_w/\rho)}$ is the frictional velocity, $y^+ = \rho y u^*/\mu$ is the dimensionless distance from the wall. An engineering correlation for the friction factor f_T of an annular zone in the turbulent regime was reported in terms of the frictional velocity as [103]

$$\sqrt{\frac{8}{f_T}} = 2.5 \ln\left(\frac{\rho L u^*}{\mu}\right) + 5.5 - \frac{3.966+1.25x}{1+x} \tag{5.23}$$

Here, $L = r_0 - r_1$ is the width of the annular zone. The shear stress τ_w can be expressed as $f_T \rho u^2/8$. Eq. (5.23) can then be re-written as

$$\sqrt{\frac{8}{f_T}} = 2.5 \ln\left(\frac{\rho\,(r_0-r_1)u}{\mu}\sqrt{\frac{f_T}{8}}\right) + 5.5 - \frac{3.966+1.25x}{1+x} \tag{5.24}$$

The Reynolds number of the equivalent annular zone is defined as $Re = \rho u D_h/\mu$, where D_h is the hydraulic diameter and equal to $2(r_0^2 - r_1^2)/r_1$. A more commonly used form of Eq. (5.24) can be obtained by substituting this definition of the Reynolds number into Eq. (5.24) and rearranging the resulting equation:

$$\sqrt{\frac{8}{f_T}} = 2.5\ln\left(Re\sqrt{\frac{f_T}{8}}\right) + 5.5 - \frac{3.966+1.25x}{1+x} - 2.5\ln(2+2x) \tag{5.25}$$

The frictional pressure drop is obtained from

$$\frac{\Delta P_f}{\Delta z} = \frac{f_T \rho u^2}{2D_\mathrm{h}} \tag{5.26}$$

The acceleration pressure drop due to evaporation is calculated from [17]

$$\frac{dP_e}{dz} = \left(\frac{\dot{m}_\mathrm{G}}{A_\mathrm{C}}\right)^2\left(\frac{1}{\rho_\mathrm{G}} - \frac{1}{\rho_\mathrm{f}}\right)\frac{d\omega}{dz} \tag{5.27}$$

Here, A_c denotes the air stream cross-sectional area, ρ_G the air density, ρ_f the water density, and ω the humidity ratio. The relative humidity values of the air stream at the inlet and outlet are experimentally determined to be 100%. The air inlet temperature is fixed at 22 °C and the corresponding humidity ratio is 16.74 g water/kg dry air. The outlet air temperature varies with different experimental conditions (liquid mass flow rates, liquid inlet temperatures, and air mass flow rates). The corresponding humidity ratio can be obtained from the thermodynamics table [96–99]. The humidity ratio can also be related to the mass fraction by $\omega = m_1/(1 - m_1)$.

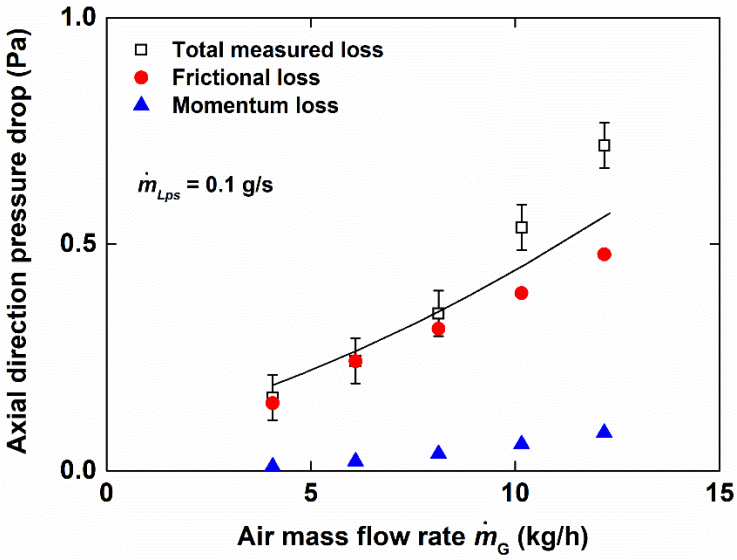

Figure 5.11: The pressure drop along the gas stream of the multi-string humidifier. The squares are the experimental data. The line represents prediction from Eq. (5.20). The circles and triangles show the two components of the pressure drop. The air flow rates of 0 - 15 kg/h correspond to the superficial air velocities of 0 – 1.1 m/s.

Figure 5.11 shows the measured and predicted axial pressure drop in the gas stream as a function of the gas mass flow rate. Note first that the gas stream pressure drop is very small, only of the order of 1 Pa. The model prediction agrees with the experimental data to within 5% for air mass flow rates below 10 kg/h. But the model underpredicts the pressure drops by as much as 20% at higher air velocities. This is in part due to the additional form drag caused by liquid beads traveling down the strings (see Figure 5.6) [95], which is not accounted for in the engineering correlation for smooth rod bundles. The acceleration pressure drop due to evaporation contributes 10 - 15% of the total pressure drop at mass flow rates higher than 10 kg/h where evaporation rate is correspondingly higher.

Smaller string pitches lead to higher values of the overall capacity coefficient, $g_m^* A/V$, but at the expense of increased gas-stream pressure drops. The smallest practical string pitch is estimated to be of the order of 5 mm, constrained in part by liquid flooding at the air inlet and in part by interference between liquid films flowing down adjacent strings. All the data reported in the present manuscript is based on a string array of pitch 10 mm as a compromise between achieving a high overall capacity coefficient and achieving a low gas-stream pressure drop. In separate unreported experiments, we used string arrays with pitches as big as 20 mm and arrays with pitches as small as 5 mm. The smallest pitch presented many practical challenges in manufacturing and assembly. We observed almost 4 times increase in the overall capacity coefficient but also a commensurate increase in the air stream pressure drop. The results were consistent with our model predictions.

Popular string arrangements are square and triangular arrays. Previous study [75] showed that the friction factor for flows along a triangular array of rods is higher than along a square array for the same porosity. But the difference falls below 2% when porosity values are higher than 0.95 [75], which is expected to be the case in our multi-string humidifiers. We therefore expect the string array arrangement to have a small influence on the gas-stream pressure drop and evaporation rate for a given string pitch and a porosity.

5.4.4 Humidifier performance comparison

We lastly compare the performance metrics of our multi-string humidifier with other types of previously reported humidifiers [81]: a pad humidifier and a spray humidifier. The present multi-string humidifier has a height of 0.4 m and a cross-sectional area of 0.0032 m^2. The pad humidifier was made of a corrugated cellulosic material similar to packed beds and used widely in humidifiers

in HDH systems [81, 86, 87]. The pad humidifier reported in a previous study has a height of 0.332 m and a cross-sectional area of 0.25 m^2 [81]. The spray humidifier consisted of four polypropylene nozzles spraying seawater into a counterflowing air stream. The spray humidifier had a height of 2 m and a cross-sectional area of 0.07 m^2.

We compare the daily water evaporation rates per unit humidifier volume as one main performance metric. In the comparison, we selected the experiments where the superficial air velocities were approximately the same. But the superficial liquid velocities differed slightly: 0.6 mm/s for our multi-string humidifier; 0.65 mm/s for the pad humidifier; and 1.41 mm/s for the spray humidifier.

Figure 5.12 shows that the present multi-string humidifier can achieve higher evaporation rates at much lower gas stream pressure drops. This is attributed to the unique geometric configuration of our multi-string humidifier that offers high interfacial areas per unit volume while providing straight and contiguous gas flow paths.

A bubble column is another widely used device configuration for humidification. However, the working mechanism of bubble columns is rather different from counterflow exchangers, making direct comparison difficult. Previously reported bubble column humidifiers achieved evaporation rates of approximately 5000-8000 kg/day/m^3 at gas stream pressure drops higher than 10 kPa [21]. As a conservative estimate, only the volume of the water reservoir is considered as the volume of the bubble columns.

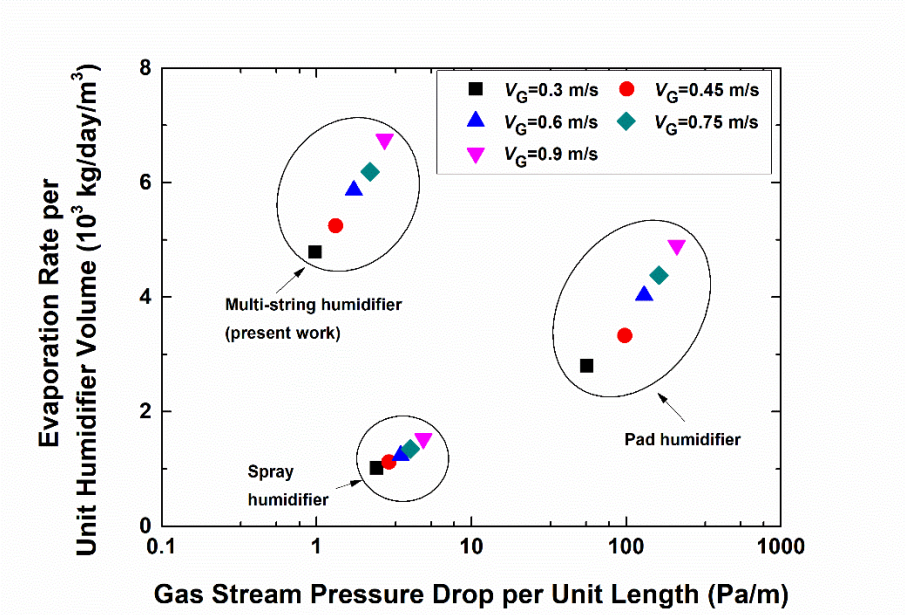

Figure 5.12: The comparison of the performance of the present multi-string humidifier with other types of humidifiers [81]

5.5. Summary

A new design of humidifiers consisting of a dense array of strings for humidification-dehumidification desalination is presented and experimentally investigated in this study. We show that this new design enables humidifiers to achieve high heat and mass transfer rates without suffering from a large gas-stream frictional loss. We extract the overall capacity coefficient from measured spatial temperature profiles to quantify the humidifier performance. The overall capacity coefficient increases with increasing liquid and air flow rates but varies within 10% for feed streams with salinities ranging from 0 to 108 g/kg. The saline water with the highest salinity used delivers approximately 10% lower evaporation rates due to its lower water vapor pressures. The multi-string humidifier can deliver comparable evaporation rates at an order of magnitude gas phase pressure drop than a pad humidifier or 5 times higher evaporation rates at a comparable gas

phase pressure drop than a spray humidifier. The present study demonstrates a multi-string humidifier with superior performance for potential applications in small-scale and mobile desalination.

Chapter 6

Summary and future work recommendations

6.1 Summary

The present work investigates the interfacial heat and mass transfer of liquid films flowing down strings against counterflowing gas streams. We begin our study from constructing a numerical model using the moving mesh method to study heat transfer phenomena for liquid films falling over highly curved surfaces in the drop-like flow regime dominated by the Rayleigh-Plateau instability. Our numerical simulation results agree well with the prediction from an analytical model for the evolution of the average bead temperature, when combined with independently predicted liquid bead-to-air and liquid substrate-to-air heat transfer coefficients.

We then experimentally investigated the relationship between flow characteristics and overall heat exchanger effectiveness for the thin liquid film flowing along a single string against a counterflowing air stream. The experimental results demonstrate that the flow characteristics are affected by the liquid mass flow rate, air velocity, and nozzle radius, but the overall heat exchanger effectiveness is only by liquid mass flow rate and the air velocity. The increase in air velocity or inter-bead spacing results in the increase in local bead-to-air heat transfer coefficient.

We extended our study to the heat transfer performance and gas phase frictional loss of a multi-string heat exchanger. We conducted a combination of experimental and numerical investigation of the impact of the liquid flow rate, air velocity, and string pitch on the heat exchanger effectiveness as well as the air side pressure drop. The overall heat transfer coefficients between the liquid film with Rayleigh Plateau instability and Kapitza instability are compared. The Reynolds analogy was validated in the multi-string heat exchanger showing a relatively small

contribution of form drag afforded by the wavy liquid films. The comparison between the multi-string heat exchanger and a vertical aligned structured packing justifies the superior performance of the multi-string exchanger.

We finally adapted the multi-string structure for desalination purpose. The cotton strings were utilized to assemble the setup to ensure perfect wetting of water on strings. We show that this new design enables humidifiers to achieve high heat and mass transfer rates without suffering from a large gas-stream frictional loss. We studied the influence of the liquid mass flow rate, air velocity and liquid salinity on the evaporation rate of the humidifier. The multi-string humidifier is also compared with other commercialized humidifiers: a pad humidifier and a spray column. Our study demonstrates that the multi-string humidifier can deliver the comparable evaporation rates at an order of magnitude lower gas phase pressure drop.

6.2 Future work recommendations

The following recommendations are made for future research on the interfacial heat and mass transfer of the liquid film down strings against counterflowing gas.

6.2.1 Using phase change materials as working fluids

We propose phase change materials as the working fluids in multi-string heat exchangers. Phase change process involves a larger amount of energy transfer than the sensible heat transfer. One good candidate for phase change material is methyl palmitate with a melting temperature of 30 ºC. Metal strings with a good thermal conductivity, such as copper and brass strings, are used instead of the polymer or cotton strings. The strings are in contact with the high temperature liquid reservoir to maintain a surface temperature higher than 30 ºC through conduction. This ensures no

solidification of the methyl palmitate on the string surface to maintain a continuous flow. The phase change process only happens on the liquid-gas interface. Both the axial temperature gradient along the metal string and radial temperature gradient across the liquid film require rigorous understanding to avoid flow jam due to liquid solidification. The liquid film instability of methyl palmitate is also an interesting topic to investigate for optimizing its heat transfer characteristics.

6.2.2 The multi-string particle collector for air filtration

Compared with the spray column, the multi-string exchanger has the advantages of achieving orders of magnitude higher heat/mass transfer performance at the same gas phase pressure drop. The wet electrostatic precipitator effectively absorbs particles with a diameter smaller than 10 μm or 2.5 μm (PM 10 or PM 2.5) and therefore is widely used to treat the exhaust gas from combustion before discharging it to the atmosphere. The electrostatic spray technology is often integrated into the wet electrostatic spray to disperse charged liquid. The structure of electrostatic sprays used in an electrostatic precipitator resembles spray columns, which offers less liquid-gas contact time than a multi-string configuration. The existence of the strings impedes the downward motion of the liquid and enhances overall absorption effectiveness by offering longer contact time between charged liquid films and particles. Consequently, the required size of a multi-string particle collector is smaller than the electrostatic precipitators with electrostatic sprays. In the multi-string particle collector, a voltage of 20 kV is applied to charge the liquid in the reservoir before it flows down arrays of strings. Liquid nozzles facilitate uniform liquid distributions to strings. A counterflowing air stream with charged dust particles is blown from the bottom. To design a multi-string particle collector, rigorously understanding the fluid dynamics and mass transfer performance of the conductive liquid film flowing down strings is necessary. The relationship

between the applied voltage and liquid flow rates should be studied to generate stable liquid film. The charged liquid film instability should be investigated to examine the influence of electric field on the liquid film fluid dynamics. The appropriate selection of liquid nozzle also requires systematic studies and tests to ensure no dust accumulation in nozzles.

References

[1] K. Onda, H. Takeuchi, and Y. Okumoto, “Mass Transfer Coefficients Between Gas and Liquid Phases in Packed Columns,” *J. Chem. Eng. Jpn.*, vol. 1, no. 1, pp. 56–62, 1968.

[2] K. Onda, H. Takeuchi, and Y. Koyama, *Effect of packing materials on the wetted surface area*. 1990.

[3] A. F. Mills, *Mass Transfer*, 1 edition. Upper Saddle River, N.J: Prentice Hall, 2001.

[4] A. Mersmann and A. Deixler, “Packungskolonnen,” *Chem. Ing. Tech.*, vol. 58, no. 1, pp. 19–31, Jan. 1986.

[5] K. Uchiyama, H. Migita, R. Ohmura, and Y. H. Mori, “Gas absorption into ‘string-of-beads’ liquid flow with chemical reaction: application to carbon dioxide separation,” *Int. J. Heat Mass Transf.*, vol. 46, no. 3, pp. 457–468, Jan. 2003.

[6] R. Letan and E. Kehat, “The mechanics of a spray column,” *AIChE J.*, vol. 13, no. 3, pp. 443–449, May 1967.

[7] T. Nozaki, N. Kaji, and Y. H. Mod, “Heat Transfer to a Liquid Flowing Down Vertical Wires Hanging in a Hot Gas Stream: an Experimental Study of a New Means of Thermal Energy Recovery,” *HEAT Transf.*, vol. 6, pp. 63–68, 1998.

[8] H. Zhai and E. S. Rubin, “Performance and cost of wet and dry cooling systems for pulverized coal power plants with and without carbon capture and storage,” *Energy Policy*, vol. 38, no. 10, pp. 5653–5660, Oct. 2010.

[9] K. P. Lee, T. C. Arnot, and D. Mattia, “A review of reverse osmosis membrane materials for desalination—development to date and future potential,” *J. Membr. Sci.*, vol. 370, no. 1–2, pp. 1–22, 2011.

[10] G. Kang and Y. Cao, “Development of antifouling reverse osmosis membranes for water treatment: A review,” *Water Res.*, vol. 46, no. 3, pp. 584–600, Mar. 2012.

[11] M. F. A. Goosen, S. S. Sablani, H. Al-Hinai, S. Al-Obeidani, R. Al-Belushi, and aD Jackson, “Fouling of reverse osmosis and ultrafiltration membranes: a critical review,” *Sep. Sci. Technol.*, vol. 39, no. 10, pp. 2261–2297, 2005.

[12] A. D. Khawaji, I. K. Kutubkhanah, and J.-M. Wie, “Advances in seawater desalination technologies,” *Desalination*, vol. 221, no. 1, pp. 47–69, Mar. 2008.

[13] I. S. Al-Mutaz, “A comparative study of RO and MSF desalination plants,” *Desalination*, vol. 106, no. 1, pp. 99–106, Aug. 1996.

[14] A. Giwa, N. Akther, A. A. Housani, S. Haris, and S. W. Hasan, “Recent advances in humidification dehumidification (HDH) desalination processes: Improved designs and productivity,” *Renew. Sustain. Energy Rev.*, vol. 57, pp. 929–944, May 2016.

[15] S. Parekh, M. M. Farid, J. R. Selman, and S. Al-Hallaj, “Solar desalination with a humidification-dehumidification technique—a comprehensive technical review,” *Desalination*, vol. 160, no. 2, pp. 167–186, 2004.

[16] R. H. Xiong, S. C. Wang, L. X. Xie, Z. Wang, and P. L. Li, “Experimental investigation of a baffled shell and tube desalination column using the humidification-dehumidification process,” *Desalination*, vol. 180, no. 1–3, pp. 253–261, 2005.

[17] M. Sievers and J. H. L. V, “Design of Flat-Plate Dehumidifiers for Humidification–Dehumidification Desalination Systems,” *Heat Transf. Eng.*, vol. 34, no. 7, pp. 543–561, Jan. 2013.

[18] J. F. Klausner, Y. Li, and R. Mei, “Evaporative heat and mass transfer for the diffusion driven desalination process,” *Heat Mass Transf.*, vol. 42, no. 6, p. 528, May 2005.

[19] G. P. Narayan, M. H. Sharqawy, S. Lam, S. K. Das, and J. H. Lienhard, “Bubble columns for condensation at high concentrations of noncondensable gas: Heat-transfer model and experiments,” *AIChE J.*, vol. 59, no. 5, pp. 1780–1790, May 2013.

[20] T. Rajaseenivasan, R. K. Shanmugam, V. M. Hareesh, and K. Srithar, “Combined probation of bubble column humidification dehumidification desalination system using solar collectors,” *Energy*, vol. 116, pp. 459–469, Dec. 2016.

[21] S. A. El-Agouz, “A new process of desalination by air passing through seawater based on humidification–dehumidification process,” *Energy*, vol. 35, no. 12, pp. 5108–5114, Dec. 2010.

[22] A. Khalil, S. A. El-Agouz, Y. A. F. El-Samadony, and A. Abdo, “Solar water desalination using an air bubble column humidifier,” *Desalination*, vol. 372, pp. 7–16, Sep. 2015.

[23] G. Grabbert and G. Wünsch, “Zur Hydraulik stark gekrümmter Rieselfilme,” *Freib. Forschungshefte A*, vol. 517, pp. 61–83, 1973.

[24] J. W. Strutt and Lord Rayleigh, “On the instability of jets,” *Proc Lond. Math Soc*, vol. 10, no. 4, 1878.

[25] D. Ter Haar, *Collected papers of PL Kapitza*, vol. 2. Elsevier, 2013.

[26] I. L. Kliakhandler, S. H. Davis, and S. G. Bankoff, “Viscous beads on vertical fibre,” *J. Fluid Mech.*, vol. 429, pp. 381–390, 2001.

[27] C. Ruyer-Quil, P. Treveleyan, F. Giorgiutti-Dauphiné, C. Duprat, and S. Kalliadasis, "Modelling film flows down a fibre," *J. Fluid Mech.*, vol. 603, pp. 431–462, 2008.

[28] C. Ruyer-Quil and S. Kalliadasis, "Wavy regimes of film flow down a fiber," *Phys. Rev. E*, vol. 85, no. 4, p. 046302, Apr. 2012.

[29] C. Duprat, C. Ruyer-Quil, and F. Giorgiutti-Dauphiné, "Spatial evolution of a film flowing down a fiber," *Phys. Fluids*, vol. 21, no. 4, p. 042109, Apr. 2009.

[30] C. Duprat, C. Ruyer-Quil, S. Kalliadasis, and F. Giorgiutti-Dauphiné, "Absolute and Convective Instabilities of a Viscous Film Flowing Down a Vertical Fiber," *Phys. Rev. Lett.*, vol. 98, no. 24, p. 244502, Jun. 2007.

[31] S. Muzaferija and M. Peric, "Computation of free-surface flows using interface tracking and interface-capturing methods," *Adv. Fluid Mech.*, vol. 24, pp. 59–100, 1999.

[32] G. D. Wehinger, J. Peeters, S. Muzaferija, T. Eppinger, and M. Kraume, "Numerical simulation of vertical liquid-film wave dynamics," *Chem. Eng. Sci.*, vol. 104, pp. 934–944, Dec. 2013.

[33] R. Liu, Z. Ding, and X. Chen, "The effect of thermocapillarity on the dynamics of an exterior coating film flow down a fibre subject to an axial temperature gradient," *Int. J. Heat Mass Transf.*, vol. 123, pp. 718–727, Aug. 2018.

[34] K. Hattori, M. Ishikawa, and Y. H. Mori, "Strings of liquid beads for gas-liquid contact operations," *AIChE J.*, vol. 40, no. 12, pp. 1983–1992, 1994.

[35] H. Chinju, K. Uchiyama, and Y. H. Mori, "'String-of-beads' flow of liquids on vertical wires for gas absorption," *AIChE J.*, vol. 46, no. 5, pp. 937–945, 2000.

[36] H. Migita, K. Soga, and Y. H. Mori, "Gas absorption in a wetted-wire column," *AIChE J.*, vol. 51, no. 8, pp. 2190–2198, Aug. 2005.

[37] S. G. Pakdehi and S. Taheri, “Separation of Hydrazine from Air by Wetted Wire Column,” *Chem. Eng. Technol.*, vol. 33, no. 10, pp. 1687–1694, Oct. 2010.

[38] S. M. Hosseini, R. Alizadeh, E. Fatehifar, and A. Alizadehdakhel, “Simulation of gas absorption into string-of-beads liquid flow with chemical reaction,” *Heat Mass Transf.*, vol. 50, no. 10, pp. 1393–1403, Apr. 2014.

[39] S. A. Galledari, R. Alizadeh, E. Fatehifar, and E. Soroush, “Simulation of carbon dioxide absorption by monoethanolamine solution in wetted-wire column,” *Chem. Eng. Process. Process Intensif.*, vol. 102, pp. 59–69, 2016.

[40] R. A. Seban and A. Faghri, “Evaporation and heating with turbulent falling liquid films,” *J. Heat Transf.*, vol. 98, no. 2, pp. 315–318, 1976.

[41] J. A. Shmerler and I. Mudawwar, “Local evaporative heat transfer coefficient in turbulent free-falling liquid films,” *Int. J. Heat Mass Transf.*, vol. 31, no. 4, pp. 731–742, 1988.

[42] J. A. Shmerler and I. Mudawwar, “Local heat transfer coefficient in wavy free-falling turbulent liquid films undergoing uniform sensible heating,” *Int. J. Heat Mass Transf.*, vol. 31, no. 1, pp. 67–77, 1988.

[43] S.-M. Yih and J.-L. Liu, “Prediction of heat transfer in turbulent falling liquid films with or without interfacial shear,” *AIChE J.*, vol. 29, no. 6, pp. 903–909, 1983.

[44] K. R. Chun and R. A. Seban, “Heat transfer to evaporating liquid films,” *J. Heat Transf.*, vol. 93, no. 4, pp. 391–396, 1971.

[45] T. Fujita and T. Ueda, “Heat transfer to falling liquid films and film breakdown—I: Subcooled liquid films,” *Int. J. Heat Mass Transf.*, vol. 21, no. 2, pp. 97–108, 1978.

[46] G. J. Gimbutis and A. D. S. Sinkunas, “HEAT TRANSFER OP A TURBULENT WATER FILM AT DIFFERENT INITIAL FLOW CONDITIONS AND HIGH TEMPERATURE GRADIENTS,” 1978.

[47] W. Wilke, “Warmeubertragung an rieselfilme,” *VDI-Forschungsheft*, vol. 490, p. B28, 1962.

[48] B. G. Ganchev, V. M. Koglov, and V. V. Lozovetskiy, “A study of heat transfer to a falling fluid film at a vertical surface,” *Heat Transfer–Sov Res*, vol. 4, pp. 102–110, 1972.

[49] H. Takahama and S. Kato, “Longitudinal flow characteristics of vertically falling liquid films without concurrent gas flow,” *Int. J. Multiph. Flow*, vol. 6, no. 3, pp. 203–215, Jun. 1980.

[50] C. Ruyer-Quil, S. P. M. J. Trevelyan, F. Giorgiutti-Dauphiné, C. Duprat, and S. Kalliadasis, “Film flows down a fiber: Modeling and influence of streamwise viscous diffusion,” *Eur. Phys. J. Spec. Top.*, vol. 166, no. 1, pp. 89–92, Jan. 2009.

[51] C. Duprat, C. Ruyer-Quil, and F. Giorgiutti-Dauphiné, “Experimental study of the instability of a film flowing down a vertical fiber,” *Eur. Phys. J. Spec. Top.*, vol. 166, no. 1, pp. 63–66, Jan. 2009.

[52] P.-G. de Gennes, *Capillarity and wetting phenomena: drops, bubbles, pearls, waves*. New York: Springer, 2004.

[53] B. J. Carroll, “The accurate measurement of contact angle, phase contact areas, drop volume, and Laplace excess pressure in drop-on-fiber systems,” *J. Colloid Interface Sci.*, vol. 57, no. 3, pp. 488–495, Dec. 1976.

[54] F. P. Incropera and A. S. Lavine, *Fundamentals of Heat and Mass Transfer*. John Wiley & Sons, 2011.

[55] G. D. Wehinger, J. Peeters, S. Muzaferija, T. Eppinger, and M. Kraume, “Numerical simulation of vertical liquid-film wave dynamics,” *Chem. Eng. Sci.*, vol. 104, pp. 934–944, Dec. 2013.

[56] B. Lloyd and R. Boehm, “Flow and heat transfer around a linear array of spheres,” *Numer. Heat Transf. Part Appl.*, vol. 26, no. 2, pp. 237–252, 1994.

[57] Z. Zeng, G. Warrier, and Y. S. Ju, “Study of the Fluid Dynamics of Thin Liquid Films Flowing Down a Vertical String With Counterflow of Gas,” p. V08BT10A054, Nov. 2015.

[58] Z. Zeng, G. Warrier, and Y. S. Ju, “Flow and Heat Transfer in Liquid Films Flowing Over Highly Curved Surfaces,” , Jul. 2015.

[59] McHale, G., Newton, M.I. and Carroll, B.J., The shape and stability of small liquid drops on fibers. Oil & Gas science and technology, 56(1), pp.47-54, 2001.

[60] J. Grünig, T. Skale, and M. Kraume, “Liquid flow on a vertical wire in a countercurrent gas flow,” *Chem. Eng. J.*, vol. 164, no. 1, pp. 121–131, 2010.

[61] W. M. Kays and A. L. London, “Compact heat exchangers,” Jan. 1984.

[62] R. S. Ramachandran, C. Kleinstreuer, and T.-Y. Wang, “Forced Convection Heat Transfer of Interacting Spheres,” *Numer. Heat Transf. Part Appl.*, vol. 15, no. 4, pp. 471–487, Jun. 1989.

[63] A. Mills, *Heat and Mass Transfer*. CRC Press, 1995.

[64] J. R. Fair, A. F. Seibert, M. Behrens, P. P. Saraber, and Z. Olujic, “Structured packing performance experimental evaluation of two predictive models,” *Ind. Eng. Chem. Res.*, vol. 39, no. 6, pp. 1788–1796, 2000.

[65] W. Brötz, “Über die Vorausberechnung der Absorptionsgeschwindigkeit von Gasen in strömenden Flüssigkeitsschichten1,” *Chem. Ing. Tech.*, vol. 26, no. 8–9, pp. 470–478, 1954.

[66] R. Kafesjian, C. A. Plank, and E. R. Gerhard, “Liquid flow and gas phase mass transfer in wetted-wall towers,” *AIChE J.*, vol. 7, no. 3, pp. 463–466, 1961.

[67] D. Bharathan, “Air-Water Countercurrent Annular Flow,” Dartmouth Coll., Hanover, NH (USA). Thayer School of Engineering, EPRI-NP-1165, Sep. 1979.

[68] J. Grünig, E. Lyagin, S. Horn, T. Skale, and M. Kraume, “Mass transfer characteristics of liquid films flowing down a vertical wire in a counter current gas flow,” *Chem. Eng. Sci.*, vol. 69, no. 1, pp. 329–339, Feb. 2012.

[69] Z. Zeng, A. Sadeghpour, G. Warrier, and Y. S. Ju, “Experimental study of heat transfer between thin liquid films flowing down a vertical string in the Rayleigh-Plateau instability regime and a counterflowing gas stream,” *Int. J. Heat Mass Transf.*, vol. 108, Part A, pp. 830–840, May 2017.

[70] F. R. Menter, “Two-equation eddy-viscosity turbulence models for engineering applications,” *AIAA J.*, vol. 32, no. 8, pp. 1598–1605, 1994.

[71] F. R. Menter, M. Kuntz, and R. Langtry, “Ten years of industrial experience with the SST turbulence model,” *Turbul. Heat Mass Transf.*, vol. 4, no. 1, pp. 625–632, 2003.

[72] A. Fluent, “ANSYS fluent theory guide 15.0,” *Inc Canonsburg PA*, 2013.

[73] W. I. Barnet and K. A. Kobe, “Heat and vapor transfer in a wetted-wall tower,” *Ind. Eng. Chem.*, vol. 33, no. 4, pp. 436–442, 1941.

[74] A. Sadeghpour, Z. Zeng, and Y. S. Ju, “Effects of Nozzle Geometry on the Fluid Dynamics of Thin Liquid Films Flowing down Vertical Strings in the Rayleigh–Plateau Regime,” *Langmuir*, vol. 33, no. 25, pp. 6292–6299, Jun. 2017.

[75] E. M. Sparrow and A. L. Loeffler, “Longitudinal laminar flow between cylinders arranged in regular array,” *AIChE J.*, vol. 5, no. 3, pp. 325–330, Sep. 1959.

[76] K. Rehme, “Pressure drop performance of rod bundles in hexagonal arrangements,” *Int. J. Heat Mass Transf.*, vol. 15, no. 12, pp. 2499–2517, 1972.

[77] K. Rehme, “Simple method of predicting friction factors of turbulent flow in non-circular channels,” *Int. J. Heat Mass Transf.*, vol. 16, no. 5, pp. 933–950, 1973.

[78] K. Rehme and G. Trippe, “Pressure drop and velocity distribution in rod bundles with spacer grids,” *Nucl. Eng. Des.*, vol. 62, no. 1–3, pp. 349–359, 1980.

[79] T. H. Chilton and A. P. Colburn, “Mass transfer (absorption) coefficients prediction from data on heat transfer and fluid friction,” *Ind. Eng. Chem.*, vol. 26, no. 11, pp. 1183–1187, 1934.

[80] T. H. Chilton and A. P. Colburn, “Distillation and absorption in packed columns A convenient design and correlation method,” *Ind. Eng. Chem.*, vol. 27, no. 3, pp. 255–260, 1935.

[81] S. Yanniotis and K. Xerodemas, “Air humidification for seawater desalination,” *Desalination*, vol. 158, no. 1, pp. 313–319, Aug. 2003.

[82] M. B. Amara, I. Houcine, and A. Guizani, “Theoretical and experimental study of a pad humidifier used in a seawater desalination process,” *Desalination*, vol. 168, pp. 1–12, 2004.

[83] E. Chafik, “A new type of seawater desalination plants using solar energy,” *Desalination*, vol. 156, no. 1, pp. 333–348, Aug. 2003.

[84] A. S. Cherif, S. B. Jabrallah, J.-P. Corriou, and A. Belghith, “Intensification of the liquid film evaporation in a vertical channel,” *Desalination*, vol. 250, no. 1, pp. 433–437, 2010.

[85] M. Al-Shammiri, “Evaporation rate as a function of water salinity,” *Desalination*, vol. 150, no. 2, pp. 189–203, 2002.

[86] G. Yuan and H. Zhang, “Mathematical modeling of a closed circulation solar desalination unit with humidification–dehumidification,” *Desalination*, vol. 205, no. 1–3, pp. 156–162, 2007.

[87] G. Yuan, Z. Wang, H. Li, and X. Li, “Experimental study of a solar desalination system based on humidification–dehumidification process,” *Desalination*, vol. 277, no. 1, pp. 92–98, Aug. 2011.

[88] A. M. I. Mohamed and N. A. S. El-Minshawy, “Humidification–dehumidification desalination system driven by geothermal energy,” *Desalination*, vol. 249, no. 2, pp. 602–608, 2009.

[89] G. Prakash Narayan, J. H. Lienhard, and S. M. Zubair, “Entropy generation minimization of combined heat and mass transfer devices,” *Int. J. Therm. Sci.*, vol. 49, no. 10, pp. 2057–2066, Oct. 2010.

[90] K. H. Mistry and S. M. Zubair, “Effect of entropy generation on the performance of humidification-dehumidification desalination cycles,” *Int. J. Therm. Sci.*, vol. 49, no. 9, pp. 1837–1847, 2010.

[91] R. K. McGovern, G. P. Thiel, G. Prakash Narayan, S. M. Zubair, and J. H. Lienhard, “Performance limits of zero and single extraction humidification-dehumidification desalination systems,” *Appl. Energy*, vol. 102, no. Supplement C, pp. 1081–1090, Feb. 2013.

[92] G. P. Narayan, K. M. Chehayeb, R. K. McGovern, G. P. Thiel, and S. M. Zubair, “Thermodynamic balancing of the humidification dehumidification desalination system by mass extraction and injection,” *Int. J. Heat Mass Transf.*, vol. 57, no. 2, pp. 756–770, 2013.

[93] K. M. Chehayeb, G. Prakash Narayan, S. M. Zubair, and J. H. Lienhard V, "Use of multiple extractions and injections to thermodynamically balance the humidification dehumidification desalination system," *Int. J. Heat Mass Transf.*, vol. 68, pp. 422–434, Jan. 2014.

[94] G. Prakash Narayan, M. G. St. John, S. M. Zubair, and J. H. Lienhard V, "Thermal design of the humidification dehumidification desalination system: An experimental investigation," *Int. J. Heat Mass Transf.*, vol. 58, no. 1–2, pp. 740–748, Mar. 2013.

[95] Z. Zeng, A. Sadeghpour, and Y. S. Ju, "Thermohydraulic characteristics of a multi-string direct-contact heat exchanger," *Int. J. Heat Mass Transf.*, vol. 126, Part A, pp. 536–544, Nov. 2018.

[96] R. W. Hyland and A. Wexler, "Formulations for the thermodynamic properties of dry air from 173.15 to 473.15 K, at pressure to 5 MPa," *ASHRAE Trans*, vol. 89, pp. 520–535, 1983.

[97] W. Wagner and A. Pruss, "The IAPWS formulation 1995 for the thermodynamic properties of ordinary water substance for general and scientific use," *J. Phys. Chem. Ref. Data*, vol. 31, no. 2, pp. 387–535, 2002.

[98] M. H. Sharqawy, J. H. Lienhard, and S. M. Zubair, "Thermophysical properties of seawater: a review of existing correlations and data," *Desalination Water Treat.*, vol. 16, no. 1–3, pp. 354–380, 2010.

[99] K. S. Spiegler, *Principles of desalination*. Elsevier, 2012.

[100] K.-C. Park *et al.*, "Condensation on slippery asymmetric bumps," *Nature*, vol. 531, no. 7592, p. 78, 2016.

[101] G. P. Narayan, K. H. Mistry, M. H. Sharqawy, S. M. Zubair, and J. H. Lienhard, “Energy effectiveness of simultaneous heat and mass exchange devices,” *Glob. Digit. Cent.*, 2010.

[102] J. Nikuradse, “Gesetzmäßigkeiten der turbulenten Strömung in glatten Rohren,” *Forsch. Im Ingenieurwesen*, vol. 4, no. 1, pp. 44–44, 1933.

[103] K. Maubach, “Reibungsgesetze turbulenter strömungen,” *Chem. Ing. Tech.*, vol. 42, no. 15, pp. 995–1004, 1970.